

1-1-2013

Investigations On Flow And Flow-Induced Vibration Of Candu Fuel Bundles

Alokendu Bhattacharya
Ryerson University

Follow this and additional works at: <http://digitalcommons.ryerson.ca/dissertations>

 Part of the [Mechanical Engineering Commons](#)

Recommended Citation

Bhattacharya, Alokendu, "Investigations On Flow And Flow-Induced Vibration Of Candu Fuel Bundles" (2013). *Theses and dissertations*. Paper 1272.

This Dissertation is brought to you for free and open access by Digital Commons @ Ryerson. It has been accepted for inclusion in Theses and dissertations by an authorized administrator of Digital Commons @ Ryerson. For more information, please contact bcameron@ryerson.ca.

INVESTIGATIONS ON FLOW AND FLOW-INDUCED VIBRATION OF
CANDU FUEL BUNDLES

by

Alokendu Bhattacharya

Master of Technology

Indian Institute of Technology Roorkee, India, 2006

Bachelor of Engineering

Bhilai Institute of Technology, Durg, India, 2004

A dissertation

presented to Ryerson University

in partial fulfillment of the

requirements for the degree of

Doctor of Philosophy

in the Program of

Mechanical and Industrial Engineering

Toronto, Ontario, Canada, 2013

© Alokendu Bhattacharya 2013

To my parents and brother Indrashish for their tireless support, love and encouragement.

To my daughter Eemon and wife Simanti, for their unforgettable sacrifice and continued patience in letting me pursue my doctoral study being thousands of miles away from them.

To my nephew Ishan, whose energy and curiosity has always been an inspiration to me.

AUTHOR'S DECLARATION FOR ELECTRONIC SUBMISSION OF A DISSERTATION

I hereby declare that I am the sole author of this dissertation. This is a true copy of the dissertation, including any required final revisions, as accepted by my examiners.

I authorize Ryerson University to lend this dissertation to other institutions or individuals for the purpose of scholarly research.

I further authorize Ryerson University to reproduce this dissertation by photocopying or by other means, in total or in part, at the request of other institutions or individuals for the purpose of scholarly research.

I understand that my dissertation may be made electronically available to the public.

INVESTIGATIONS ON FLOW AND FLOW-INDUCED VIBRATION OF CANDU FUEL BUNDLES

Alokendu Bhattacharya

Doctor of Philosophy, 2013

Program of Mechanical and Industrial Engineering, Ryerson University

ABSTRACT

Excitations induced by three-dimensional unsteady flows of ordinary water coolant through a string of CANDU fuel bundles in a fuel channel are investigated in this thesis. Several comprehensive computational fluid dynamics (CFD) models are developed and solved by means of large eddy simulation (LES), high performance computers and parallel processing scheme. The 12-bundle flow model is the first ever developed concerning flow in a very complex CANDU fuel channel. The lateral fluid flow and flow-induced excitations on every fuel bundle are obtained and analyzed for various combinations of bundle angular positions. The coherent nature of the flow through the multiple bundles inside the fuel channel exhibiting fluid excitations of frequencies spreaded over a wide band in the power spectra is a source of bundle lateral vibration. The flow features of different bundle regime are correlated both in time and frequency domain and they are sensitive to the bundle-to-bundle angular position. This finding directs that, to study the flow and flow-induced excitations and vibrations of a bundle string, it is necessary to include all bundles for fluid-structure interactions. Results from the computational model reveal that the misaligned interface

changes the flow pattern in the fuel channel. The mean lateral fluid forces increase by an order of magnitude and their RMS values raise about 3 to 4 times at some configurations compared to fully aligned situation. Experiments are also performed using the simulated CANDU bundles in an out-reactor setup to verify the computational results. An analysis of a complete fuel channel of a nuclear reactor using LES is at the forefront of current research worldwide and this study is a major step forward towards understanding and unfolding the fuel bundle vibration phenomenon.

ACKNOWLEDGEMENTS

I would like to take the opportunity to express my sincere gratitude to my supervisor, Dr. Shudong Yu, for including me in his research team and for his invaluable guidance, continued patience and tireless support throughout the course of my doctoral program. I would also like to extend my sincere thanks to Dr. Greg Kawall, for all the support and advice he provided during the initial years of my research. I am thankful to the other members of the dissertation committee, Dr. Alagan Anpalagan, Dr. Marwan Hassan, Dr. David Greatrix, Dr. Wey leong, Dr. Hua Lu and Dr. Ahmad Ghasempoor for their efforts in reviewing the thesis and providing valuable comments to improve the quality of dissertation. Thanks are due to Mr. Joseph Amankrah and Mr. Andrew Heim for their co-operation in preparing the experimental setup. I also acknowledge the excellent support from Dr. Hartmut Schmider and Mr. Chris MacPhee concerning the use of computing facilities at HPCVL, Queens University, Canada. The financial supports from NSERC, Ryerson University and SNC Lavalin Nuclear Inc. are gratefully acknowledged.

To my friend and colleague, Xuan Zhang, I extend my sincere appreciation for his support and valuable suggestions on various technical aspects and also sharing some lighter moments whenever required. Thanks to Ravi Peri, Farzin Abbasian, Aminul Haque, Mo Fadaee and Richard Rishon for their assistance in carrying out the experimental work and sharing some good healthy time in the lab to ease the work load during the course of my study.

I also like to express my kind appreciation to Dr. Sumit Goswami, Mr. Asis Kumar Bhaumik, Mr. Shishir Bhattacharyya, Dr. Pranab Kumar Bagchi, Dr. N. C. Singhal, Dr. J. P. Narayan, Dr. M. L. Sharma, Mrs. Sonali Ray, Md. Anwar Kamal and Dr. Dilip Chakraborty at different stages of my life for their encouragement and support towards my doctoral study. My sincere gratitude goes to Dr. Ashok Kumar of IIT Roorkee for being my supervisor in my Masters study and helping me pursue my doctoral program. I am also grateful to acknowledge the

support I received from my Managers Mehtap Ozcan and John Bowden of Candu Energy Inc. towards finishing my PhD program without any hindrance.

Special thanks are due for my parents-in-law for taking care of my daughter by shouldering lots of responsibilities on my behalf and also for compromising many of their personal commitments due to my study. Last but not the least, I would like to express my deepest gratitude to my parents, my wife and daughter, my brother and his family, for their unending love and support, without which this stage could not have been reached in my life.

TABLE OF CONTENTS

Author’s Declaration for Electronic Submission of a Dissertation.....	iii
Abstract.....	iv
Acknowledgement.....	vi
Table of Contents.....	viii
List of Tables.....	xii
List of Figures.....	xiii
Nomenclature.....	xvii
CHAPTER 1: INTRODUCTION	1
1.1 Background	1
1.1.1 Description of CANDU reactors.....	1
1.1.2 Operating experiences	2
1.1.3 Fuel bundle vibration phenomenon	2
1.2 Literature review	4
1.2.1 Analytical and experimental study.....	4
1.2.2 Approach with computational fluid dynamics	6
1.3 Motivation and objectives of the present research	8
1.4 Methodology and organization of thesis.....	9
1.4.1 Computational approach.....	9
1.4.2 Experimental approach.....	11
1.4.3 Conclusion and future work	12
CHAPTER 2: FLOW MODELING SCHEME INSIDE FUEL CHANNEL.....	13
2.1 Approach for modeling.....	13
2.2 Assumptions made in model building.....	13
2.3 Modeling of a sector of bundle flow	14
2.3.1 Solution of the computational model.....	16

2.3.2	Results	17
2.4	Modeling of a full section bundle flow with the inlet endplate	19
2.4.1	Model description	19
2.4.2	Meshing Scheme.....	21
2.4.3	Domain Partitioning, Boundary Conditions.....	24
2.5	Validation of the results.....	25
2.6	Results	27
2.6.1	Results of z-velocity	27
2.6.2	Flow development after endplate.....	28
2.7	Summary	30
CHAPTER 3: FLOW SIMULATION FOR A 12- BUNDLE FUEL CHANNEL		31
3.1	Introduction	31
3.2	Modeling details and Solution technique.....	32
3.2.1	Description of the flow domain.....	32
3.2.2	Solution scheme.....	32
3.2.3	Computational resource.....	33
3.3	Validation	34
3.4	Results	34
3.4.1	Velocity contours at various interfaces.....	35
3.4.2	Velocity vectors at various interfaces.....	38
3.4.3	Time histories for x and y-force for different bundles.....	41
3.4.4	Discussion on x-force (F_x).....	42
3.4.5	Discussion on y-force (F_y).....	42
3.4.6	PSDs for the x and y-forces in different bundles	44
3.4.7	PSDs of x-forces	45
3.4.8	PSDs of y-forces	45
3.4.9	Mean and RMS values of x and y-force for different bundles	45

3.4.10	Mean and RMS of x-forces.....	45
3.4.11	Mean and RMS of y-forces.....	46
3.4.12	Correlation study of flow features among different bundles.....	51
3.4.13	Correlation x-velocities and x-forces in time domain.....	53
3.4.14	Correlation x-velocities, x- and y-forces in frequency domain.....	58
3.5	Summary	65
CHAPTER 4: INVESTIGATION ON BUNDLE ANGULAR MISALIGNMENT		67
4.1	Computational study	67
4.1.1	Introduction.....	67
4.1.2	Description of flow domain.....	68
4.1.3	Flow domain discretization	69
4.1.4	Solution technique and Computational resource.....	71
4.1.5	Validation and grid sensitivity study.....	71
4.1.6	Bundle-to-bundle angular misalignment	71
4.1.7	Results	72
4.1.7.1	Discussion on y-velocities	74
4.1.7.2	Discussion on x-velocities	74
4.1.7.3	Tangential velocity.....	74
4.1.7.4	Radial velocity.....	75
4.1.7.5	Lateral fluid forces	75
4.1.7.6	Effect of angular misalignment	79
4.1.7.7	Pattern of flow shown by pathlines	79
4.1.7.8	Pattern of flow shown by in-plane velocity vectors	81
4.1.7.9	Mean and RMS values lateral fluid forces.....	83
4.1.8	Findings from the computational study	86
4.2	Experimental study	87
4.2.1	Introduction.....	87

4.2.2	Description on test facility.....	87
4.2.3	Experiments	90
4.2.4	Results and Discussions	94
4.2.4.1	Stationarity of recorded vibration signals	94
4.2.4.2	Acceleration measurements	97
4.2.4.3	Displacement measurements	100
4.2.4.4	Acceleration PSDs	102
4.2.4.5	Displacement PSDs.....	102
4.2.4.6	Effect of Angular Misalignment on Bundle Acceleration response	106
4.2.4.7	Effect of Angular Misalignment on Bundle Displacement response	108
4.2.4.8	Effect of Flow Velocity on Bundle Response at Various Angular Misalignment.....	110
4.2.5	Findings from the experimental work.....	111
4.3	Summary	111
CHAPTER 5: CONCLUSION.....		112
5.1	Conclusion.....	112
5.2	Major Accomplishments	113
5.3	Significance of this research.....	113
5.4	Future work	114
APPENDIX		116
REFERENCE		125

LIST OF TABLES

Table 2-1 Details of grids used in grid study.....	15
Table 2-2 Mesh details and time step specifications.....	23
Table 2-3 Information of boundary layers at various segments.....	23
Table 4-1 Flow parameters at different mean flow velocities.....	70
Table 4-2 Mean and RMS values of fluid forces on the first bundle at different misalignment angles.....	85
Table 4-3 Flow parameters at different speed settings for 25.6° misalignment.....	93
Table 4-4 The mean and RMS values of acceleration and displacement at mass flow rate of 17.97 kg/s for different angular orientations.....	100

LIST OF FIGURES

Fig. 1-1 A fuel channel (top); fuel elements and endplate details (bottom).....	1
Fig. 1-2 Scope of several computational models of the present study.	10
Fig. 2-1 Cross-section of the flow domain for a 60° sector of fuel bundle.	15
Fig. 2-2 Normalized time-averaged streamwise velocity (U/U_{max}), around the middle outer element with plots from various models used in grid study.	18
Fig. 2-3 Normalized time-averaged streamwise velocity (U/U_{max}), around the middle outer element.	18
Fig. 2-4 Computational domain for the basic bundle structure model.	20
Fig. 2-5 Fuel element numbering scheme (a) and endplate components (b).	20
Fig. 2-6 Mesh discretization along the axial direction of the flow domain.....	21
Fig. 2-7 Exploded view of meshes for the bundle (a), and endplate subchannels (b).	24
Fig. 2-8 Comparison of axial velocity contours around a middle-ring-element for the present simulation, as shown in (a), with the measurement performed by D’Arcy and Schenk (1987), as shown in (b).	26
Fig. 2-9 Contours of z-velocity normalized by corresponding U of 2.4 m/s for different axial locations at U of 2.4 m/s.	27
Fig. 2-10 Pathlines showing development of fluid flow with sources encircled when viewed from downstream side.....	28
Fig. 2-11 Pathline showing development of flow at different time instants for U of 2.4 m/s, (a) viewed straight from outlet side, (b) and (c) viewed from different angles.	29
Fig. 3-1 Different models with interface misalignment and other details shown.	33
Fig. 3-2 Contours of velocity magnitude at the interface between BD-4 & 5.	36
Fig. 3-3 Contours of velocity magnitude at the interface between BD-8 & 9.	37
Fig. 3-4 In-plane radial velocity vectors (10x scale).	38
Fig. 3-5 Zoom-in view of in-plane radial velocity vectors.	39

Fig. 3-6 In-plane tangential velocity vectors (10x scale).....	40
Fig. 3-7 Zoom-in view of in-plane tangential velocity vectors.	41
Fig. 3-8 Time histories of the x-force on different bundles.	43
Fig. 3-9 Time histories of the y-force on different bundles.	44
Fig. 3-10 PSD values of x-forces on different bundles.	47
Fig. 3-11 PSD values of y-forces on different bundles.	48
Fig. 3-12 Mean and RMS values of x-force on the different bundles.	49
Fig. 3-13 Mean and RMS values of y-force on the different bundles.	50
Fig. 3-14 Different bundle-pair combinations for correlation study: (a) BD-1 with BD-1 to BD-12; (b) BD-6 with BD-1 to BD-12; (C) BD-4 & BD-5, BD-4 & BD-3, BD-5 & BD-6, BD-8 & BD-9, BD-8 & BD-7, BD-9 & BD-10; (P) Progressively incremented combinations: BD-1 & BD-2, BD-2 & BD-3, BD-3 & BD-4, ..., BD-11 & BD-12.	54
Fig. 3-15 Correlation plots of x-velocities from Model-1: (a) BD-1 with other bundles; (b) BD-6 with other bundles; (c) Bundles located near the misaligned interfaces in Model-2.....	56
Fig. 3-16 Correlation plots of x-velocities from Model-2: (a) BD-1 with other bundles; (b) BD-6 with other bundles; (c) Bundles located near the misaligned interfaces.	57
Fig. 3-17 Correlation plots of x-velocities for bundle-pair combination “P”: (a) from Model- 1; (b) from Model-2.	58
Fig. 3-18 Correlation plots of x-forces for bundle-pair combination “P”: (a) from Model-1; (b) from Model-2.	59
Fig. 3-19 Flow coherence plots for x-velocities from Model-1: (a) BD-1 with other bundles; (b) BD-6 with other bundles; (c) Bundles located near the misaligned interfaces in Model-2....	61
Fig. 3-20 Flow coherence plots for x-velocities from Model-2: (a) BD-1 with other bundles; (b) BD-6 with other bundles; (c) Bundles located near the misaligned interfaces.	62
Fig. 3-21 Flow coherence plots for x-velocities for bundle-pair combination “P”: (a) from Model-1; (b) from Model-2.	63

Fig. 3-22 Flow coherence plots for x-forces for bundle-pair combination “P”: (a) from Model-1; (b) from Model-2.....	64
Fig. 3-23 Flow coherence plots for y-forces for bundle-pair combination “P”: (a) from Model-1; (b) from Model-2.....	65
Fig. 4-1 Configuration of endplate and fuel-element with angular misalignment shown.....	68
Fig. 4-2 Entire computational domain with boundary condition indicated.....	69
Fig. 4-3 Illustration of meshing scheme.....	69
Fig. 4-4 Different angular misalignment configurations with 5° increments.....	73
Fig. 4-5 Contours of y-velocity normalized by corresponding U at different axial locations for U of 2.4 m/s.	76
Fig. 4-6 Contours of x-velocity normalized by corresponding U velocity at different axial locations for U of 2.4 m/s.	76
Fig. 4-7 Contours of tangential-velocity normalized by corresponding U at different axial locations for U of 2.4 m/s.	77
Fig. 4-8 Contours of radial-velocity normalized by corresponding U at different axial locations for U of 2.4 m/s.	77
Fig. 4-9 Time histories and PSDs of x-force (side force) and y-force (lift force) for the first bundle for U of 2.4 m/s and 4.8 m/s.....	78
Fig. 4-10 Pathlines showing development of fluid flow with sources indicated by black dots when viewed from downstream side for aligned interface.	80
Fig. 4-11 Pathlines showing development of fluid flow with sources indicated by black dots when viewed from downstream side for misaligned interface.	81
Fig. 4-12 In-plane velocity vectors (scale 20x) at locations before and after the interface.....	82
Fig. 4-13 Zoomed view of in-plane velocity vectors.	83
Fig. 4-14 Comparison of x-force and y-force for aligned and misaligned interfaces.....	84
Fig. 4-15 Mean and RMS values of x and y-force on the first bundle at different alignments...	86
Fig. 4-16 An out-reactor experimental setup.....	87

Fig. 4-17 Side view of a simulated 43-element fuel bundle.	88
Fig. 4-18 Locations and mountings of accelerometer and displacement sensor.....	89
Fig. 4-19 Present experimental domain with misalignment between bundles explained.....	91
Fig. 4-20 Different angular misalignment configurations in the bundle-to-bundle interface region.	92
Fig. 4-21 Repeatability checking shown by time histories and PSDs of measured acceleration and displacement responses.....	94
Fig. 4-22 Plots showing variation of mean values at various mass flow rates.....	95
Fig. 4-23 Plots showing variation of standard deviations at various mass flow rates.	96
Fig. 4-24 Time histories of acceleration response for the inlet sensor at mass flow rate of 17.97 kg/s for different angular orientations.....	98
Fig. 4-25 Time histories of acceleration response for the middle sensor at mass flow rate of 17.97 kg/s for different angular orientations.....	99
Fig. 4-26 Time histories of displacement response for the inlet sensor at mass flow rate of 17.97 kg/s for different angular orientations.....	101
Fig. 4-27 PSDs of acceleration response for the inlet sensor at mass flow rate of 17.97 kg/s for different angular orientations.....	103
Fig. 4-28 PSDs of acceleration response for the middle sensor at mass flow rate of 17.97 kg/s for different angular orientations.....	104
Fig. 4-29 PSDs of displacement response at mass flow rate of 17.97 kg/s for different angular orientations.	105
Fig. 4-30 Mean and RMS values of acceleration response at various angular orientations for different mass flow rates.....	107
Fig. 4-31 Mean and RMS values of displacement response at various angular orientations for different mass flow rates.....	109
Fig. 4-32 RMS values of acceleration and displacement response at various mass flow rates for different angular orientations.....	110

NOMENCLATURE

C_{ij}	Cross stress tensor
C_s	Smagorinsky constant
D	pipe inner diameter (m)
d	fuel element diameter (m)
D_h	hydraulic diameter (m)
p	pressure (Pa)
L_{ij}	Leonard tensor
L_e	entrance length
l	turbulent characteristic length
R_{ij}	Reynolds subgrid tensor
Re	Reynolds number
r	local radial coordinate
$S_{i,j}$	strain rate tensor (1/s)
t	time (s)
u_τ	friction velocity $(\tau_w / \rho)^{1/2}$ (m/s)
u'	turbulent characteristic velocity (m/s)
U	mean axial flow velocity at pipe inlet (m/s)
v	Kolmogorov velocity scale (m/s)
x	horizontal coordinate
y	vertical coordinate

y^+	dimensionless cell distance from the wall ($u_\tau y / \nu$)
z	axial coordinate

Greek symbols

δ_{ij}	Kronecker delta
η	Kolmogorov length scale (m)
μ	Dynamic viscosity ($\text{kg}\cdot\text{m}^{-1}\cdot\text{s}^{-1}$)
ν	kinematic viscosity, μ/ρ ($\text{m}^2\cdot\text{s}^{-1}$)
ρ	density ($\text{kg}\cdot\text{m}^{-3}$)
$\tau_{i,j}$	subgrid-scale stress tensor ($\text{m}^2\cdot\text{s}^{-2}$)
τ	Kolmogorov time scale (s)
τ_w	wall shear stress ($\text{kg}\cdot\text{m}^{-1}\cdot\text{s}^{-2}$)
ϕ	azimuthal coordinate
Δ	grid size (m)
$\bar{\Delta}$	filter length or cubic root of cell volume (m)

Abbreviations

BD	Bundle
CANDU	CANada Deuterium Uranium
CE	Central Element
CFD	Computational Fluid Dynamics

DNS	Direct Numerical Simulation
DSGS	Dynamic Sub-grid Scale
IRE	Inner Ring Element
LETOT	Large Eddy Turn Over Time
LES	Large Eddy Simulation
MRE	Middle Ring Element
ORE	Outer Ring Element
PSD	Power Spectral Density
RMS	Root Mean Square
RSM	Reynolds Stress Model
RANS	Reynolds Average Navier-Stokes
SGS	Sub-Grid Scale
URANS	Unsteady Reynolds Average Navier-Stokes

CHAPTER 1: INTRODUCTION

1.1 Background

1.1.1 Description of CANDU[®] reactors

A typical CANDU reactor core consists of a few hundred horizontally laid fuel channels. A string of fuel bundles are placed inside the pressure tube in each of these fuel channels. The downstream fuel bundle is supported by a stopper or shield plug to hold all fuel bundles at their designed positions against the hydraulic drag, as shown in Fig. 1-1. A CANDU-6 bundle consists of 37 fuel elements of which 18 are located in the outer ring, 12 in the middle ring, 6 in the inner ring and one at the centre (Fig. 1-1). All fuel elements are welded to the two endplates to form an integral fuel bundle structure. During operations, heat generated from fuel bundles is brought out by the flowing heavy water coolant for steam generation. Each bundle weighs about 22 kg.

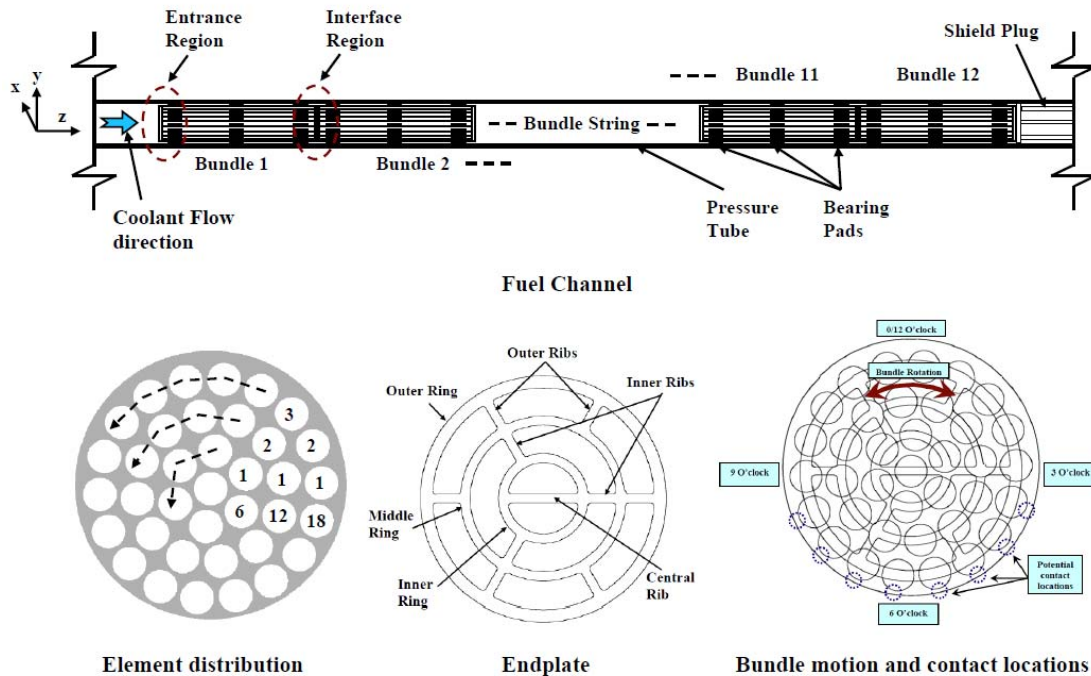


Fig. 1-1 A fuel channel (top); fuel elements and endplate details (bottom).

[®] CANada Deuterium Unranium , a registered trade mark of Atomic Energy of Canada Ltd.

1.1.2 Operating experiences

During normal reactor operations, vibration of the fuel bundles induced by flow is observed. From the inherent design of the CANDU bundle and the fuel channel, the horizontally-laid bundles can have various types of small scale motion inside a pressure tube - rolling, sliding and bending vibration with respect to the designed equilibrium positions. However, it can induce impact or rubbing between the bundle outer surfaces and the pressure tube inner wall. Over a long period of time (almost decades), these bundle motions can cause wear and material loss from the pressure tube wall which is called fretting wear. It would be worth mentioning right at this point that, in reality, the fuel channel system is highly pressurized single phase flow in order to achieve the maximum possible turbulence of the coolant in the bundle subchannels so that heat transfer rate is maximized. Still there might be some minor leakages in the system which could lead to some bubble formation inside, which however, is not desirable.

Under operating conditions, unsteady coolant flow through fuel bundles were known to cause moderate to severe fretting marks on the inside surfaces of the pressure tube between the 4 o'clock and 8 o'clock positions (Judah, 1992; Norsworthy et al., 1994; Norsworthy and Ditschun, 1995). According to a survey of the commercial reactors (Stewart, 1992), fretting marks on the pressure tube inner wall were present in all fuel channels and were the worst near the inlet bundles.

1.1.3 Fuel bundle vibration phenomenon

Flow-induced vibration (FIV) mechanisms which are relevant to nuclear reactor components are: fluidelastic instability, vortex shedding, turbulence-induced excitation and acoustic resonance.

The fluid-elastic instabilities result from coupling between fluid-induced dynamic forces and the motion of structures. Instability occurs when the flow velocity is sufficiently high so that the energy absorbed from the fluid forces exceeds the energy dissipated by damping. The fluid-elastic instability usually leads to excessive vibration. The minimum velocity at which instability occurs is called the critical velocity for fluid-elastic

instability. Since, the flexural rigidity of components such as piping and fuel elements is relatively large, the flow velocities are much lower than the critical velocity. The details on the fluid-elastic instability are documented by researchers (Blevins, 1993; Au-Yang, 2001; Paidoussis, 1966, 2004). Earlier studies, both analytical and experimental, have shown that for fuel bundles, fluid-elastic instability is not a driving factor since the mean flow velocity in the bundle is much less than the critical value, required for instability to occur (Paidoussis, 2004; Zhang and Yu, 2008).

Vibration induced by the vortex shedding is another form of flow-induced structural motion. A structure (e.g., a cylinder) when subjected to cross-flow, sheds vortices alternatively from one side and then the other which exerts varying pressure distribution on the structure, causes net fluctuating reaction forces. When the natural frequency of the structure, corresponding to lateral structural movement in the direction of the flow, matches the vortex shedding frequency, a phenomenon called lock-in occurs resulting in an amplified vibration. The flow inside a fuel bundle structure was earlier regarded as parallel flow (Pettigrew, 1993; Blevins, 1993). However, the flow in the inlet endplate subchannels and bundle-to-bundle interface regions are practically cross-flow (Abbasian et al., 2009; Zhang and Yu, 2011; Bhattacharya et al., 2011a; Bhattacharya et al., 2012).

The fuel bundle vibration may be caused by turbulence. Turbulence-induced excitation generates random pressure fluctuations around the surface of a component. Turbulence-induced excitation was considered to be the principal vibration excitation mechanism in axial flow since the flow velocity in the fuel bundles falls in the subcritical region. Therefore, it was believed that turbulence-induced excitations may produce enough bundle vibration to cause wear in the supporting tube. However, Yetisir and Fisher (1997) pointed out that the small scale parallel-flow turbulence alone is not sufficient to produce the required level of bundle vibration and work-rate for the observed fretting marks on the pressure tube surface. Moreover, some recent studies report that the mixed parallel and cross flow through the various bundle subchannels and bundle interfaces can act as a potential source of FIV of fuel bundles (Zhang and Yu, 2011; Bhattacharya et al., 2011a; Bhattacharya et al., 2012).

The acoustic pressure pulsations, originating from the pumps or acoustic noise generated by piping elements such as valves can excite acoustic resonances in a receptive component of the piping system. If the acoustic resonance frequency is close to that of the component, significant vibration may occur. The possible damage due to acoustic pulsations can be reduced to some extent by modifying the system components, as documented by Misra et al., (1994). In this sense, it would be worthwhile to mention that acoustic frequencies exhibit sharp spikes which are easily distinguishable and thus provide scope for necessary modification on the structural design to avoid matching of any such frequencies in order to skip resonance.

1.2 Literature review

1.2.1 Analytical and experimental study

Over the past few decades, research has been conducted in the field of CANDU fuel bundle vibration, emanating from a single element to a complete fuel bundle. However, most of them, during the earlier time, considered fuel bundle vibration as a parallel flow phenomenon. An analytical model was developed for a cluster of cylinders in the axial flow and the fluid coupling terms in the added mass were derived by Chen and Wambsganss (1972) and Chen (1975). In another work by Paidoussis (1982), a thorough study was made on the vibration problem encountered in reactors and reactor peripherals by the axial and the cross flow.

Another aspect of fuel bundle vibration subjected to axial flow is due to the turbulence experienced by the structure. Gorman (1971) modeled the random vibration response of a fuel element in two-phase turbulent coolant flow and came up with a conclusion that higher amplitude vibration is related to the statistical properties of the pressure field surrounding the surface of the fuel element. Paidoussis and Curling (1985) developed an analytical model for vibration of a cluster of cylinders in parallel turbulent flow. They later carried out an experimental investigation on the characterization of the wall pressure fluctuation (Curling and Paidoussis, 1992). The turbulence, the axial velocity and the wall shear stress variation in subchannels around a CANDU-6 bundle were measured through experiments by D'Arcy and Schenk (1987). Pettigrew (1993), in an experimental investigation on CANDU fuel

bundle vibration, reported that the vibration amplitudes increase with the mass flow rates and the recorded RMS values of vibration response was within 10 μm . Yetisir and Fisher (1997) developed an analytical model for a single fuel element subjected to turbulence excitation modeled by random excitation forces applied uniformly on the fuel element. They found that the fuel element vibration due to the flow-induced random turbulent excitation is insufficient by itself to produce the required level of work rate causing the fretting damage observed in some commercial CANDU reactors. Therefore, if turbulence-induced excitations are incapable of producing transverse vibration required to cause observed material loss for a single fuel element, then it is most unlikely for a whole fuel bundle to vibrate only by turbulence. From the investigation of Simth and Derken (1998) on a single CANDU-6 fuel bundle, it has been found that the bundle vibration is a mixture of rolling and bending motion; the unsteady forces acting on the bundle is reduced with the inclusion of the straightener in the inlet.

Some of most recent research work revealed that CANDU fuel bundle flow is very complex (Abbasian et al., 2009; Zhang and Yu, 2011; Bhattacharya et al., 2012). This is due to the presence of endplates which consist of several ribs and rings contributing to the generation of some local cross-flow around the entrance of the inlet bundle and interfaces between neighbouring bundles. Bhattacharya et al., (2011a), in an experimental work on simulated 43-element CANDU fuel bundle, observed that the bundle lateral vibration frequency is proportional to the inlet velocity of the flow entering the bundle – an indication of the existence of vortex shedding phenomenon. The effect of bundle angular misalignment has been studied by Vijayan et al. (1999). They carried out experiments to measure the pressure drop across various components of the CANDU reactor fuel channel under single-phase flow conditions. The experimental results indicated that the variation in the bundle alignment at the junction can result a maximum variation of $\pm 6\%$ in the pressure drop across the 13-bundle string in a fuel channel. However, they did not evaluate any effect of misalignment on the bundle response or the fluid excitations. Further work on this area in understanding the bundle flow mechanism and also the cause of bundle vibration inside the whole fuel channel is thus required.

1.2.2 Approach with computational fluid dynamics

Flow inside a CANDU fuel channel is a large scale flow problem. The lack of comprehensive studies of the fuel channel flow in the past was due to the extreme complexities of the flow structure and the large computational demand of the problem. With the rapid advancement in the computing technology and parallel processing technique, numerical solutions for very large scale problem are now possible. Various numerical schemes have been employed in the literature to solve three-dimensional unsteady flow problems. Lee and Jang (1997) investigated the turbulent flow in an array of bare elements by solving the Reynolds Averaged Navier–Stokes (RANS) equations, in conjunction with the non-linear k - ϵ method. Suh and Lightstone (2004) concluded that the k - ϵ method is unable to predict secondary flows inside complex subchannel areas in element-bundle geometry. Chang and Tavoularis (2007) simulated the turbulent flow in a sector of bare elements for a 37-element fuel bundle by solving the Unsteady Reynolds Averaged Navier–Stokes (URANS) equations by means of the Reynolds Stress Model (RSM). They concluded that URANS, supplemented by RSM, has better capability, compared to RANS, in dealing with three-dimensional turbulent flow.

The Large Eddy Simulation (LES) technique was developed in the 1960's for modeling anisotropic turbulence with high accuracy. In LES scheme, the filtered N-S equations are solved in such a way that eddies larger than the mesh size are computed directly, while eddies smaller than the mesh size are modeled implicitly. The advantage of LES is that direct determination of the large eddies yields higher accuracy in modeling the unsteady flow through complex geometries like bundle subchannels because of their geometry-dependency and unsteady nature. The small scale eddies are modeled by sub-grid scale (SGS) modeling. Barsamina and Hassan (1997) concluded that LES is capable of predicting turbulence in complex geometries and may be used as a viable engineering tool with a suitable subgrid scale closure model. Also, in various separate studies, a higher capability of the LES technique among LES, RANS and Direct Numerical Simulation (DNS), in predicting anisotropic turbulence in the case of a densely-packed bundle geometry, was reported (Rollet-Miet et al., 1999; Benhamadouche and Laurence, 2003; Baglietto et al., 2006). In LES applications, the Smagorinsky model is commonly used with a constant, C_s

(Smagorinsky, 1963). This requires the use of additional wall functions in order to dampen the subgrid scale viscosity near the solid boundaries. To resolve this problem, a dynamic subgrid scale (DSGS) model is used (Germano et al., 1991), where the model parameter is dynamically calculated on the basis of the resolved scales. This improvement on the Smagorinsky model was initially proposed by Germano et al. (1991) and then modified by Lilly (1992). Hassan and Barsamian (1999) applied the Smagorinsky model and the DSGS model based on Lilly's modification to a 9 element non-staggered bundle arrangement. They concluded that LES is a good alternative in solving large scale engineering applications with complex geometries. Kim and No (2004) used the pressure fluctuations predicted by LES to perform spectral analyses in bundle flows in various combinations of elements. Merzari and Ninokata (2009) found that LES allows deeper analysis of the flow field in order to obtain additional insight into element-bundle structure. Abbasian (2009) reported that the instantaneous and mean flow characteristics obtained by the anisotropic model, like LES, contains more accurate predictions of the flow behavior in terms of span-wise flow regimes and flow variable fluctuations, unlike k- ϵ approach. Hence LES scheme is one of the most suitable approaches which can be implemented to the CANDU type bundle flow modeling and therefore, the present study considers the LES approach for all flow modeling.

Abbasian et al. (2009) studied a simulated 43-element fuel bundle with endplates, and found that flow through a set of parallel elements is entirely different from the coolant flow through the same set of elements with endplates. They also noticed the formation of large eddies and swirling flow behind the inlet endplate. In some other interesting works, it has been observed that endplates are one of the major sources for the bundle transverse vibration (Zhang and Yu, 2011; Bhattacharya et al., 2012a). Very recently, Bhattacharya et al., (2011b), Bhattacharya and Yu (2012a), Bhattacharya and Yu (2012b) found that the angular misalignment between neighbouring bundles can significantly increase the bundle transverse motion induced by the flow and also the lateral fluid excitations on the fuel bundles.

It is known that for any structure to be excited it takes two, i.e., both the excitation frequency and the structural mode should match in order to produce a non-zero joint

acceptance between these two factors. Now, since the fuel bundles or the string of fuel bundles vibrate inside the fuel channel meaning that there has to be some sources of excitation which combines with the structural modes to provide the energy of vibration to the fuel bundle system. The present study is mainly aimed towards understanding the possible sources of potential fluid excitations in a much comprehensive manner.

Therefore, the mixed cross and parallel flows in the entrance region and the bundle-to-bundle interface regions appear to be responsible for producing the large amplitude flow excitations. The flow inside the fuel bundle subchannels is responsible for connecting and forming a very complex and coherent flow pattern inside the bundle-filled fuel channel. For the present investigation, it was found that to properly identify the true flow-induced fuel bundle vibration mechanism, it is necessary to include the entire string of fuel bundles and the pressure tube for modeling the fluid flow (Bhattacharya and Yu, 2013) and the fluid-structure interactions in the CFD models.

1.3 Motivation and objectives of the present research

First, since the flow through various subchannels inside the fuel channel has continuity across the bundles, fluid entering the inlet bundle is correlated with the fluid exiting the outlet bundle. From what is described in the last and the penultimate paragraph of the previous section, it is clear that for identifying the actual fluid excitations on fuel bundles, the entire length of fuel channel should be modeled with multiple bundles placed inside. However, this has not been undertaken in past studies and hence, the inclusion of this new approach is the primary motivation of the present research study.

Secondly, while modeling the flow for a string of 12 bundles, there may be situations when fuel bundles are not fully aligned to each other. This brings about an important aspect which is: the possible effect of bundle-to-bundle angular misalignment on both the fuel bundle vibration and the lateral fluid excitations. Thus, a thorough investigation focusing on bundle angular misalignment is of importance which drives another part of the present research work. The above aspects ultimately provides the basis for the following objectives that frame the present study,

- To develop a comprehensive fluid model of coolant flow through a string of CANDU fuel bundles with endplates inside a fuel channel and to obtain the individual fluid excitations in each bundle for combinations of hypothetical angular misalignments;
- To evaluate the effects of bundle-to-bundle angular misalignments on unsteady fluid forces, which are responsible for fuel string vibration;
- To investigate experimentally the vibration of a short string of simulated fuel bundles with various angular misalignments in a water loop to find the FIV mechanism and also to analyze effect of bundle angular misalignments on the FIV.

1.4 Methodology and organization of thesis

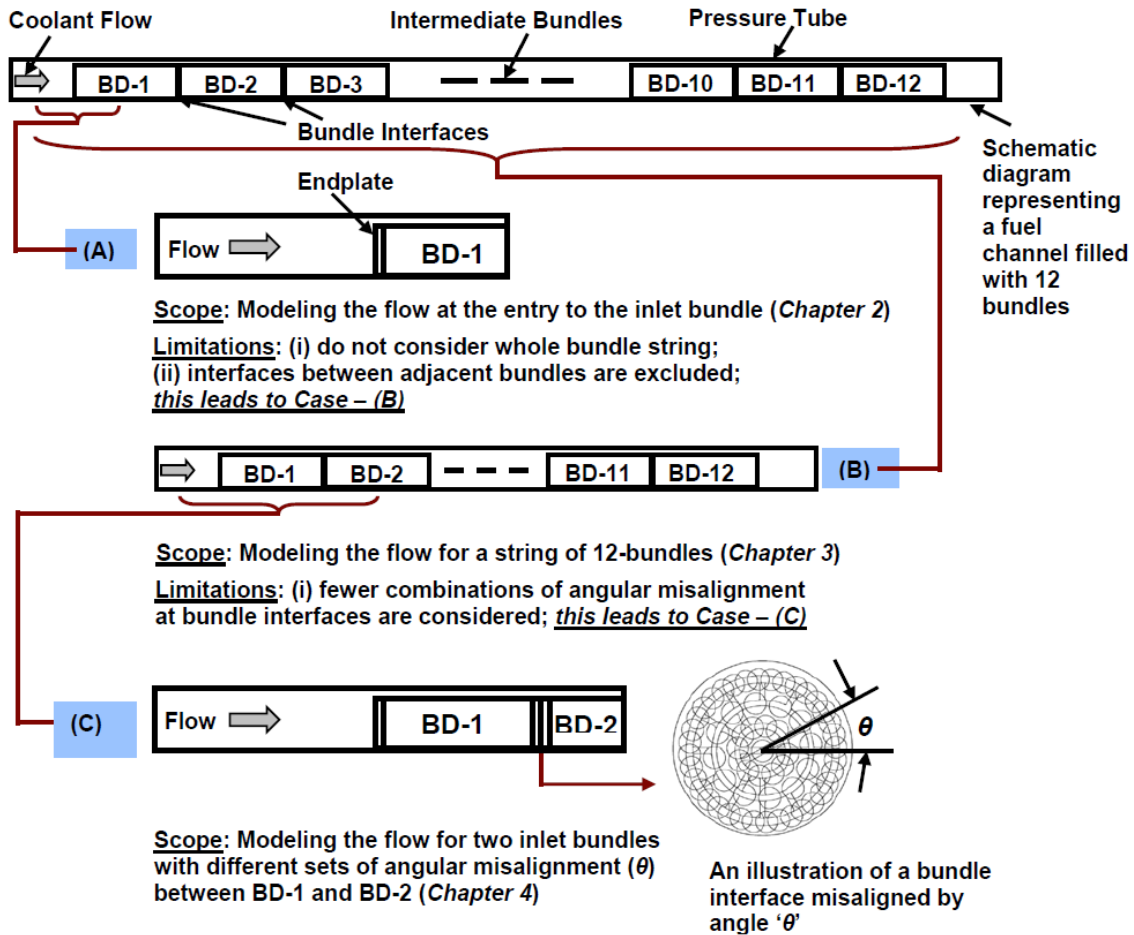
To deliver on the objectives of the thesis, both computational and experimental approaches are taken. Detailed methodologies of these approaches are outlined below.

1.4.1 Computational approach

As shown in Fig. 1-2, the flow through a 12-bundle string fuel channel consists of the following distinctive regions: (a) entry to the inlet bundle, (b) interfaces between neighboring bundles, where the fluid particles, due to the bundle geometry, flow in a very complex manner like mixed cross and parallel flow. This leads to enhancement of the lateral fluid force acting on the bundles and ultimately higher bundle side-to-side motion. Therefore, to understand the bundle flow mechanism accurately, flow should be modeled for multiple bundles, possibly for a complete fuel channel. The methodology considered in this research work is schematically presented in Fig. 1-2 where, the scope, the domain and the limitations of different models are elaborated.

The aim to execute the objectives of the research is to model the complete fuel channel flow with an accurate solution technique. However, it would be appropriate to develop a smaller version of the full channel CFD model with a certain meshing scheme and solution strategy first and then compare the results before implementing the similar modeling and solution scheme to the 12 bundle model. To achieve this, a CFD model for a 60° sector of the 37-element CANDU bundle without the endplates is presented and solved with the LES

numerical scheme, in association with the Smagorinsky (1963) SGS model. A grid sensitivity study has been performed to examine the accuracy of the present grid. The results from this work are compared with the work done by Chang and Tavoularis (2007). Then the computational approach is extended to a half bundle CFD model by considering a clear pipe zone, an interim endplate zone and half of the first bundle zone in the flow model (refer to Case-A of Fig. 1-2). The results from this model are compared with the experimental work of D’Arcy and Schenk (1987). This preliminary work, as described in Chapter 2, is an establishing step of the computational and solution technique being adopted for the CFD models which will provide confidence before extending it to a 12 bundle CFD model.



Cases (A), (B) and (C) collectively will be able to deliver the overall objectives of the thesis.

Fig. 1-2 Scope of several computational models of the present study.

At this juncture, the already tested computational scheme can be extended for a larger flow domain with 12 bundles placed inside a fuel channel. The physical domain for which this numerical model is created represents different cases with various angular misalignment combinations at the bundle-to-bundle interfaces, as sketched in Case-B of Fig. 1-2. The idea of this study is to have an overall view on the fluid flow and its lateral excitations on each of the bundles with several bundle misalignment combinations out of numerous possible hypothetical angular misalignments at different interfaces in a complete fuel channel. This is one of the most significant attempts made to date in regards to capturing comprehensively the flow and its characteristics in the whole fuel channel for a CANDU type reactor. Chapter 3 discusses various aspects of this study with much detail.

From the inherent design of the CANDU fuel channel, there could be countless different combinations of angular misalignment out of the 11 bundle interfaces in a single fuel channel filled with 12 bundles. Both developing and solving CFD models with so many combinations are hard to execute practically, as well as being computationally demanding. Therefore, the investigation on the effect of angular position on the lateral fluid excitations is carried out with two bundles only. It may not represent though the true fuel channel model, but surely it will give some light to the phenomenon under examination. The computational scheme for this flow problem is taken from the 12-bundle CFD model. Thus a CFD model is prepared consisting of two inlet CANDU-6 bundles (refer to Case-C of Fig. 1-2); the model can take different misalignment configurations between the two bundles, as presented in Chapter 4. This work expands on the possible effect of bundle-to-bundle angular misalignment on the lateral fluid excitations, and thereby identifies some critical misalignment orientations at which fuel bundle may experience higher lateral fluid forces.

1.4.2 Experimental approach

Ideally, a test loop with 12 bundles placed in it should be used for the experimental study. But due to various limitations e.g., space, driving pump etc., the experiments could be carried out with only two simulated bundles within the currently available resources at the Vibration Research Facility of Ryerson University. Hence, to examine the bundle vibration induced by the fluid flow, experiments are carried out in an out-reactor setup with water as

flowing fluid, and placing two simulated 43-element CANDU fuel bundles inside the test loop. The experiments are focused on the possible effect of angular misalignment on the bundle lateral response, as discussed in detail in Chapter 4. Thus, Chapters 2, 3 and 4 collectively will deliver the material and the results that meet the objectives of the present research study

1.4.3 Conclusion and future work

The findings from the present research study are summarized in Chapter 5. Some possible avenues for expanding the current work, towards achieving the larger goal to addressing the fuel bundle vibration induced by the flow in a more comprehensive way, are also provided in Chapter 5.

CHAPTER 2: FLOW MODELING SCHEME INSIDE FUEL CHANNEL

The flow regime inside the fuel channel where heavy water fluid particles travel from the clear pipe zone to an entirely different and complex bundle subchannels through a number of thin endplates in the interface zones is of importance to this study. The theory behind the development of the computational model and also some idealized flow models will be discussed in this chapter. The scheme adopted for the computational model as elaborated in the coming sections will be generic to the next chapters.

2.1 Approach for modeling

In an ideal situation, the flow domain inside the fuel channel containing 12 bundles with bearing pads and spacer pads attached to them along with the end-fittings at the two ends of the bundle string should be modeled. However, this leads to an enormous and very complicated computational model which might not be feasible practically, at least as of now. Therefore, in this research study, primarily a meshing scheme is developed for a much idealized CANDU-type bundle structure, where, a sector of the whole bundle cross section is produced first with air as fluid in it. This model does not contain any endplate and thus it is representative more to a parallel subchannel flow. Then, the result of this model is validated with existing results already available in the literature. Upon achieving reasonable agreement through this comparison, a small model with pipe flow and half of the inlet bundle flow region is built. This is carried out in order to examine the capability of the model to accurately capture the flow features inside the bundle subchannels before implementing the modeling and solution scheme into a comprehensive computational model with 12 bundles. The result from this simplified model is verified with data available in literature.

2.2 Assumptions made in model building

Like any other research, the present research also has certain assumptions made while developing the computational model. They are as mentioned here.

The first assumption that is made while developing all the computational model is that the boundary of the flow domain, i.e., the walls of the fuel bundle structure, is fixed and hence cannot move. However, in actual practice they are not. Thus, the present computational work lacks to some extent to capture the real flow and the associated fluid-structure interaction phenomenon.

Another important aspect is that in real CANDU bundles, the bearing pads and the spacer pads are installed to support the bundle inside the pressure tube and to avoid inter-element impacting, respectively. These pads are not considered while preparing the computational models, to avoid more complexity. It may be useful to mention here that the projected area of obstruction by all 18 bearing pad considered together is in the range of about 2% of the overall pipe flow area. Therefore, influence in changing the bundle subchannel flow pattern is deemed to be minor and hence, neglected in the current study.

It is to be noted that the above assumptions are followed for all the computational models developed in the current research.

2.3 Modeling of a sector of bundle flow

This flow problem contains one sixth of a 37-element CANDU fuel bundle with air as the flowing fluid as studied by Chang and Tavoularis (2007). Periodic boundary conditions are employed in the streamwise and tangential directions. The input parameter at the inlet is a 13 m/s mean flow velocity. The cross-section view of the flow domain of this model is shown in Fig. 2-1. Grid size and quality affect the simulation results. To understand the sensitivities of numerical results on grid sizes, three computational models with different grid size, described in Table 2-1, are created and solved using LES to simulate the parallel flow problem studied by Chang and Tavoularis (2007). The value of Δz is kept to a fixed value of 4 mm because in that direction the flow domain has the longest dimension. Since the highest skewness value of the cell volumes for the three meshes is 0.7, which is less than 0.9 required of a quality grid, the mesh distribution attained is good.

For each of the three meshing schemes, a computational model with one-sixth of the cross section and 0.0262 m length (i.e., $69 D_h$ long; $D_h=0.3799$ mm) is built. Periodic boundary conditions are used on the two radial boundaries. At the inlet, the *velocity* is specified; and at

the outlet, the *outflow* boundary condition is defined. The flow in each subchannel is considered fully developed after about $30D_h$ from the inlet. The basis of this axial length is also supported by the conclusion from Anselmet et al. (2009) and White (2003). They proposed that the entrance region length L_e , which characterizes the longitudinal position beyond which full development of the flow is reached, can be taken as $4.4R_e^{1/6}$ according to White or $1.6R_e^{1/4}$ according to Anselmet et al., where $R_e = UD_h / \nu$ is the global Reynolds number in the duct with hydraulic diameter D_h having a fluid of mean flow velocity U and kinematic viscosity ν . Under normal operating conditions, the Reynolds number varies from 19000 to 79000. Anselmet et al.'s relationship yields an entrance length of $30 D_h$ or 0.0114 m, which is less than 0.0262 m. The length of the computational model is thus justified.

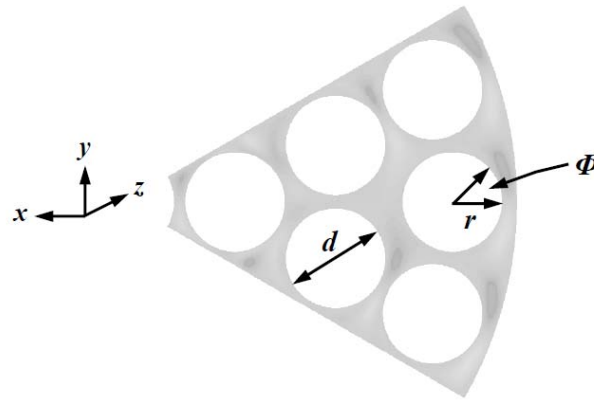


Fig. 2-1 Cross-section of the flow domain for a 60° sector of fuel bundle.

Table 2-1 Details of grids used in grid study.

Mesh	I	II	III
Grid size ($\times 10^6$)	0.638	0.529	0.442
Δr ($\times 10^{-3}$ m)	0.5	0.6	0.7
Δz ($\times 10^{-3}$ m)	4	4	4
Minimum cell volume (m^3)	5.286×10^{-13}	1.586×10^{-12}	1.828×10^{-12}
Maximum cell volume (m^3)	1.719×10^{-7}	3.461×10^{-9}	4.576×10^{-9}

2.3.1 Solution of the computational model

As described earlier, the computational models are solved using the LES scheme. Now, when the LES technique is employed to solve the three-dimensional filtered unsteady N-S equations, flow structures larger than the scaling filters are resolved directly; whereas, subgrid scales are used to model structures smaller than the filter scale (Chung, 2002). The filtered momentum and continuity equations for incompressible flow without body forces can be written as (Sagaut, 2006),

$$\begin{cases} \frac{\partial \bar{u}_i}{\partial t} + \frac{\partial (\bar{u}_i \bar{u}_j)}{\partial x_j} = -\frac{1}{\rho} \frac{\partial \bar{p}}{\partial x_i} + \nu \frac{\partial}{\partial x_j} \left(\frac{\partial \bar{u}_i}{\partial x_j} + \frac{\partial \bar{u}_j}{\partial x_i} \right) - \frac{\partial \tau_{ij}}{\partial x_j} \\ \frac{\partial \bar{u}_i}{\partial x_i} = 0 \end{cases} \quad (i = 1, 2, 3) \quad (1)$$

where, u_i , are the flow velocity components; p is the pressure; ρ is the density; and ν is kinematic viscosity; the over-bar denotes the filtered quantity; and τ_{ij} is the subgrid stress components. Leonard (1974) expressed the subgrid stress term in the form of a triple summation as,

$$\tau_{ij} = L_{ij} + C_{ij} + R_{ij} \quad (2)$$

where, $L_{ij} \left(= \overline{\overline{u_i u_j}} - \overline{\overline{u_i}} \overline{\overline{u_j}} \right)$, $C_{ij} \left(= \overline{\overline{u_i u'_j}} + \overline{\overline{u'_j u_i}} \right)$ and $R_{ij} \left(= \overline{\overline{u'_i u'_j}} \right)$ represent the Leonard tensor, cross-stress tensor and Reynolds subgrid tensor, respectively, with a view to decomposing the non-linear term $\overline{u_i u_j}$ to finally arrive at (Sagaut, 2006),

$$\tau_{ij} = \overline{u_i u_j} - \bar{u}_i \bar{u}_j \quad (3)$$

These are turbulent stresses for grid filters, which can ultimately be determined by filtered velocity fields through interaction among (i) resolved scales transferring energy to small scales, (ii) unresolved scales transferring energy to either large or small scales, and (iii) small scales producing energy from small scales to large scales (Chung, 2002).

In the Smagorinsky subgrid model, the subgrid stress components are modeled as,

$$\tau_{ij} - \frac{1}{3}\delta_{ij}\tau_{kk} = -2(C_s \bar{\Delta})^2 (2\bar{S}_{ij}\bar{S}_{ij})^{1/2} \bar{S}_{ij}$$

$$\bar{S}_{ij} = \frac{1}{2} \left(\frac{\partial \bar{u}_i}{\partial x_j} + \frac{\partial \bar{u}_j}{\partial x_i} \right) \quad (4)$$

where, $C_s \bar{\Delta}$ is the mixing length and C_s is the Smagorinsky constant having a value between 0.1 and 0.2; $\bar{\Delta}$ is the filter length scale or cubic root of the cell volume, i.e., usually the size of the computational grids. In the current study, the value of C_s is taken as 0.1, which is default value in FLUENT.

A cluster of supercomputers, in conjunction with a parallel processing scheme, are utilized to obtain a numerical solution. A steady-state solution is first sought using the k- ϵ method. The converged steady-state solution is subsequently used as the initial condition for obtaining an unsteady state solution with LES.

2.3.2 Results

The time-averaged streamwise velocities (U/U_{max}) around the outer-middle element are compared in Fig. 2-2 for $\phi = 60^\circ$ and $\phi = 180^\circ$ at which data were measured for a longer range of r/d ratios. Here r is the local radial co-ordinate; d is the element diameter; and ϕ is the orientation angle. It is worth mentioning here that these data are taken at locations starting from r/d ratio of 0.514, but not exactly on the element outer surface where a no-slip boundary condition is imposed. It can be seen that for both ϕ values, the simulation results obtained using the present CFD models, with LES approach those of Chang and Tavoularis (2007) as the mesh grid size becomes finer. The present measurements and obtained trend are in good agreement with the already measured trend, but based on the results obtained from balancing the conflicting needs for accuracy and affordability of computations, Mesh-I is adopted for a more comprehensive verification against the independently obtained results in Fig. 2-3. An examination of the results reveals that there is good agreement among the three sets of results independently obtained by experiments and URANS (Chang and Tavoularis 2007), and LES in this study. Only minor differences are observed for $\phi = 120^\circ$ at higher r/d ratios where a small under-prediction is noticed.

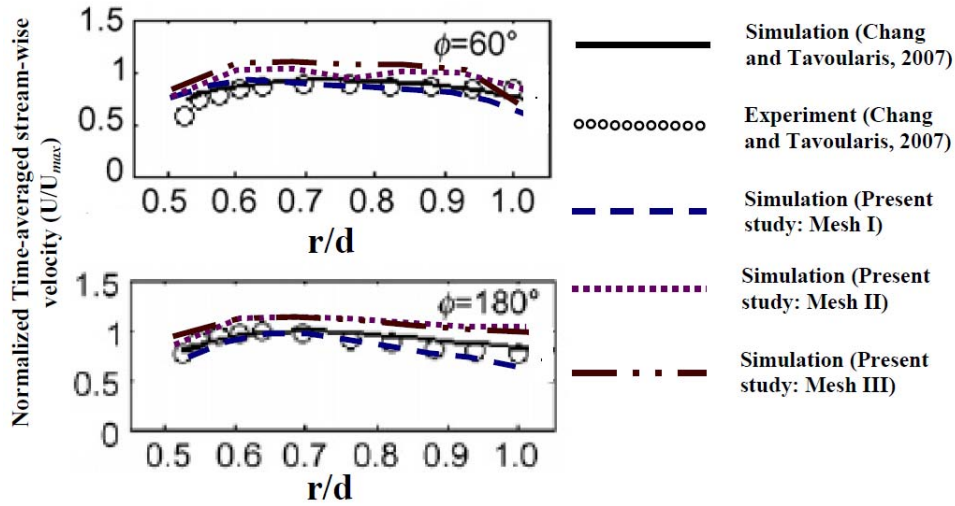


Fig. 2-2 Normalized time-averaged streamwise velocity (U/U_{max}), around the middle outer element with plots from various models used in grid study.

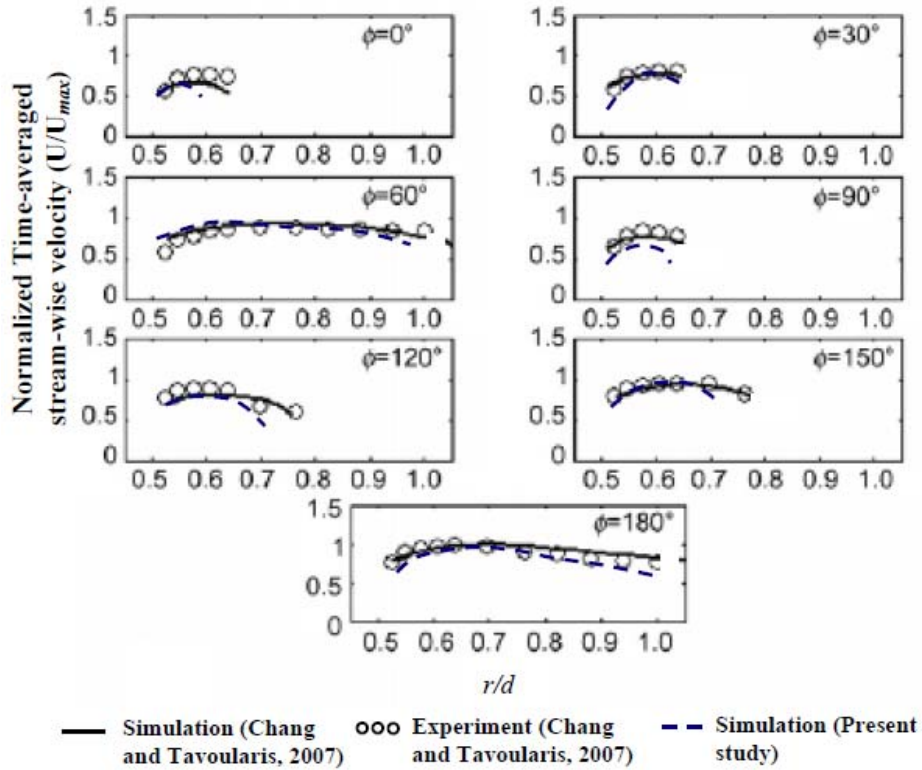


Fig. 2-3 Normalized time-averaged streamwise velocity (U/U_{max}), around the middle outer element.

2.4 Modeling of a full section bundle flow with the inlet endplate

As described at the beginning of this chapter, the flow modeling of a complete CANDU fuel channel is a large-scale complex problem. It would be, therefore, appropriate to test the computational scheme adopted and verified in a 60° sector parallel flow model, as elaborated in section 2.3, for a much simplified flow domain before implementing it into a full scale fuel channel model with 12 bundles. Thus, a small CFD model is developed to examine this issue, which is discussed briefly in the following sub-sections.

2.4.1 Model description

A computational model consisting of (i) a pipe of $6D$ in length, where D is the inner diameter of the pressure tube, (ii) all endplate subchannels formed by the circular rings and radial ribs, (iii) the bundle subchannels formed by fuel element outer surfaces, and (iv) finally the gap subchannels formed between the outer fuel element surfaces and the pressure tube inner surface, is created using GAMBIT and FLUENT to simulate the entrance flow through the inlet fuel bundle in a fuel channel. The entire computational domain along with the flow direction and global coordinates and boundary conditions imposed is shown in Fig. 2-4. The pipe length of $6D$ is required computationally in order for the flow with a specified uniform axial velocity everywhere at the inlet surface to be fully developed before it reaches the first upstream bundle. Details of bundle subchannels along with the fuel element numbering scheme are shown in Fig. 2-5(a). The endplate structure and its subchannels are shown in Fig. 2-5 (b). It should be mentioned that the flow through the upstream bundle structure for the orientation shown in Fig. 2-5 is investigated.

From the Anselmet et al.'s relationship the length at which flow becomes fully developed can be evaluated as 0.240 m and therefore, only the upstream half of the bundle, 0.248 m in length from the inlet endplate, is considered in this model.

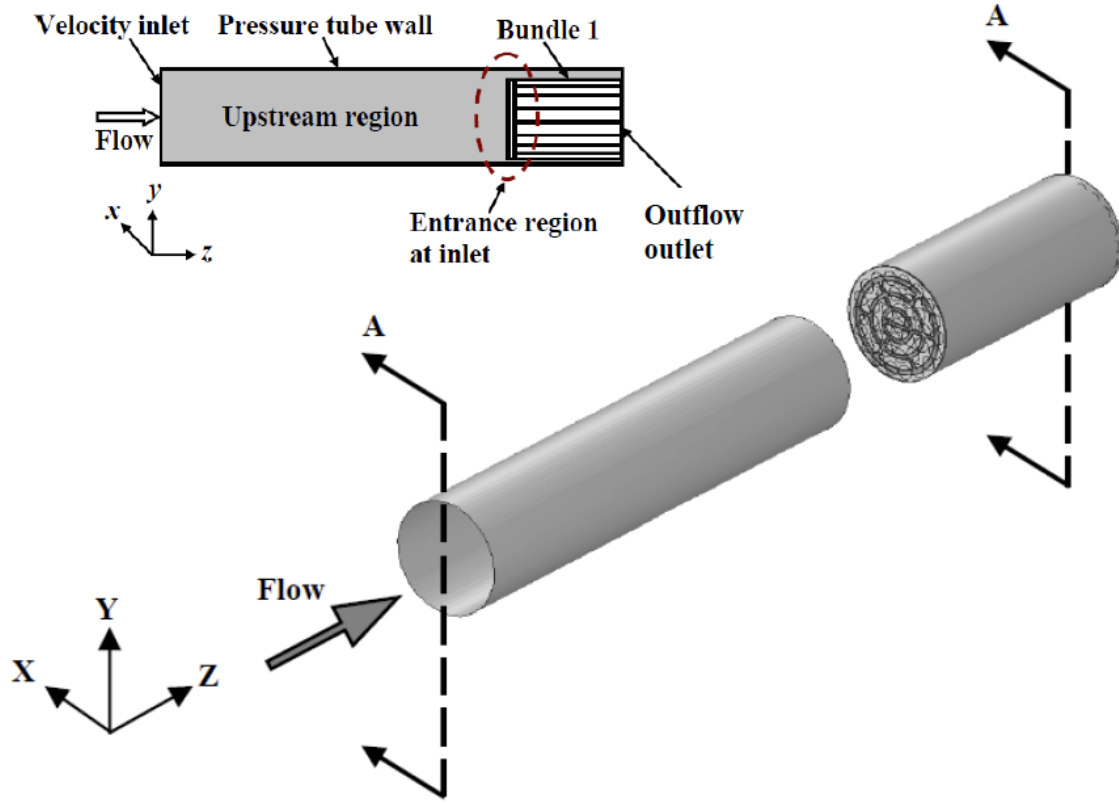
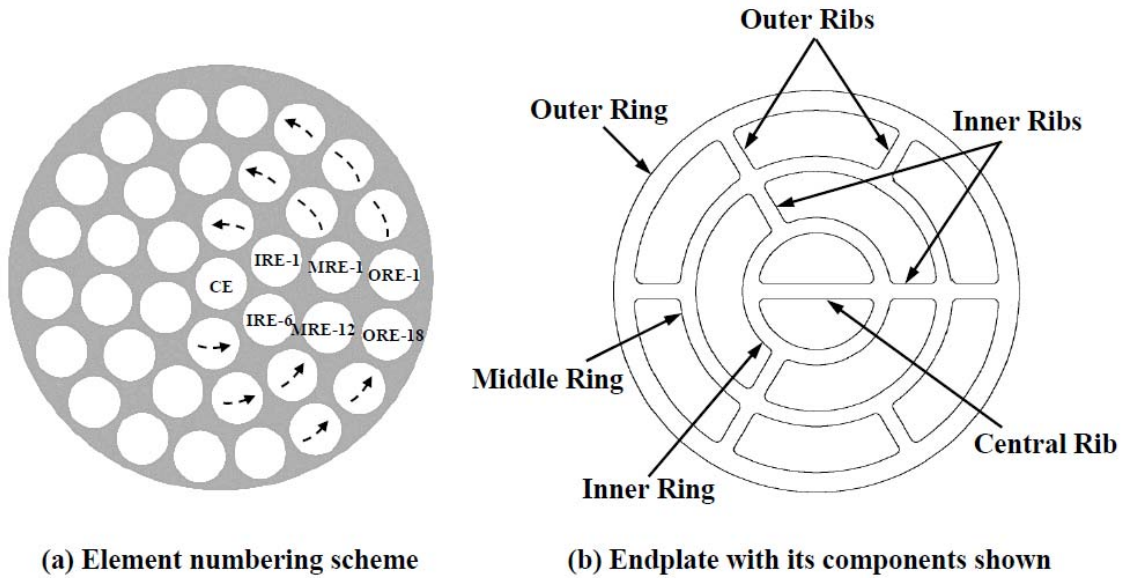


Fig. 2-4 Computational domain for the basic bundle structure model.



(a) Element numbering scheme

(b) Endplate with its components shown

Fig. 2-5 Fuel element numbering scheme (a) and endplate components (b).

2.4.2 Meshing Scheme

A sectional view of the grid in the A-A plane, used for the flow problem in Fig. 2-4, consists of three different regions: the upstream pipe flow, the endplate flow and the bundle flow. As shown in Fig. 2-6, the pipe flow region is divided into two sub-regions. A coarse uniform mesh is used for the sub-region far away from the bundle. A non-uniform mesh is used for the sub-region adjacent to the fuel bundle. A magnification of 1.1 is applied to cells from the upstream endplate to the boundary between the two pipe flow sub-regions. The adjacent regions are then grouped using the non-conformal meshing scheme. The endplate and bundle flow regions contain the finest grid sizes out of the whole fluid domain. The whole computational domain contains about 6.3 millions cells. More details including the radial distribution (Δr) and the axial distribution (Δz) of the grid are given in Table 2-2.

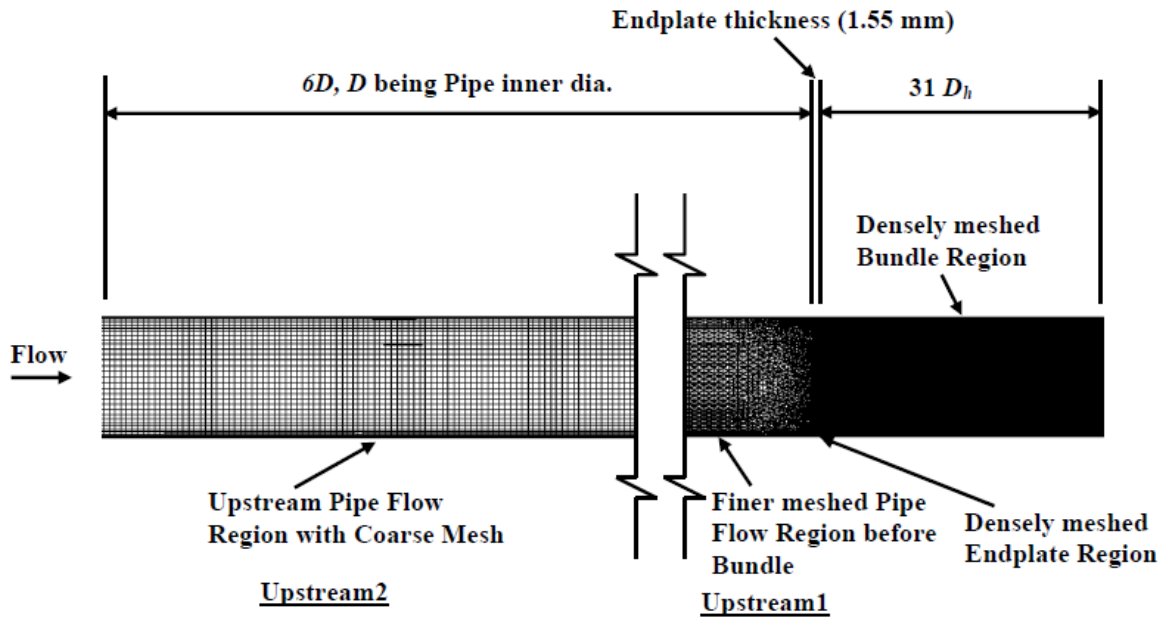


Fig. 2-6 Mesh discretization along the axial direction of the flow domain.

In addition to the LES approach with Dynamic Smagorinsky Model as described in section 2.3.1, the energy equation is added to the solver as follows:

$$\frac{\partial}{\partial t}(\rho e) + \nabla \cdot (\vec{u}(\rho e + p)) = \nabla \cdot (k_f \nabla T) \quad (5)$$

where e is the energy obtained using $e = h - p/\rho$ with h being the enthalpy. Constant specific heat is considered for the present problem, so the enthalpy may be written as $h = c_p T$; k_f is the heat conduction coefficient of the fluid and is taken care of by the solver while defining the temperature and other material properties on the wall surfaces surrounding the fluid domain; and T is temperature. The effect of viscous dissipation and the buoyancy driven forces are neglected assuming that the viscous heating is negligible, and the density does not vary much with temperature. The purpose of adding this energy equation is to model the flow like an in-situ operating condition. Also from the work by Abbasian (2009), one can note that the magnitude of the fluid excitations becomes lower but the RMS values increase. So, it is always better to capture the flow characteristics inside the flow domain with the proper operating conditions as done here.

The accuracy of the LES technique, primarily dependent on the size and quality of the meshes, can be evaluated using the three Kolmogorov microscales - the length scale η , the time scale τ and the velocity scale ν . According to Tennekes and Lumley (1972), the Kolmogorov scales may be determined from the following equations,

$$\eta = l \text{Re}^{-3/4}, \quad \tau = (l/u') \text{Re}^{-1/2}, \quad \nu = u' \text{Re}^{-1/4} \quad (6)$$

where, the Reynolds number $\text{Re} = (uD_h/\nu)$; hydraulic diameter $D_h = 0.0081$ m for the problem; the turbulent characteristic velocity u' , usually taken to be 5 to 10% of the mean flow velocity; and l is the turbulent characteristic length. At a mean axial flow velocity of 2.4 m/s at the inlet, an average mean axial velocity of 6 m/s in bundle subchannels is found, which corresponds to a Reynolds number of 48,600. In the present model, the time scale τ is 2.4×10^{-4} seconds.

Since the near-wall mesh resolution is of critical importance in LES, the thickness of the first layer of cells near a wall must meet the requirement: $y^+ = 1$, which is followed in the current study. Details pertaining to the boundary layer are provided in Table 2-3. The distribution of grids in the xy -plane is shown in Fig. 2-7 for the fuel bundle and endplate

regions. Time step size is another important parameter influencing accuracy of the numerical simulation of turbulent flow (Choi and Moin, 1994). A time step size of 10^{-5} seconds is chosen on the basis of the large eddy turn-over-time (LETOT) or the time scale τ in Eq. (6).

Table 2-2 Mesh details and time step specifications.

Zones (columns) and Parameters (rows)	Bundle region	Endplate region	Upstream region	
			Upstream1	Upstream2
Grid size ($\times 10^6$)	3.34	0.44	1.1	1.4
Grid type	Hexahedral cells	Triangular prism cells	Tetrahedral cells	Hexahedral cells
Δr ($\times 10^{-3}$ m)	0.5	0.5	Near endplate 0.8 and near inlet 4.5	2.5 - 5
Δz ($\times 10^{-3}$ m)	4	0.52		5
LETOT ($\times 10^{-5}$ s)		2.14 - 8.56		
Δt ($\times 10^{-5}$ s)		1		

Table 2-3 Information of boundary layers at various segments.

Zones (columns) and Parameters (rows)	Bundle region	Endplate region	Upstream region	
		Around endplate surfaces	Upstream1	Upstream2
Thickness of first layer ($\times 10^{-6}$ m)	6.55	6.08	8.47	8.47
Growth factor	1.2	1.3	1.3	1.3
Number of layers	12	12	15	15
Total depth of boundary layer ($\times 10^{-4}$ m)	4.868	4.868	14.17	14.17

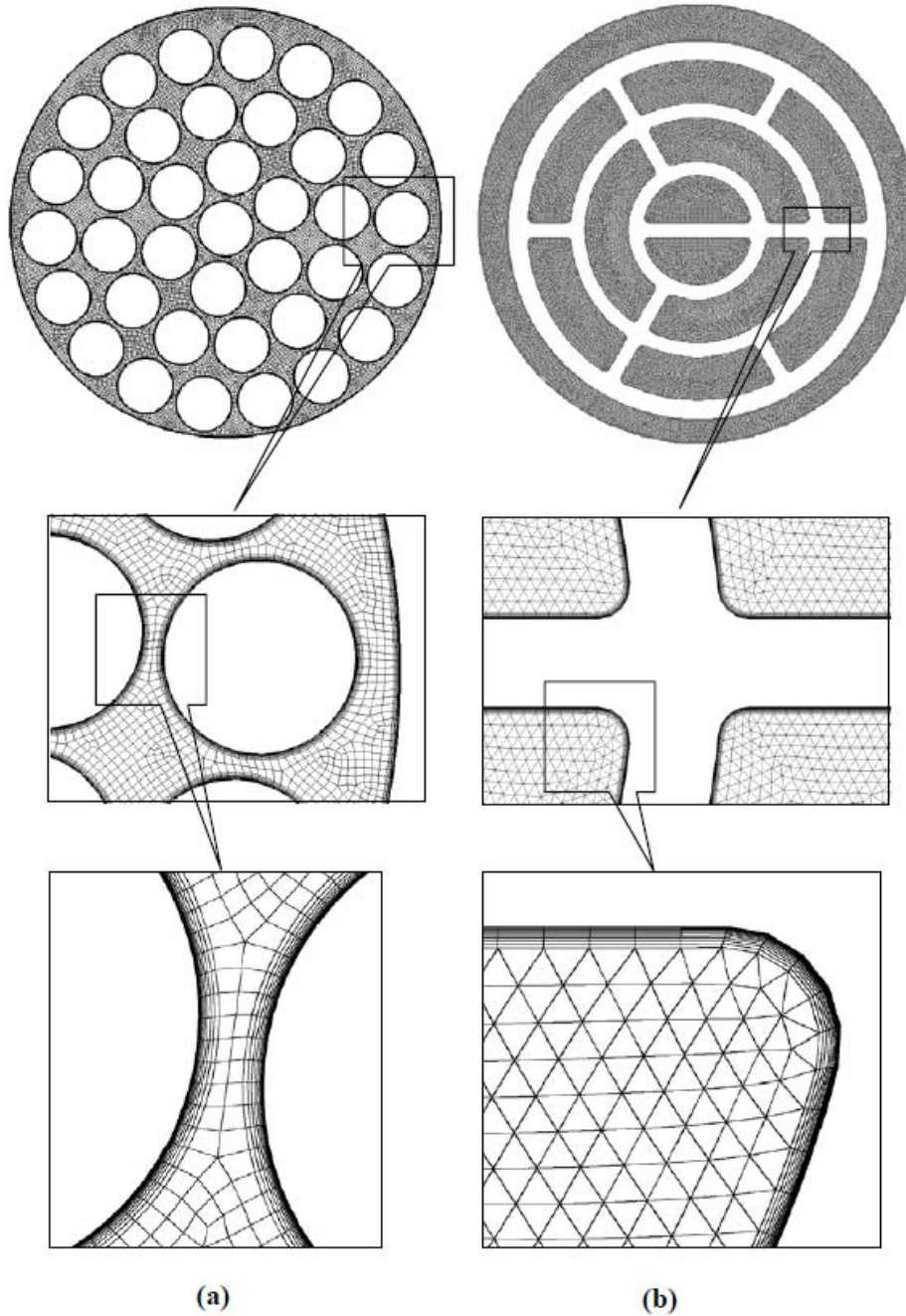


Fig. 2-7 Exploded view of meshes for the bundle (a), and endplate subchannels (b).

2.4.3 Domain Partitioning, Boundary Conditions

The present model domain is segregated into several regions to handle different geometries of the pipe section, the endplate subchannels and the bundle subchannels. Each transition zone consists of a different geometry and these different geometrical regions were

connected to each other by the interface surfaces. This allows a transition through non-conformal meshes.

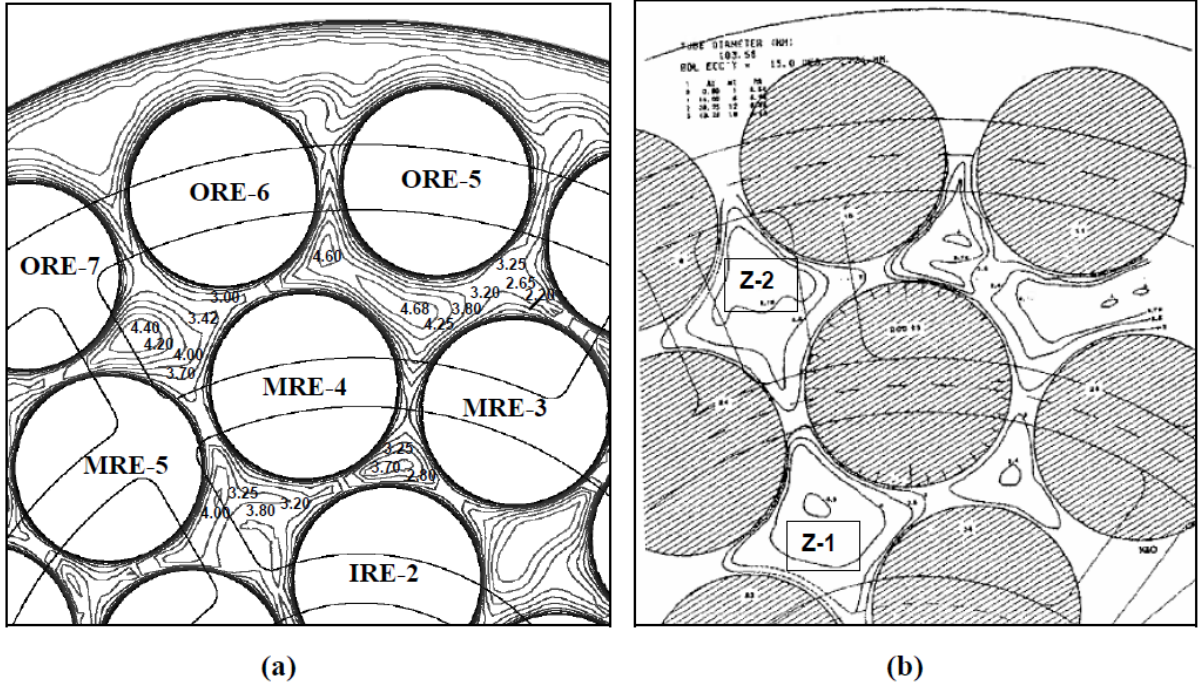
The inlet face is defined as the *velocity* inlet since the mean axial flow is known a priori at this cross-section. The outlet surface is specified as the *outflow*, which defines no z-gradient of flow parameters. This is in accordance to the actual situation since at the mid-span of the CANDU bundle fluid particle has almost minimal z-gradient (Zhang and Yu, 2011). The inner wall of the tube surrounding the bundle and the outer walls of all elements are defined as walls with the no-slip condition.

This is, however, worth mentioning here that modeling a half of the bundle and analyzing its behavior in isolation of the other neighboring bundles would not be fully correct for an ideal situation. Because, even at the middle of the bundle the fluid has influence from the interface zone having the other endplate which is not modeled. However, the idea of this half bundle model is to verify the extent of ability of the CFD model to predict the flow features. This will be carried out by comparing the results with that of experimental work from literature.

2.5 Validation of the results

The results of this half bundle CFD model are compared with the measurement done by D'Arcy and Schenk (1987). The local axial flow velocity contours around the element MRE-4 from the present study is checked with the measurement done by them, where the Reynolds number of the flow was kept as 25,000, based on the average bundle hydraulic diameter of 7.48 mm, with water considered as the fluid. In accordance with this Reynolds number of 25,000, the mean bundle flow is coming out to be 3.34 m/s corresponding to a mean flow velocity of 1.34 m/s at the inlet in the present CFD domain. Hence, solution is sought for the mean flow velocity of 1.34 m/s at the inlet for a separate CFD model. The local axial flow velocity around the MRE-4 at a cross-section 0.93 m from the upstream endplate is compared for both cases, as shown in Fig. 2-8. For better clarity and understanding, the values of contour lines at two different subchannel zones (Z-1 and Z-2) from simulation and from experiment are tabulated separately. From this figure, it can be noticed that the values in both contours are in good agreement with exceptions at few

locations. As expected, the center of each subchannel has highest axial flow velocity with gradually decreasing magnitude towards the fuel element walls. Based on this comparison, it would be fair to mention that present computational model, although only for a half of the bundle length, demonstrates reasonably agreeable results. Some of the results are presented in the following section.



Zones -->		at Z-1		at Z-2	
	Contour lines	Simulation (a)	Experiment (b)	Simulation (a)	Experiment (b)
1	Central line	4	4.5	4.4	3.75
2	1st line	3.8	4	4	3.5
3	2nd line	3.25	3.5	3.42	3
4	3rd line	3	3	3	--

Fig. 2-8 Comparison of axial velocity contours around a middle-ring-element for the present simulation, as shown in (a), with the measurement performed by D’Arcy and Schenk (1987), as shown in (b).

2.6 Results

Results on the z -velocity and corresponding pathlines are shown in the coming sub-sections.

2.6.1 Results of z -velocity

Fig. 2-9 shows the distribution of the z -velocity magnitude normalized by the mean axial flow velocity at different axial distances at a certain point of time. It is important to mention here that, although flow contours vary with time considering the unsteady nature of the flow, the pattern of the distribution remains similar with time. For the endplate midplane, subchannel areas show higher velocity zones at one side of the endplate ribs, except for the central rib. These subchannels adjacent to the endplate ribs have a differential pressure distribution on both sides of each rib because one side has a larger area than the other one, causing fluid to take the larger area subchannel path. For the $1D_h$ axial location contours, some areas are found with the velocity in the reverse direction.

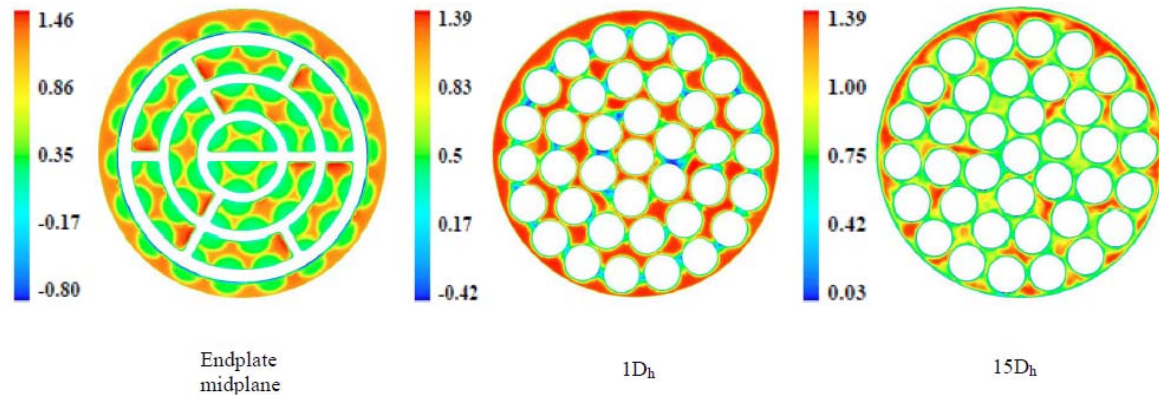


Fig. 2-9 Contours of z -velocity normalized by corresponding U of 2.4 m/s for different axial locations at U of 2.4 m/s.

A detail view will reveal that all the subchannel regions have positive velocity, whereas, the regions representing area merely after the endplate rings have either negative velocity or very low positive velocity. This is an important observation as it reflects the influence of endplate components. The presence of endplate makes the flow at the entrance region cross-flow-like and can be explained with the help of a wake phenomenon dominating in this region. As the result of the wake and vortex shedding just after the endplate rings (i.e., at the

downstream side of the endplate), fluid particles can rotate back towards the upstream side. The contour at the axial location of $15D_h$ further downstream does not show the reversal of flow, which is understandable, but some periodic distribution of flow, with a periodicity of 120° in the azimuthal direction, can be observed.

From Fig. 2-10, it can be noticed that fluid particles shift from its original flow path to a different one; but, the flow is showing a pattern that near the half way of the bundle it reflects lesser movement in the transverse direction.

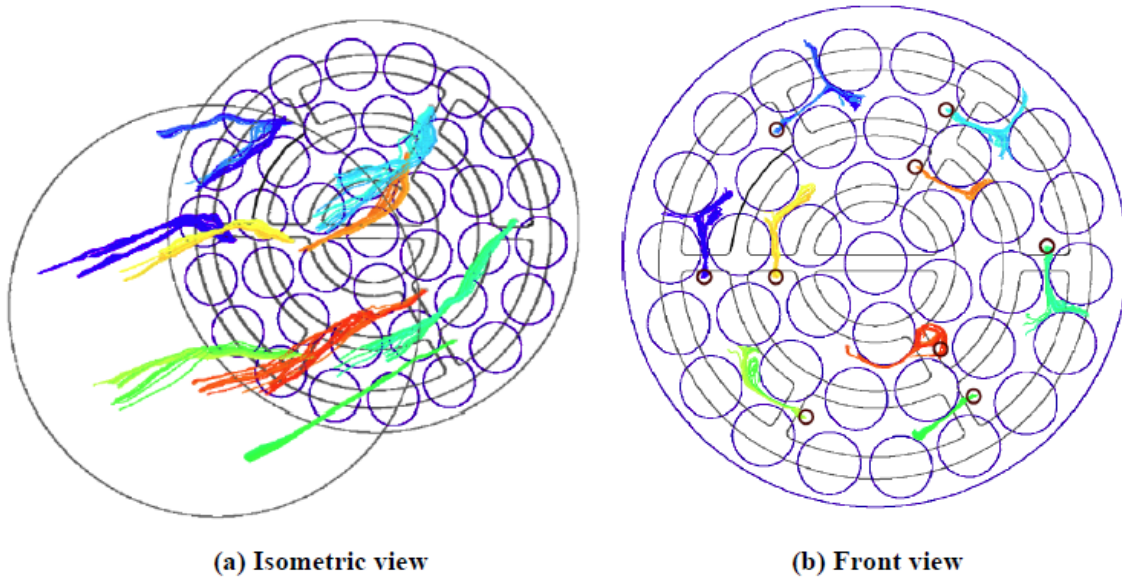


Fig. 2-10 Pathlines showing development of fluid flow with sources encircled when viewed from downstream side.

2.6.2 Flow development after endplate

Typical flow development with time is shown by Fig. 2-11 by a series of images. Pathlines are shown by lines varying from darker to lighter for four source surfaces to locations away from the four sources, respectively. These pathlines are generated from four different tiny surfaces at pre-selected locations. Two surfaces are on the left side and the other two are on the right side, as shown by each image. Surfaces created on the left side are at centre of the subchannels and represent a wide-gap region; whereas, surfaces created on the right side are between two elements and represent a narrow-gap region. To have a clearer view for better

understanding, elements are not shown for row (a) and only a few elements are shown for row (b) and row (c). The three columns represent three different instants of time.

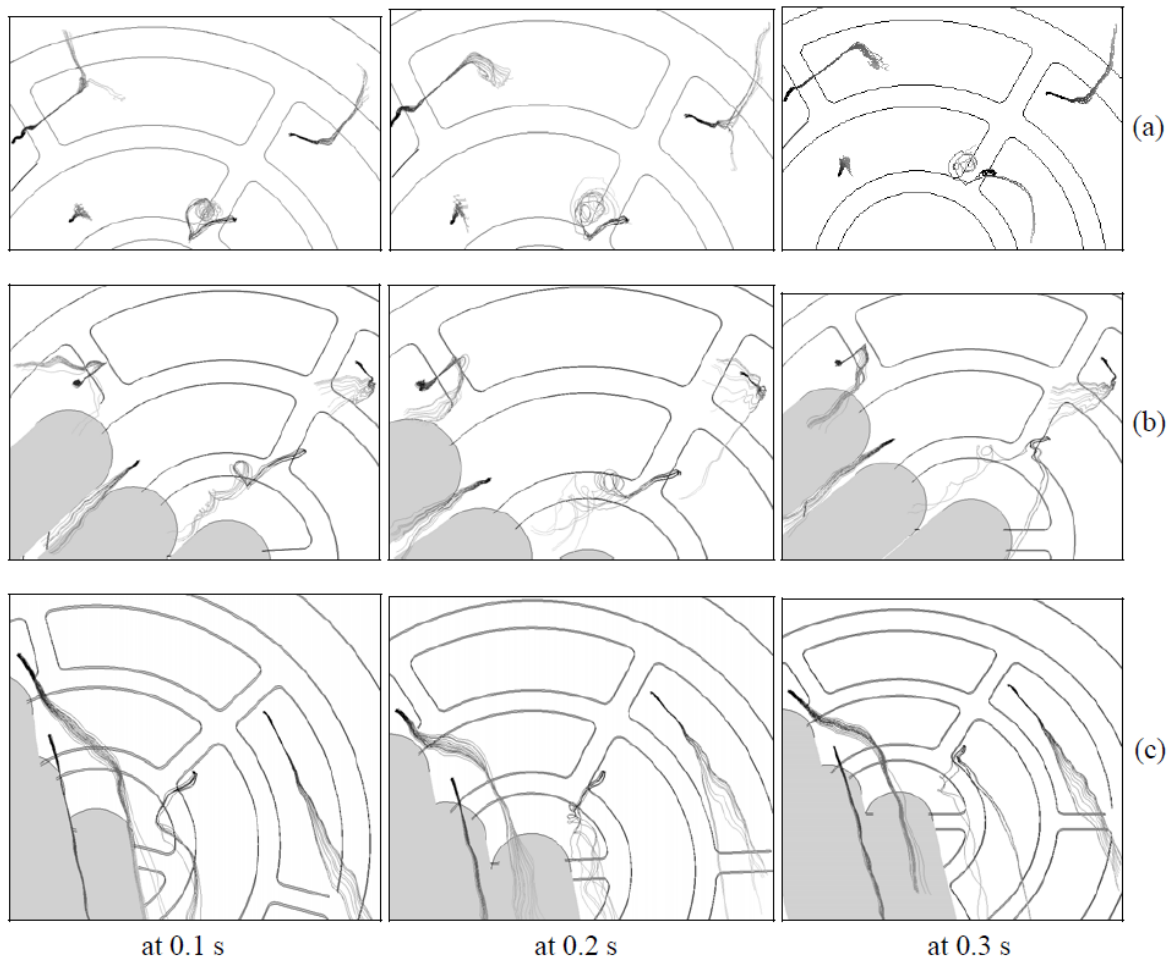


Fig. 2-11 Pathline showing development of flow at different time instants for U of 2.4 m/s, (a) viewed straight from outlet side, (b) and (c) viewed from different angles.

The flow coming from the four different sources deviates from the path corresponding to no-endplate situation, with different degrees. The source located at the bottom-left side exhibits minimum deviation; whereas, both top-left and top-right sources exhibit maximum deviations. Also, the variation of flow is small with respect to time, showing that the basic nature of the flow is almost similar. This can be noticed comparing flow images in different columns, even from the isometric views in (b) and (c).

A very interesting phenomenon is noticed for the source at the bottom-right location. Flow coming from this source area shows strong swirling motion in its path although the deviation is small. This observation can be verified in the isometric images where this effect is seen to be very prominent.

Another important observation is that, for all images, flow coming from a source near the endplate rib similar to sources at the top-left, top-right and bottom-right, gets deviated much more than that coming through the clear subchannel area, similar to the source at the bottom-left. This confirms that the presence of the endplate ribs/rings influences the flow to behave like cross-flow around the entrance region and helps generate wakes. Ultimately, due to the combined effect of all these ribs/rings, the bundle experiences a swirling-like flow through subchannels, as seen in Fig. 2-10.

2.7 Summary

From both the one-sixth sector and full cross-section bundle model, it is observed that the computational scheme adopted is capable of predicting the flow features in bundle subchannels of various asymmetric geometries. One of the findings from this part of study is the occurrence of swirling flow inside the bundle. Results demonstrate that the flow in the vicinity of the inlet bundle is far from the commonly perceived parallel flow. On the contrary, it is a mix of cross and parallel flow, and the presence of endplate ribs and rings are the reason behind this. However, in order to judge the fluid behavior inside the fuel channel more precisely, modeling a comprehensive flow model considering all 12 bundles would be appropriate and this is investigated in the following chapter.

CHAPTER 3: FLOW SIMULATION FOR A 12- BUNDLE FUEL CHANNEL

3.1 Introduction

Modeling of flow in a complete fuel channel filled with a string of 12 bundles is a computationally demanding matter. Comprehensive computational fluid dynamics models for the 12-bundle string of 37-element CANDU-6 fuel bundles are developed and solved using LES. The CFD models can take different angular positions for any bundle and thereby broadening the scope of the model by allowing any possible angular misalignment between neighboring bundles.

The present work deals with an application of a previously validated LES scheme (Bhattacharya et al., 2012) with an aim to developing a CFD model for a complete string of 12 bundles and assesses the nature of the flow and flow-induced excitations onto different bundles inside the fuel channel. The reason for selecting the LES scheme used in this work and details associated with the scheme are already described in much detail in earlier chapters and therefore, not included here. However, for clarity, readers are advised to please refer to Chapter 2 for further details on the CFD modeling schemes and its solution techniques adopted in this study.

The CANDU fuel bundles are not axi-symmetric structures. The angular position of fuel bundle is not controlled during refueling. The fuel bundles can take on difference angular positions inside the fuel channel. In this study, to address the effect of the possible angular misalignments between different bundles on the flow characteristics inside a complete CANDU fuel channel with 12 bundles, three different CFD models are created: (a) one with all bundles fully aligned to each other, (b) one with misalignment existing at two different bundle interfaces, and (c) another with all misaligned interfaces. The focus of this study is to see the effect of the angular misalignments on the flow and flow-induced unsteady lateral forces on each bundle in the string.

3.2 Modeling details and Solution technique

3.2.1 Description of the flow domain

As mentioned earlier, three different CFD models are developed with the complete length of a CANDU-6 fuel channel containing string of 12 bundles. The first model has all fuel bundles perfectly aligned to each other inside the pressure tube, as illustrated for Model-1 of Fig. 3-1. This model will help one understand the basic flow nature inside a fuel channel, if there is no misalignment in the interfaces, which is, however, a situation very hard to guarantee practically. In the second model, a partial implementation of the interface misalignment is done. The reason it is partial is due to the fact that this model has interface misalignment at only two different interfaces. The first and last four bundles are fully aligned to each other. But, the remaining set of four bundles, placed in between, are altogether misaligned by an angle of 45° . Within these centrally located four bundles there is no misalignment among themselves (Model-2 of Fig. 3-1). It would be noted here that the selection of this misalignment angle is random. This model will help capture flow properties if there is fewer misaligned interfaces, like between BD-4 & BD-5 and between BD-8 & BD-9 in Model-2 of Fig. 3-1. The third model comprises of all misaligned bundle interfaces (by 5° at each interface) in order to have an entirely opposite case to that described in the model-1 (refer to Model-3 of Fig. 3-1). Thus, with these three models, the nature of the flow and flow-induced unsteady forces onto the different bundles can be captured comprehensively. Please note that, the first bundle (BD-1) and the last bundle (BD-12) are always referred here with respect to the coolant's inlet and outlet flow direction, respectively (refer Fig. 3-1).

3.2.2 Solution scheme

For solving the computational problems mentioned in the previous section, the LES scheme, which is already tested and validated, is employed. The details for the LES scheme implemented in this study are not elucidated in this section and can be found in Chapter 2. The time step size in this study is chosen to be 5×10^{-5} s, which is well below the large eddy turn-over-time (LETOT) of 2.4×10^{-4} s. The mean axial flow velocities considered is 2.4 m/s at the inlet corresponding to an average velocity of 6 m/s through the bundle subchannels

and the corresponding Reynolds number is 4.86×10^4 . The temperature everywhere in the fluid (water) is assumed to be 300°C . A static pressure of 10 MPa is used at the inlet to simulate operating conditions similar to *in-situ*.

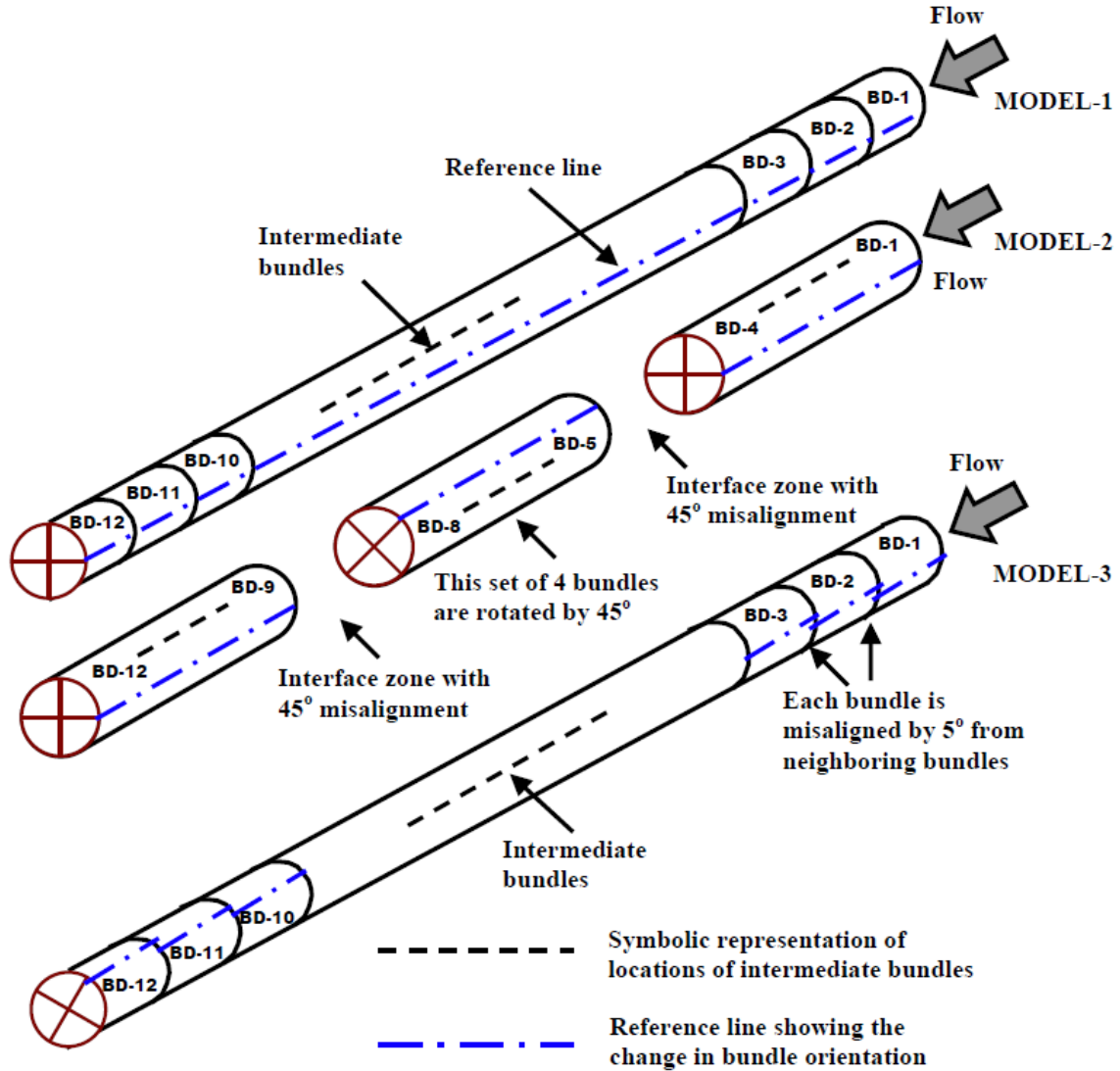


Fig. 3-1 Different models with interface misalignment and other details shown.

3.2.3 Computational resource

Each of the computational models has about 55 millions grid cells. Therefore, the enormity of such a large scale numerical problem requires very efficient, accurate and high performance computing resources. The numerical solution is obtained for the three

dimensional unsteady flow using a cluster of 60 high performance computer, in conjunction with a parallel processing scheme. The cluster consists of eight shared-memory machines that are high-end Sun SPARC Enterprise M9000 Servers. Each of these servers consists of 64 quad-core 2.52 GHz Sparc64 VII processors; also the servers have a total of 2 TB of memory (8 GB per core). A steady-state solution is first sought using the k- ϵ model. The converged steady-state solution is then used as the initial condition for obtaining a subsequent unsteady-state solution with LES. The transition time from steady state to unsteady state stable solution is about 2000 time steps or 0.1 s of flow time. The convergence criteria are set to a value of 0.001 for flow parameters. For the time step size used in this study, 2 to 11 iterations are required for each time step in the LES solutions to achieve the desired accuracy. This is to be noted here that even using such a high performance computer, it took about 130,000 CPU-hours (90 days approximately) to obtain for 0.4 seconds of real time simulation solution data.

3.3 Validation

The previously verified computational scheme, as described in Chapter 2, is extended to develop this 12 bundle flow model. To avoid redundancy, the details for this validation are not mentioned here and readers are requested to kindly refer to Chapter 2 for further insight.

3.4 Results

The present chapter will concentrate only on the flow features for different bundles along the whole length of the fuel channel considering various misalignment configurations. To demonstrate this, various flow parameters, like flow velocities, fluid excitation force, for each fuel bundle, are considered for analysis and discussion. It is observed from earlier studies (Zhang and Yu, 2011; Bhattacharya et al., 2012a), that the fluid excitations for bundle lateral motion primarily come from the region around the endplates, i.e., the inlet and the interface zones, where the flow is mainly mixed of cross and parallel flow, compared to the almost parallel flow at the mid-bundle locations. Thus, the analysis in the subsequent sections will be done for parameters in transverse, i.e., x and y direction, with z being the longitudinal or axial direction of the flow model. The next subsections present contours,

time histories, mean and RMS values for different parameters for different bundles to showcase the flow characteristics for the whole bundle string.

From the description of the three models, as depicted in section 3.2.1, it can be seen that Model-3 is entirely different from the other two models due to the fact that only in Model-3 all interfaces are with misaligned bundle orientations (Fig. 3-1). However, except for two specific interface locations, i.e., between BD-4 & 5 and BD-8 & 9, all interfaces of model 1 and 2 are with fully aligned bundle orientation. Therefore, from this aspect, it is assumed that results from Model-3 will have remote chance of similarity with other two models but, between model 1 and 2 similar results can be expected except for those two misaligned interfaces, as indicated above. Thus, a comparative study of flow parameters around these two interfaces would be a legitimate and logical approach in order to examine the effect of the angular misalignment on the bundle subchannel flow. This is worked out in the following sections.

3.4.1 Velocity contours at various interfaces

In Fig. 3-2, the contours of the velocity magnitude are presented for interface between BD-4 & 5. From this figure, the flow appears to be much regular, undisturbed and has a smooth velocity distribution in that cross-sectional plane in case of Model-1. Contrary to that, contours of Model-2 show much disturbed flow pattern both before and after the interface zone. Furthermore, in the close-vicinity of the interface of Model-2, the flow is suffering from additional obstruction and creating small scale wakes due to the presence of endplate ribs/rings of the downstream bundle appeared suddenly by the misalignment. Thus misaligned interface amplifies the transverse component of the velocity magnitude thereby enhancing the chance of lateral fluid excitations. Now, whether or not the lateral fluid forces indeed get amplified, and if so up to what extent, will be examined in the later part (section 3.4.4) of this chapter. Also, from Fig. 3-3, outcomes similar to the preceding paragraph can be observed. This signifies the effect of interface misalignment in influencing the bundle subchannel flow.

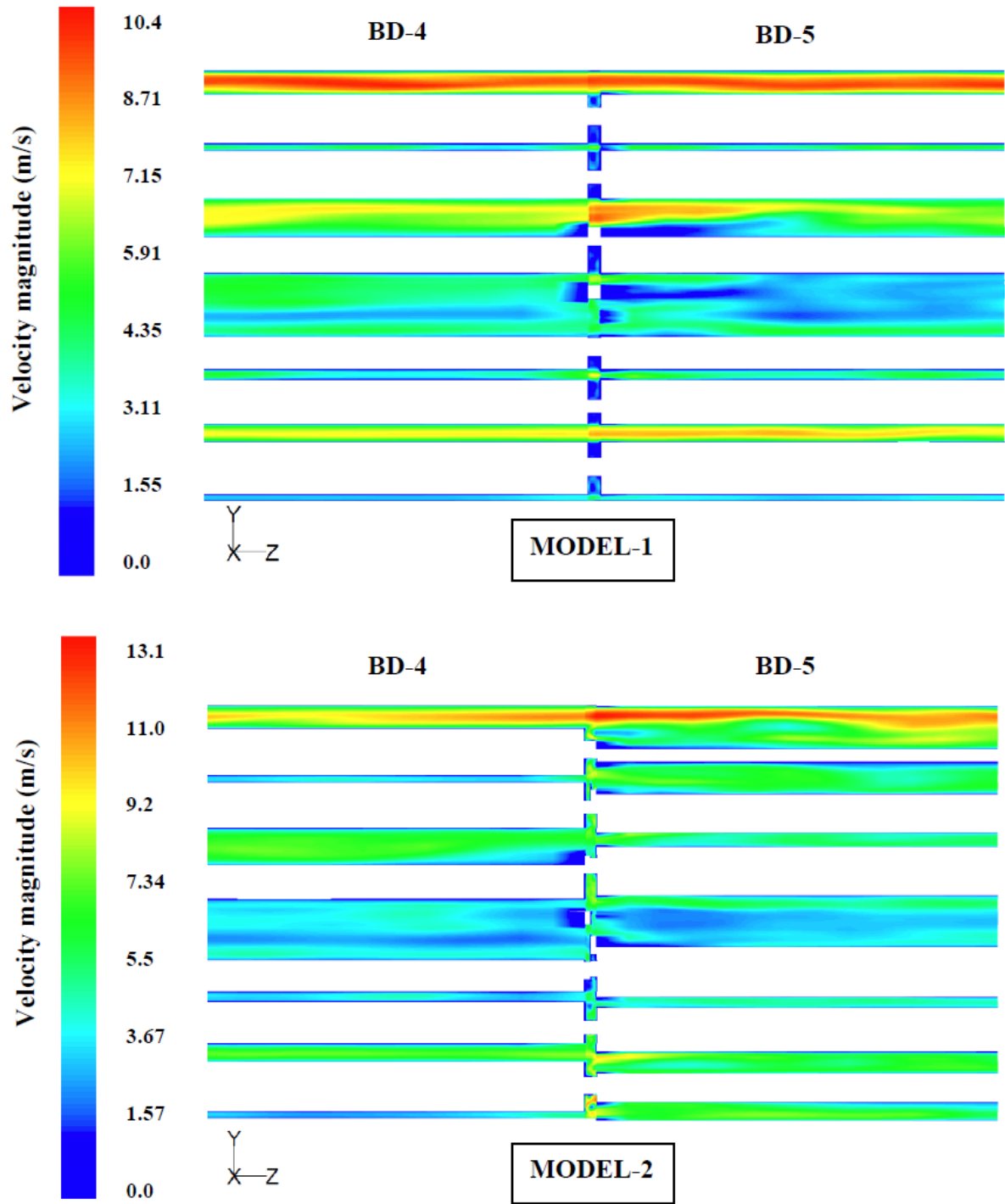


Fig. 3-2 Contours of velocity magnitude at the interface between BD-4 & 5.

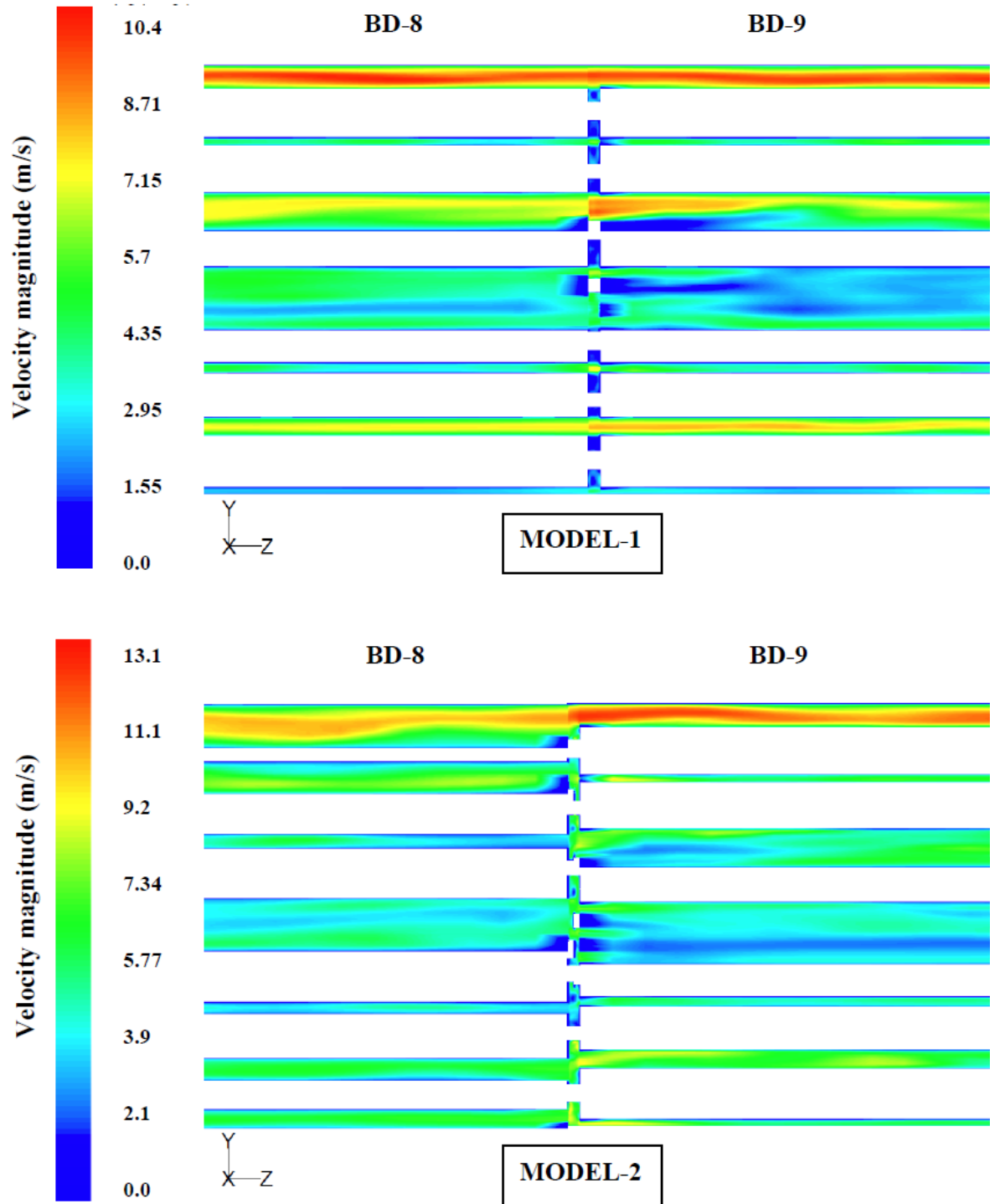


Fig. 3-3 Contours of velocity magnitude at the interface between BD-8 & 9.

3.4.2 Velocity vectors at various interfaces

First, in Fig. 3-4, radial velocity vectors are presented. It is very clearly noticeable that in both the cross sections, i.e., BD-4 & 8, radial components are not so significant in case of model-1 compared to that of Model-2, where presence of strong radial vectors is visible in various subchannels. Moreover, it should also be emphasized here that the occurrence of the strong radial vectors in the subchannels of the flow domain is localized to opposite sides of the vertical axis, towards left in case of BD-4 and towards right in case of BD-8. This can be explained in this way, that for the flowing fluid of BD-8, the BD-9 is rotated in the direction opposite to that of flowing fluid of BD-4 entering BD-5 (refer to Fig. 3-1).

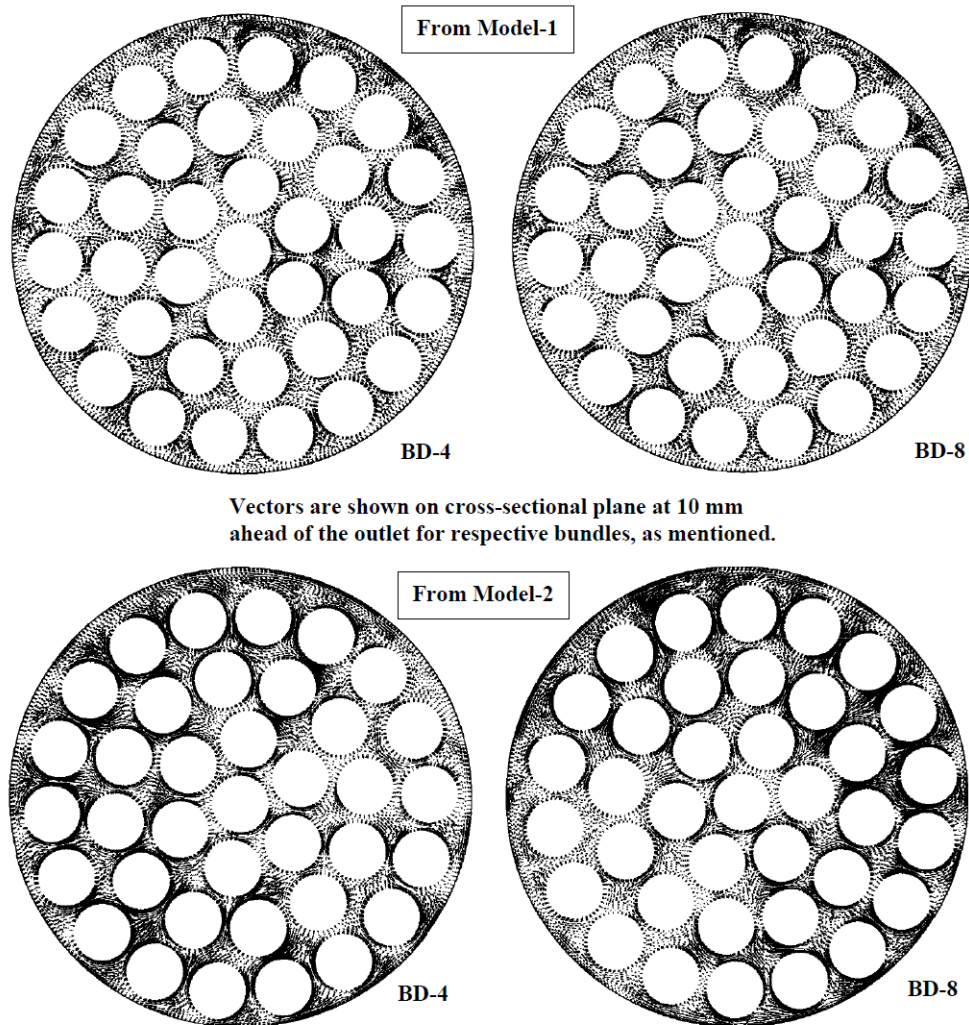


Fig. 3-4 In-plane radial velocity vectors (10x scale).

In order to see the vectors more clearly by their length and orientation, a zoom-in view is also produced for a portion in the upper half of the cross-section, as shown in Fig. 3-5. It is very clear from these vectors plots that the misaligned interfaces create considerably higher (from 0.7 m/s to 2.37 m/s in aligned and misaligned cases, respectively, i.e., almost 3 times higher for the maximum value) transverse flow motion across various subchannels. Therefore, going by this observation, BD-4 and BD-8 should be subjected to opposite transverse fluid excitations, which would be investigated in the section 3.4.4 of this chapter.

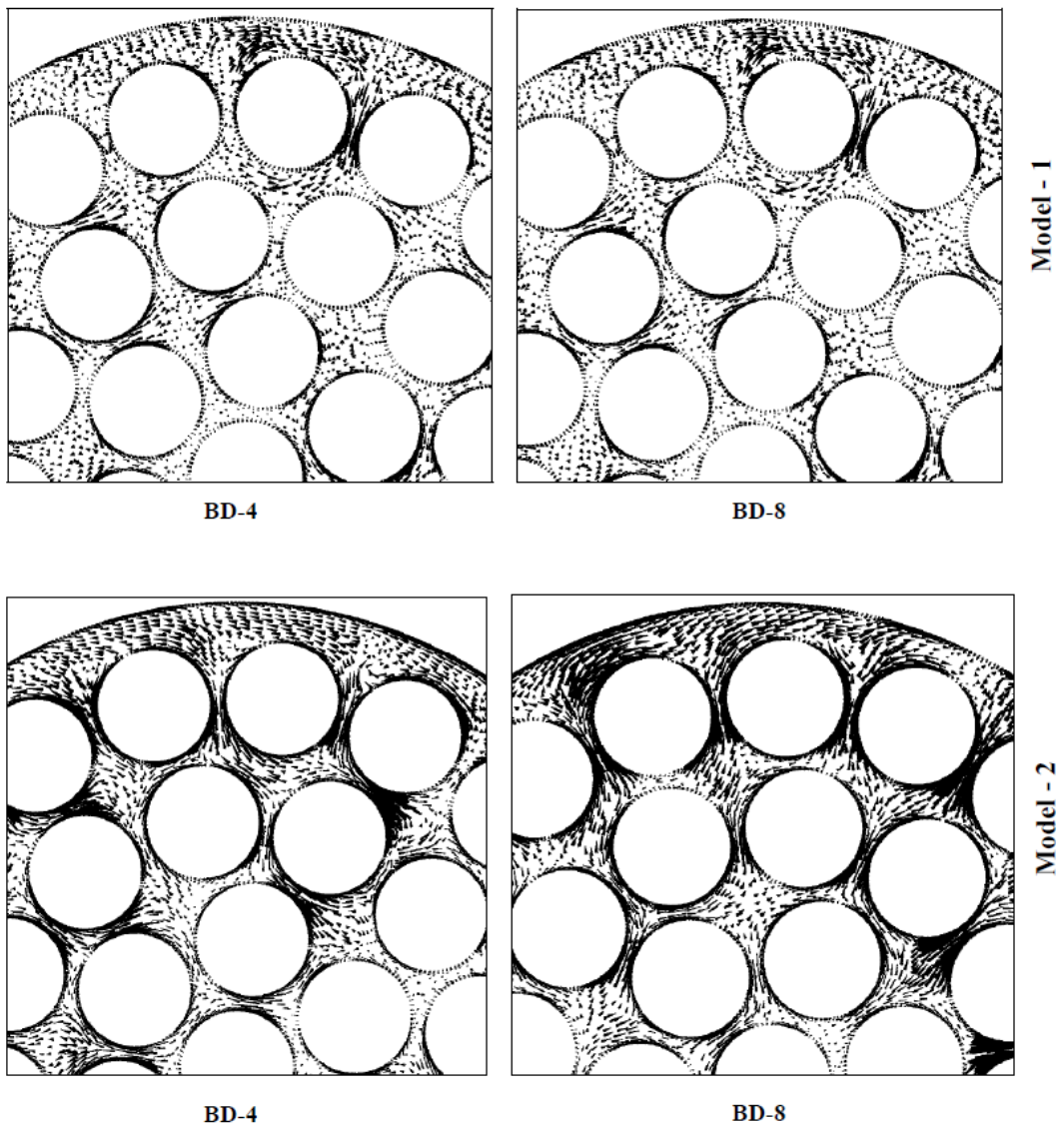


Fig. 3-5 Zoom-in view of in-plane radial velocity vectors.

The tangential velocity vectors, which may help the bundle roll inside the pressure tube, are shown in the Fig. 3-6. Here in this figure also, similar observations can be noticed like described in the preceding paragraph. Both the cross-sections for Model-1 show insignificant development of the tangential velocity vectors, unlike as observed in Model-2 where, their strong presence (from 0.5 m/s to 1.6 m/s in aligned and misaligned cases, respectively, i.e., almost 3 times higher for the maximum value) is noticed. Also, the locations where these strong tangential components are seen are distributed in the opposite direction of the vertical axis in BD-4 & 8, as expected. Like radial velocity, vectors are also shown in a zoom-in view for tangential velocity, as can be seen in Fig. 3-7.

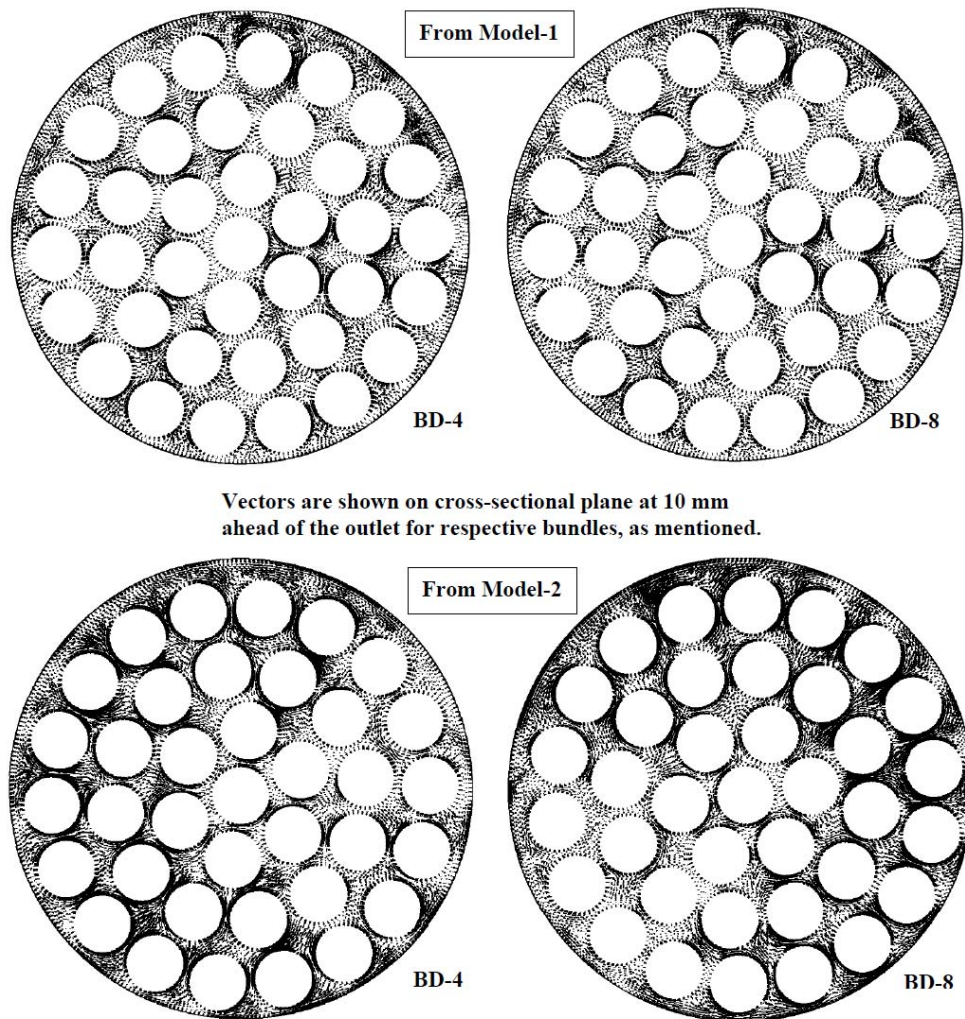


Fig. 3-6 In-plane tangential velocity vectors (10x scale).

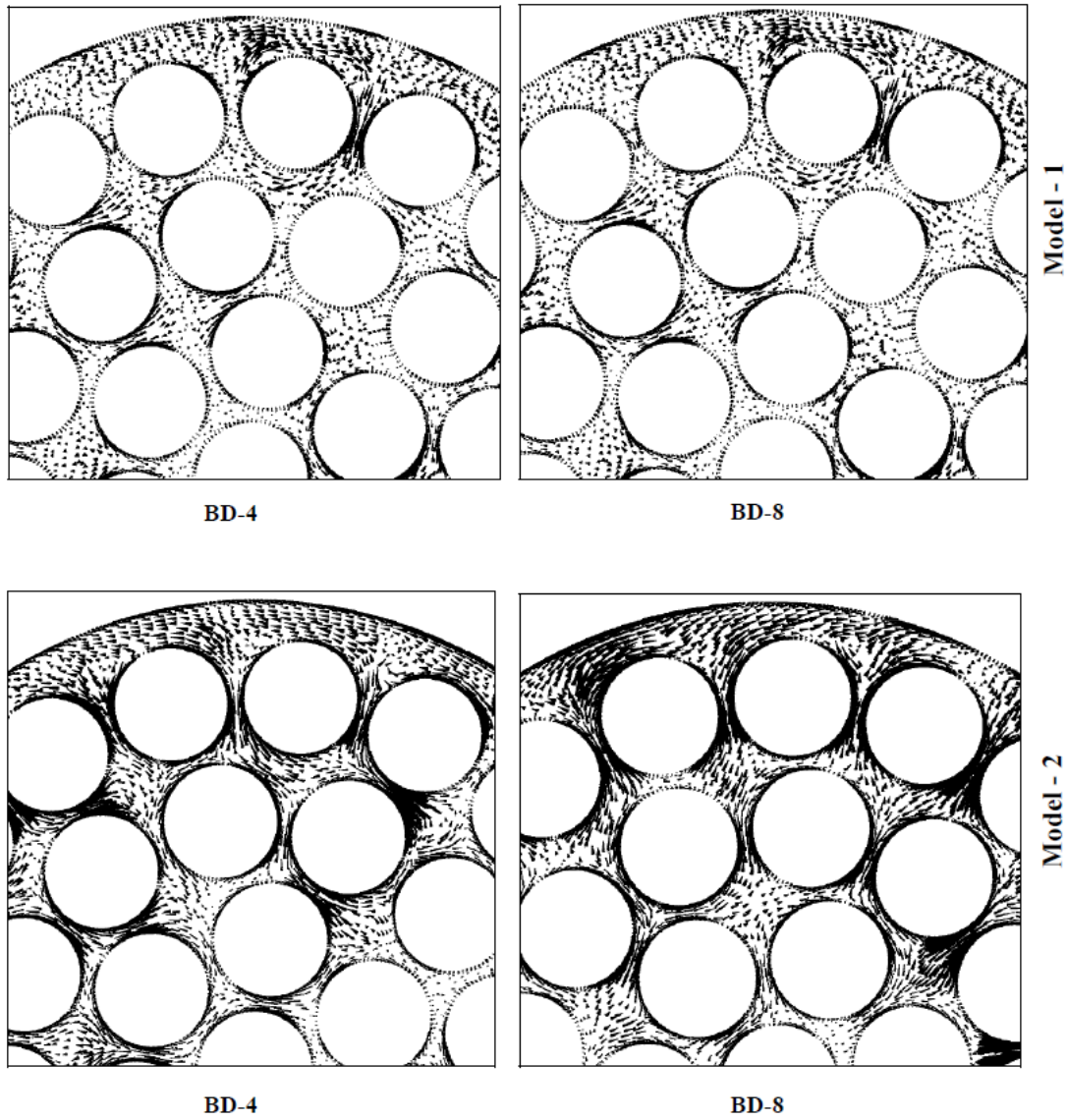


Fig. 3-7 Zoom-in view of in-plane tangential velocity vectors.

3.4.3 Time histories for x and y-force for different bundles

During the solution of the flow simulation, fluid forces in transverse directions are recorded at every time steps for each of the bundles. These force values are total fluid force acting on each bundle, but not on individual elements. The fluid force recorded can be expressed as,

$$F_i = \frac{1}{2} C_i \rho v^2 A \quad (7)$$

where, i represents the direction x or y , C is the coefficient of lift force, ρ is fluid density, v is fluid velocity and A is the reference area. Now, in FLUENT, first the coefficient of lift force in the respective direction is evaluated and then fluid forces acting on the solid faces are determined by integrating the pressure and viscous forces on the surfaces. Then the fluid forces acting on each cylindrical element and on the endplate are added up to finally evaluate the total force acting a single individual bundle. These all steps are repeated in each time-step to get the history of the fluid excitations over the total solution time. Comparisons are made between results of Model -1 and 2 leaving Model-3 for discussion in section 3.4.4. The following sub-sections are dedicated to analyze the results in detail. The color of time history for any particular bundle in Model-1 may differ from that of the corresponding bundle in Model-2; separate legends, however, are indicated in the results of two different models to avoid confusion in distinguishing the time histories of individual bundles.

3.4.4 Discussion on x -force (F_x)

The Fig. 3-8 shows the time histories of the x -force experienced by the different bundles. The results from Model-1 show almost insignificant amplitudes of fluid excitations in x -direction for all of the 12 bundles, compared to that of Model-2, where, the force amplitudes for several bundles are scattered in a wide range of ± 40 N. Not only that, a detail observation on the results of Model-2 will reveal that the fluid excitations and their fluctuations are larger for those bundles which are adjacent to the misaligned interfaces, i.e., BD-4 & 5 and BD-8 & 9. From the results of Model-2, it can also be seen that the level of fluctuations is higher for all other bundles as well, compared to Model-1 thus implicating the importance of consideration of angular misalignment in the flow model.

3.4.5 Discussion on y -force (F_y)

Not surprisingly, are found similar outcomes from the time histories of the lift force or the y -force of different bundles (Fig. 3-9). One can easily notice that the overall range of amplitude varies between ± 30 N and the large deviation from the mean is observed again for the BD-4, 5, 8 & 9, which are located around the misaligned interfaces. Also, like x -force,

the fluctuations of fluid excitation force in y -direction for remaining bundles, which are located away from misalignment zones, is also significantly influenced by the presence of interface zones and hence they too are amplified to a considerable amount.

This in turn hints that the presence of only two misaligned interfaces out of a total 11 of them can influence the lateral fluid excitations for all other bundles which are even away from the misaligned interface locations. Thus, the results presented here are an indication to the fact that bundle-to-bundle angular misalignment should not be ruled out for the true evaluation of the fluid forces experienced by the fuel bundles.

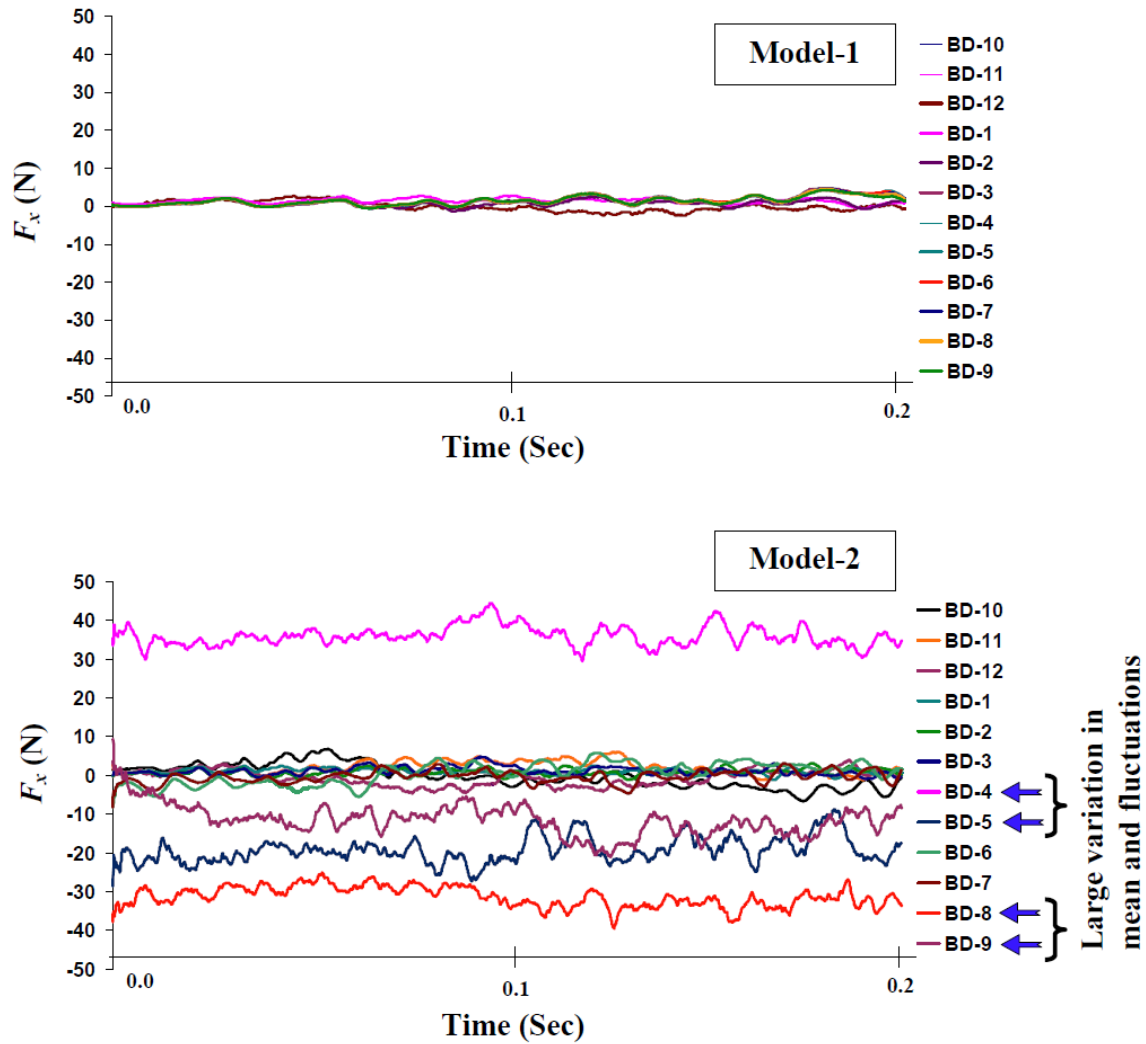


Fig. 3-8 Time histories of the x-force on different bundles.

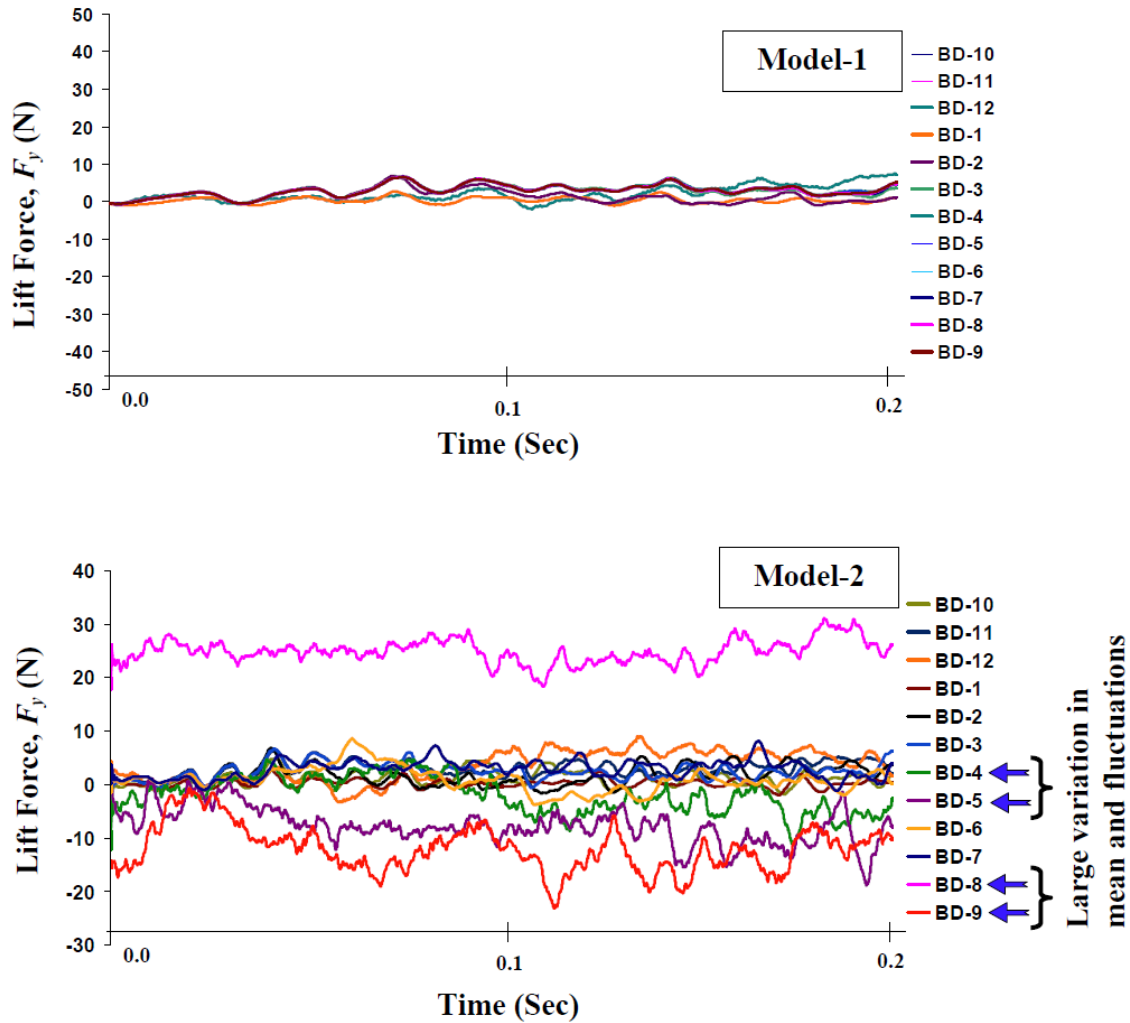


Fig. 3-9 Time histories of the y-force on different bundles.

3.4.6 PSDs for the x and y-forces in different bundles

Power spectral densities (PSDs) of the fluid forces in x and y directions are also evaluated for each fuel bundle for the recorded fluid force history data. The PSDs are determined and plotted using a Matlab script (See Appendix). Observations on the PSD plots are discussed in the next section.

3.4.7 PSDs of x -forces

The PSDs of the x -forces on different bundles are shown in Fig. 3-10. The results reveal that for Model-1, there is almost no shift in the evolution of these frequencies of the fluid lateral forces for different bundles. On the contrary, for both of the plots (b) and (c) i.e., for Model-2 and Model-3, it is observed that the fluid excitation frequencies evolve without showing any trend and keep on changing for different bundles. Moreover, from the very same plots, it can also be found that compared to fully aligned situation, misaligned bundle interface produces more number of sharp spikes in their respective spectra making the bundles subjected to more number of fluid excitation frequencies.

3.4.8 PSDs of y -forces

In Fig. 3-11, the PSDs of the y -forces for different bundles are illustrated for different model combinations. The observations in this figure are almost similar to that made in subsection 3.4.7. The Model-1 results show almost unchanged spectra for different bundles, whereas, in the case of the other two models, they have several spikes.

3.4.9 Mean and RMS values of x and y -force for different bundles

It is important to investigate the lateral fluid forces acting on each bundle in the complete length of the 12 bundle string inside the pressure tube. The RMS values of the recorded data are evaluated after deducting the mean from the original data and processed further with the help of Microsoft Excel tool.

3.4.10 Mean and RMS of x -forces

The mean values of the x -force of different bundles are shown in Fig. 3-12. The lowest values are coming from Model-1 wherein all bundles are placed at fully aligned configuration. But, for Model-2, maximum rise in the amplitude is seen for BD-4, 5 & 8, with 4 and 8 showing highest values but opposite in direction. This is quite in agreement with what is observed in and expected of earlier section 3.4.2. Further to this, one can also notice here, that between Model-1 and -2 except for BD-4, 5, 8 & 9, values corresponding to other bundles are almost matching with each other. This observation is indeed important simply because if there are fully aligned interfaces, lateral fluid excitations are not to be

amplified a lot and it is only around the misaligned interface zones where these forces become significantly large. From the same figure (Fig. 3-12), it is also seen that the mean value of the transverse fluid forces change to a reasonable extent if all the interfaces in the bundle string are with misaligned bundle configuration, as seen for Model-3.

While investigating the RMS values, it is found that the fluctuations are very small in case of Model-1, but is observed to be quite high for Model-2 and -3 both. For Model-2, BD-4, 5, 6, 8, 9 & 10 show considerable rise in the RMS values. This is because they contain the two misaligned interfaces; whereas, for BD-1, 2, 3, 7, 11 & 12, fluctuations remain comparable to that of Model-1. This is because these bundles are situated far from the misaligned interfaces which turned out to be one of the major sources of the lateral fluid forces. However, for Model-3, except BD-1, RMS values of all remaining bundles show large variations from that of model-1 and they keep changing from BD-2 to BD-12, which is as expected, because Model-3 has all bundles misaligned with each other.

3.4.11 Mean and RMS of y-forces

The mean and RMS values of the y-forces for different bundles are presented in Fig. 3-13. Like x-forces, here also almost similar observations can be made for Model-1. However, the mean values reach its peak at BD-5, 8 & 9 for Model-2. Interestingly, the values in BD-5 and BD-8 are reversed in this case from x-force. For Model-3 the values are again reasonably higher than Model-1 and varies from BD-1 to BD-12.

Like the x-force results, for the RMS values, for Model-1 no significant fluctuation is noticed; but, for Model-2, it is very high for BD-4, 5 & 9. This is again because of the fact that these bundles constitute the misaligned interface zones and thereby creating large amount lateral fluid forces acting on these bundles. Whereas, BD-1, 2, 3, 7, 9 & 10 exhibit fluctuating force almost matching with the corresponding bundle of Model-1; reason behind this is the location of these bundles being far away from the misaligned interfaces. The results from Model-3 are almost similar to that of the x-force results and hence proving the significance of the misaligned interfaces.

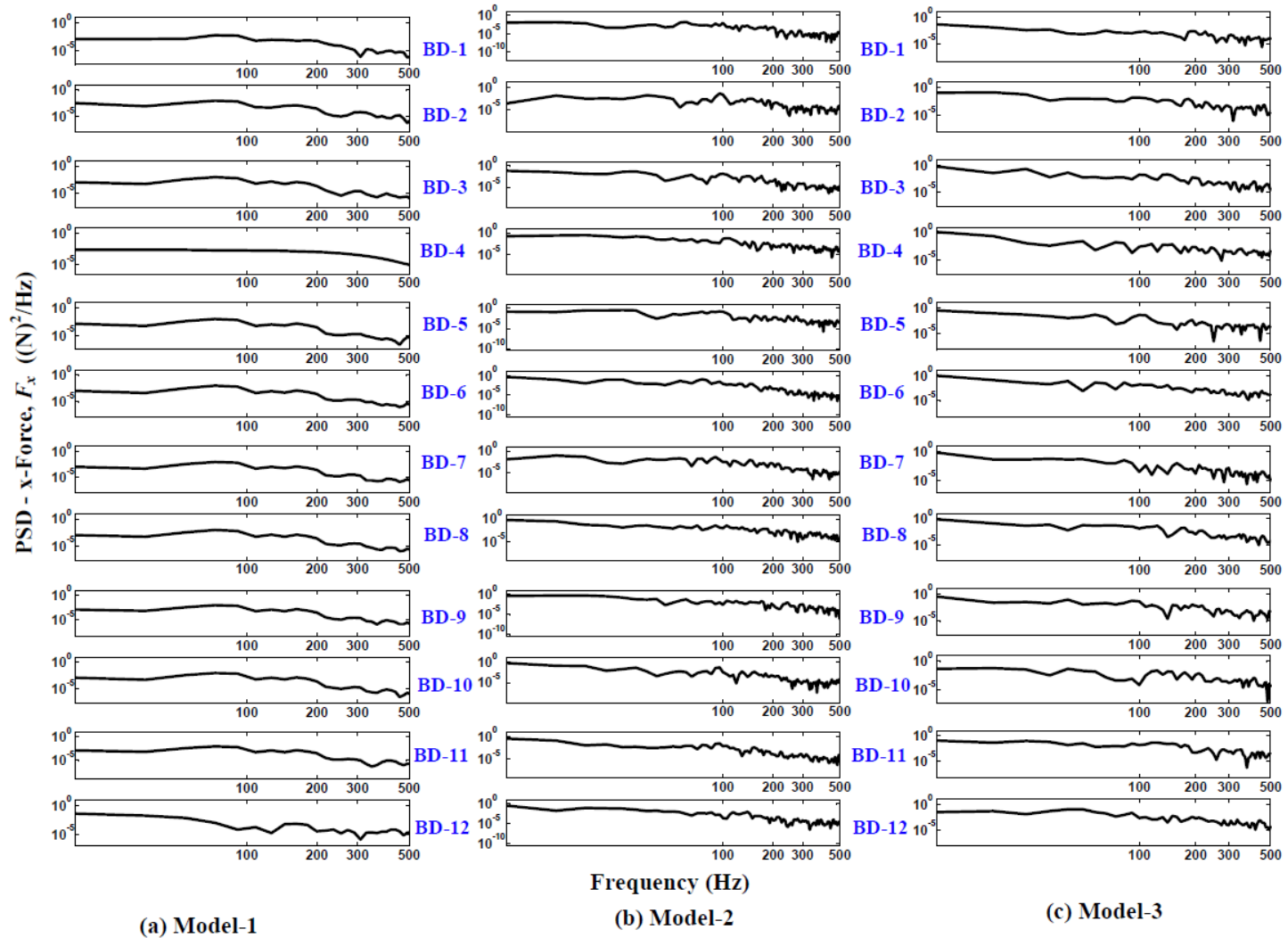


Fig. 3-10 PSD values of x-forces on different bundles.

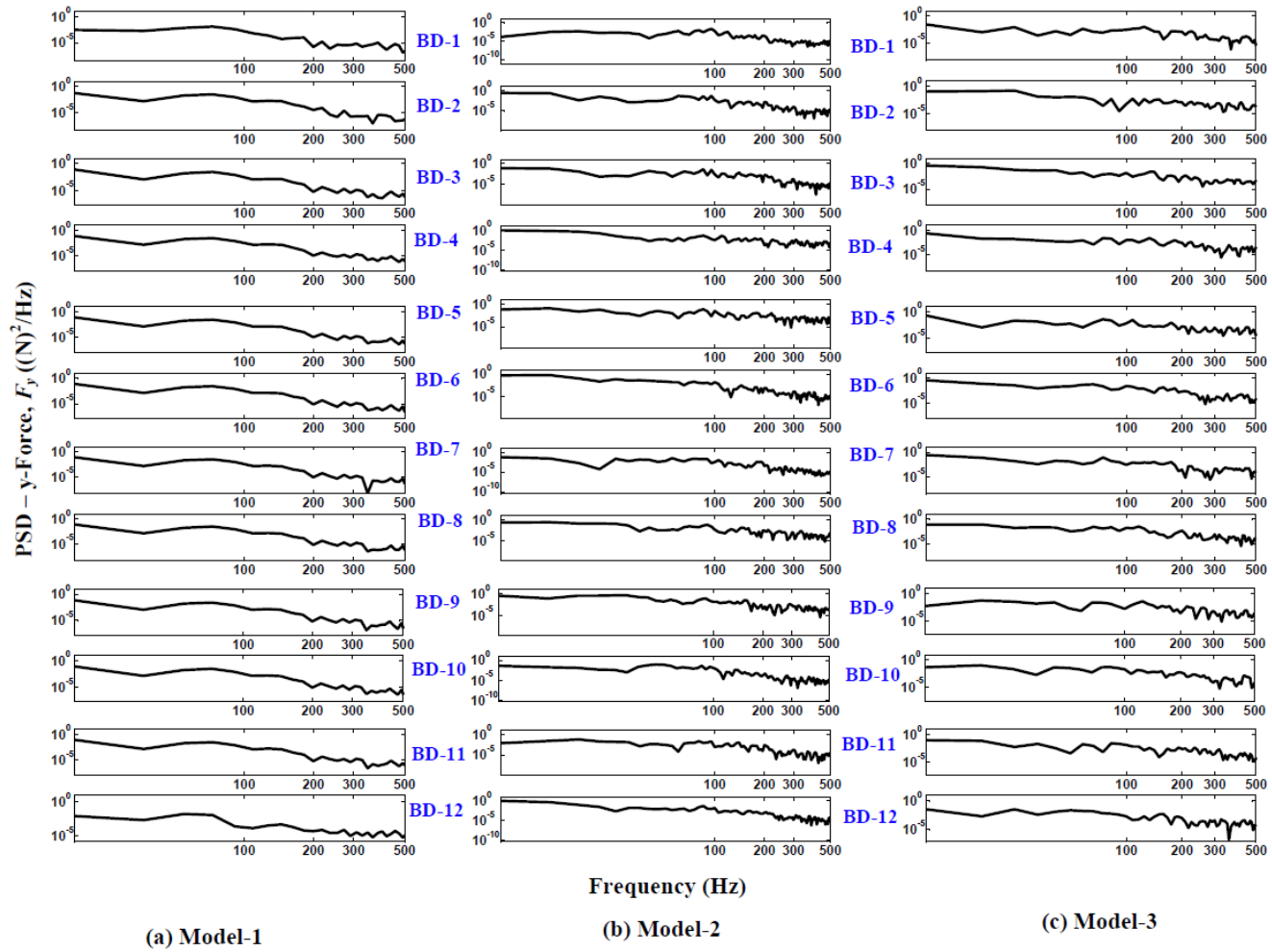


Fig. 3-11 PSD values of y-forces on different bundles.

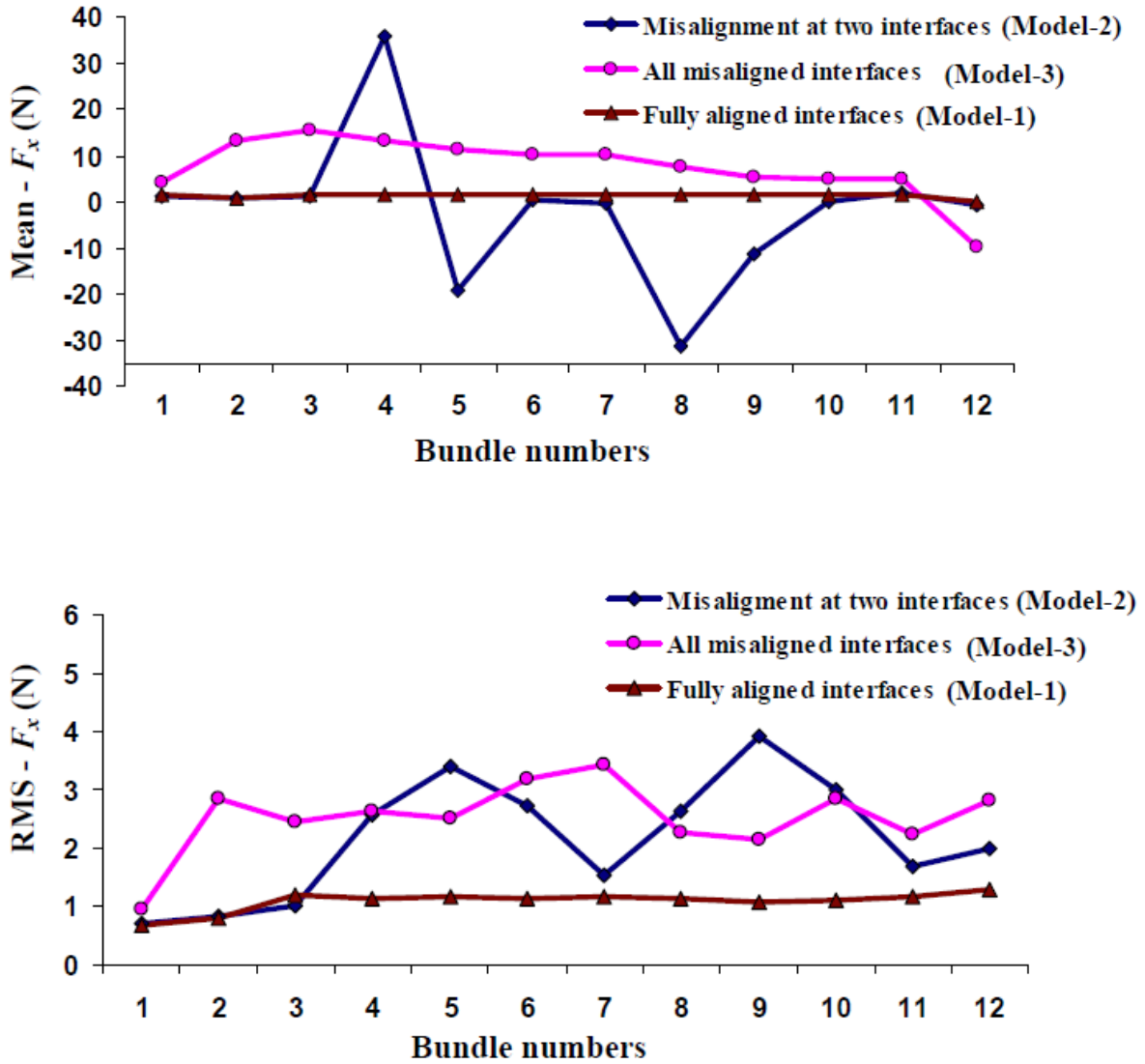


Fig. 3-12 Mean and RMS values of x-force on the different bundles.

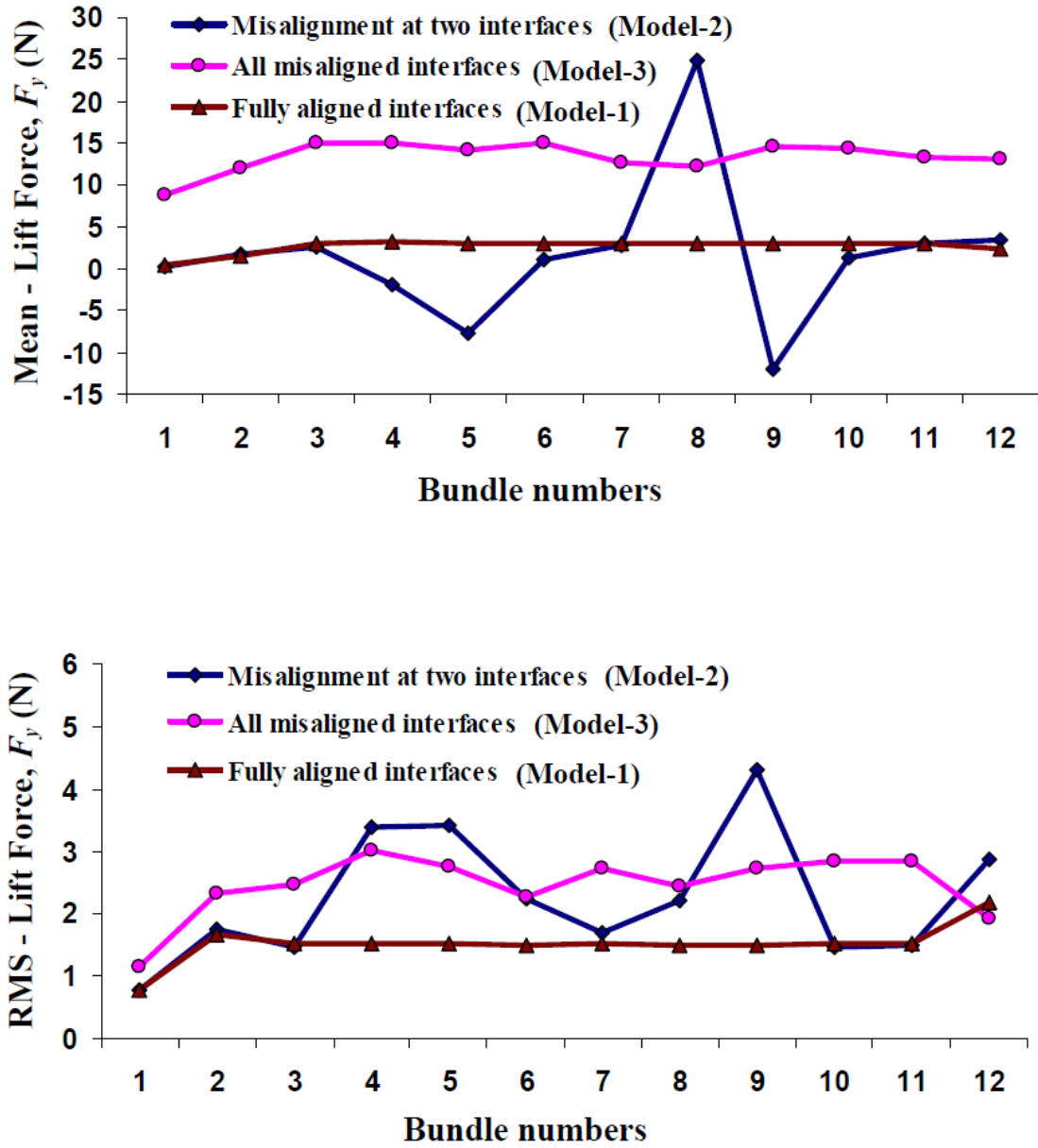


Fig. 3-13 Mean and RMS values of y-force on the different bundles.

3.4.12 Correlation study of flow features among different bundles

The fluid flow throughout the string of bundles is a continuous media as fluid particles are connected by the subchannels of bundles, however complicated they may be. Results from previous subsections showed that different bundle position could influence the flow features in the neighbouring bundles to a large extent; but how much the fluid properties, e.g., velocity, fluid excitation etc., are correlated to each other is not yet shown with cogent data or expression. Upcoming sections of this thesis will shed some light on this matter, with the help of correlation studies.

To examine the similarity (or dissimilarity) of flow among different bundles, a cross-correlation study is carried out on the time history of the flow parameters recorded during the simulation solution time. In time history analysis, the cross-correlation between two time series describes the normalized cross-covariance function. If, for the 12-bundle flow model, $(F_t)_i$ and $(F_t)_j$ represent two stationary flow properties corresponding to i^{th} and j^{th} bundle, respectively, then the cross-covariance of these pair of time histories would be as,

$$COV_{i,j} = E\left[\left((F_t)_i - \mu_i\right)\left((F_{t+\tau})_j - \mu_j\right)\right] \quad (8)$$

where, μ_i and μ_j are the mean values of $(F_t)_i$ and $(F_t)_j$, respectively, E is an operator which determines the expected values of the corresponding expression on which it is acting. Now, the cross-correlation coefficient, which is the normalized cross-covariance function, can be expressed as below,

$$C(\tau)_{i,j} = \frac{COV(\tau)_{i,j}}{\sigma_i \sigma_j} \quad (9)$$

where, σ_i and σ_j are the standard deviations of the two time histories $(F_t)_i$ and $(F_t)_j$, respectively, under consideration. From this relation, if $(F_t)_i = (F_t)_j$ for all t , then the cross-correlation coefficient represents simply the auto-correlation coefficient. The correlation coefficients are evaluated and plots generated using a Matlab script (See Appendix).

As far as the fuel bundle motion is concerned, it is also important to figure out the correlation or coherence of the flow features in the frequency domain, especially the fluid excitations. Revealing this would lead towards finding the possible matching of fluid excitation frequencies with the bundle frequencies, if there is any, which can be utilized for a larger scope of future study in the dynamics of the bundle behavior inside a fuel channel. This is executed again with the help of a Matlab script (See Appendix) for different flow parameters recorded during the simulation solution. The parameter plotted is the coherence magnitude with respect to frequency for two time histories using Welch's averaged and modified periodogram method (Welch, 1967). The Matlab script therefore estimates the coherence between $(F_t)_i$ and $(F_t)_j$ for the recorded period of time as a function of frequency, as expressed below,

$$C(f)_{i,j} = \frac{|P(f)_{i,j}|^2}{[P(f)_{i,i}][P(f)_{j,j}]} \quad (10)$$

where, $P(f)_{i,i}$, $P(f)_{j,j}$ are the power spectral densities of the above two time histories and the $P(f)_{i,j}$ is the cross-power spectral densities of those time histories. The $C(f)_{i,j}$ values determine how good $(F_t)_i$ is related to $(F_t)_j$ at each frequencies and provides a value from 0 to 1, with 1 being the highest coherence. Hence, the coherence values will always be 1 for all frequencies in case $(F_t)_i = (F_t)_j$. This is verified in the next section which deals with the results of the current study.

In a single fuel channel, altogether there are 12 bundles; thus the number of possible bundle-pair combinations could be: $({}^{12}\check{C}_2+12)$ equalling 78. Here, \check{C} denotes conventional notation of combination and the addition of 12 corresponds to 12 additional combinations of each bundle with themselves, i.e., the auto-correlations. Therefore, for any flow parameter there could be 78 total combinations among 12 bundles for which cross-correlation coefficient can be determined. Consolidating all of those hundreds of correlation plots in this manuscript is not plausible to demonstrate. Therefore, a strategy is developed aiming to cover the whole range of correlation combinations in order to deliver the objectives of this study, as elaborated in the next paragraph.

For any operating condition with 12 bundles, there will be 12 time series for any flow parameter. Selection of bundle-pair combination is done in such a way that correlation is performed for: (i) all bundles with the first bundle; (ii) a middle bundle with rest of bundles and (iii) neighboring bundles of each misaligned interface in Model-2. To examine how the flow features keep developing (or modifying) as the fluid particles flow through BD-1 to BD-12, correlation is also carried out for a set of progressively incremented combinations: BD-1 & BD-2, BD-2 & BD-3, BD-3 & BD-4, ..., BD-11 & BD-12. All these combinations, as shown in Fig. 3-14, collectively will be able to find out the relationship among different flow parameters for different bundles and also reveal how this inter-bundle flow relationship is influenced due to the presence of the bundle angular misalignment.

3.4.13 Correlation x-velocities and x-forces in time domain

First, the correlation coefficients are plotted for x-velocities for different bundle-pair combinations. These velocity parameters are recorded through out the solution time for every time steps for point location in a subchannel at 10 mm after the inlet endplate for each of the bundles. The location of the point is selected in such a way that similar points would be considered in corresponding location of the misaligned bundles as well. From Fig. 3-15 (a), correlation between BD-1 and other bundle can be seen. Except for $C(\tau)_{1,1}$ case, which is the auto-correlation with its own, no other bundle show good correlation with BD-1. This is justified since the BD-1 is the entry point for the flow in the fuel channel from a clear pipe flow regime to an entirely different bundle-endplate subchannel flow regime; the flow in BD-1 may not resemble very much with the rest of the bundles. The correlations of BD-6 with rest of the bundles are plotted in Fig. 3-15 (b) from which strongest correlation is seen between all bundles, except with first three bundles in the string, which shows that fluid particles take few bundles of distance to become a regularized bundle subchannel flow. In Fig. 3-15 (c), correlation plots are shown for specific bundle-pair combinations which include bundles constituting the misaligned interfaces and its neighboring bundles in case of Model-2. Results from these plots and corresponding similar plots from Model-2 will help compare the influence of the misalignment on the flow correlation.

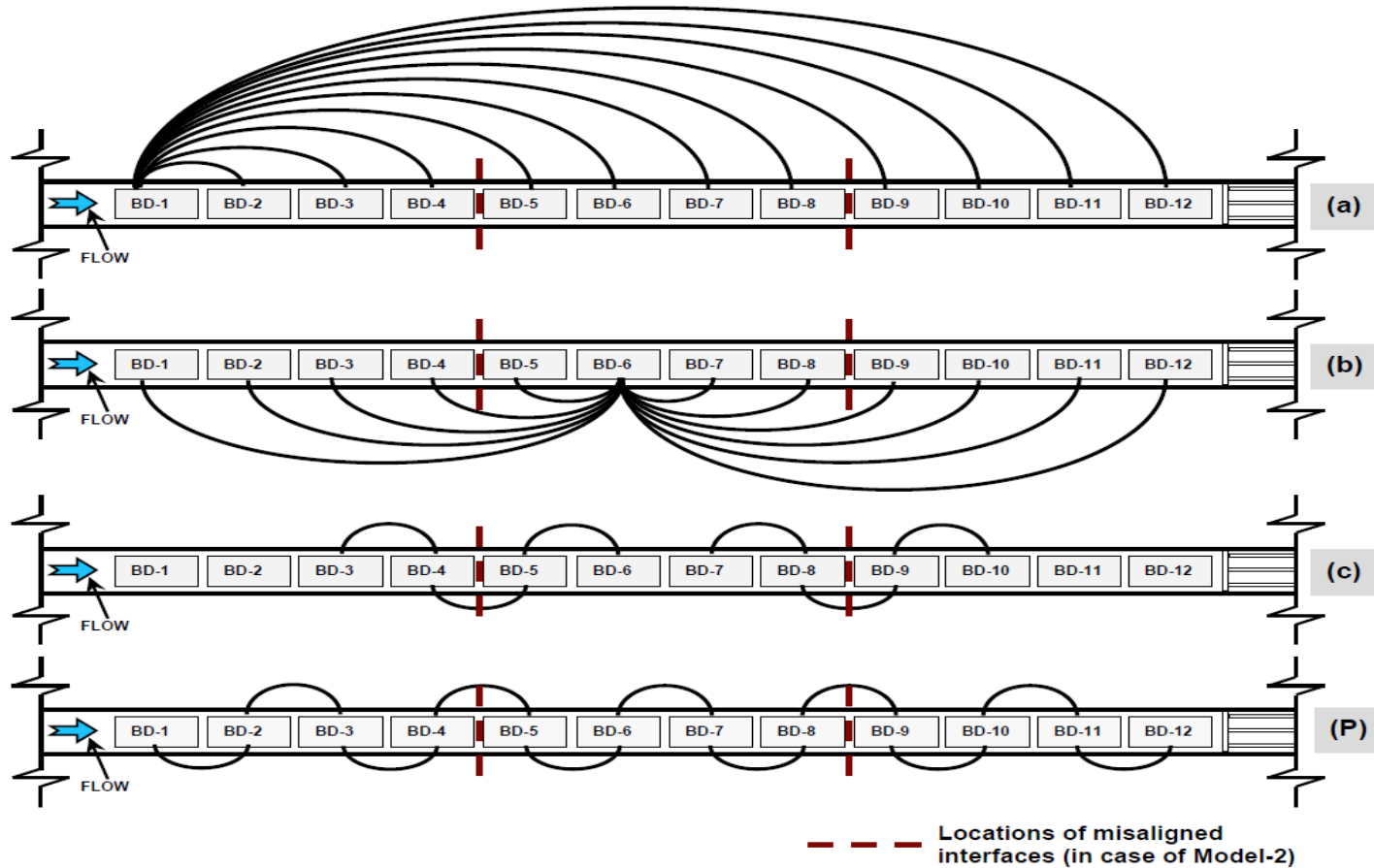


Fig. 3-14 Different bundle-pair combinations for correlation study: (a) BD-1 with BD-1 to BD-12; (b) BD-6 with BD-1 to BD-12; (C) BD-4 & BD-5, BD-4 & BD-3, BD-5 & BD-6, BD-8 & BD-9, BD-8 & BD-7, BD-9 & BD-10; (P) Progressively incremented combinations: BD-1 & BD-2, BD-2 & BD-3, BD-3 & BD-4, ..., BD-11 & BD-12.

It can be clearly noticed that a strong correlation is seen in all combinations of bundle pairs selected; this implies that flow properties of different bundles placed at the midway of the fuel channel are highly correlated for the completely aligned bundle arrangement.

If we see Fig. 3-16, which refers to Model-2, from (a) observation similar to Fig. 3-15 (a) can be noticed. A comparison between part (b) of both Fig. 3-15 and Fig. 3-16 reveals that strongest correlation occurs for $C(\tau)_{6,6}$ in Model-2, as expected. All other bundle-pair combinations exhibit almost no correlation or very weak correlation, as opposed to what is seen for Model-1. This can be explained as, the fluid flow features loose their resemblance from bundle to bundle due to the presence of misaligned interfaces. In Fig. 3-16 (c), it can be observed that a very weak correlation is present for these set of bundles unlike what is noticed in Fig. 3-15 (c). This is justified since misaligned interfaces change the pattern of the flow in the bundle subchannels and hence weaker correlation.

The correlation of bundle-pair in their progressive increment from BD-1 to BD-12 is shown in Fig. 3-17. From Fig. 3-17 (a), it is observed that except for first 3 to 4 bundles, all other combinations exhibits strong correlation meaning that flow nature is very much coherent in the most part of the bundle string barring few from the inlet end. The reason for this is explained above. As expected, the misaligned interfaces break the inter-bundle coherence of the flow parameter showing the weakest correlation values, as seen in Fig. 3-17 (b).

The change in the flow pattern in case of misaligned interfaces will obviously reflect onto the fluid forces acting on the bundles; this is examined here with combination “P”. Now, looking at Fig. 3-18 (a), it can be seen that the nature of the flow for the first three bundles at the inlet and the last couple of bundles at the outlet end is the most uncorrelated ones. Other than these, remaining all bundle-pairs possess a much strong coherent flow, as expected. From Fig. 3-18 (b), it is observed that the flow similarity observed in case Model-1 is lost in Model-2 emphasising the influence of the bundle angular misalignment.

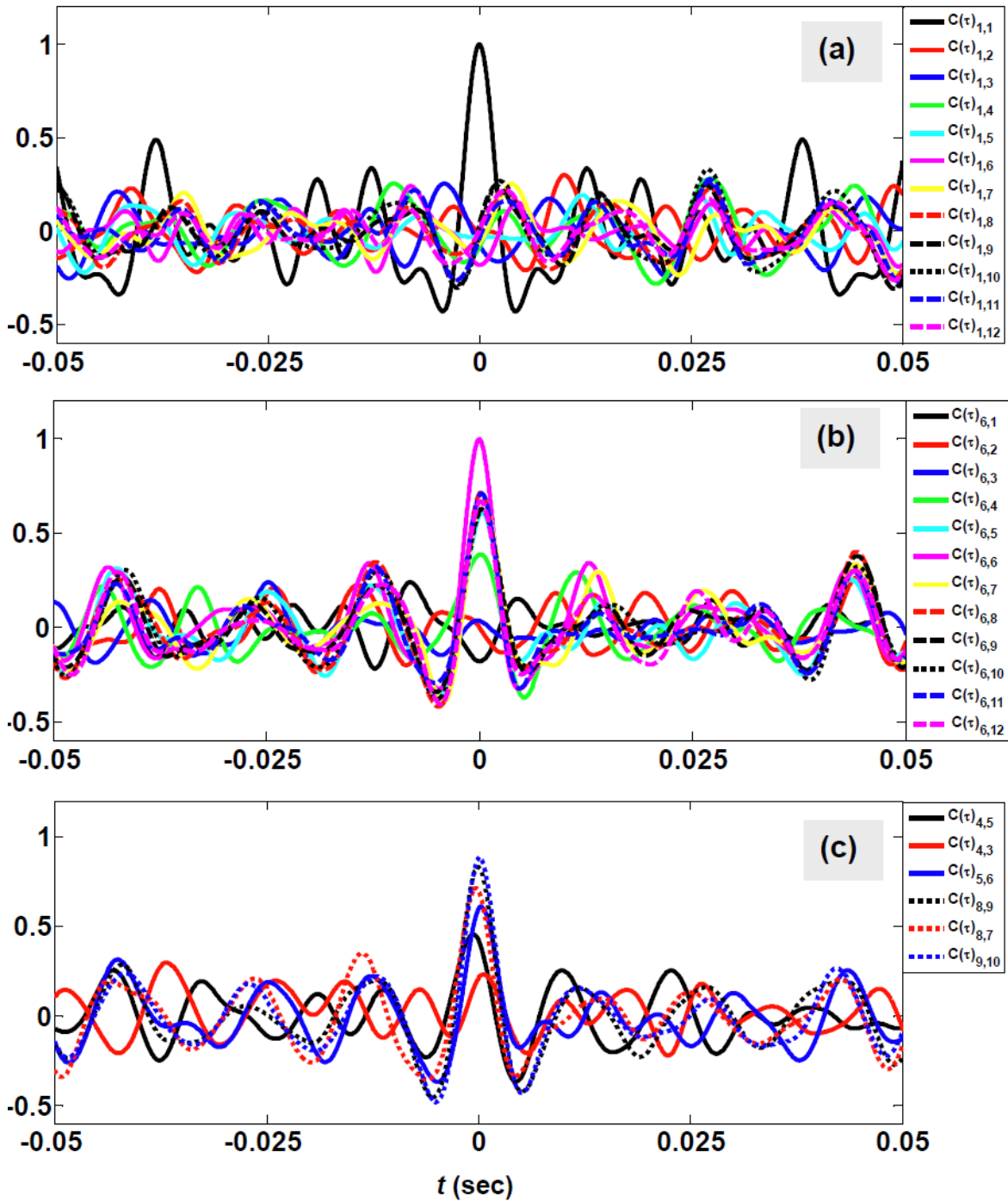


Fig. 3-15 Correlation plots of x-velocities from Model-1: (a) BD-1 with other bundles; (b) BD-6 with other bundles; (c) Bundles located near the misaligned interfaces in Model-2.

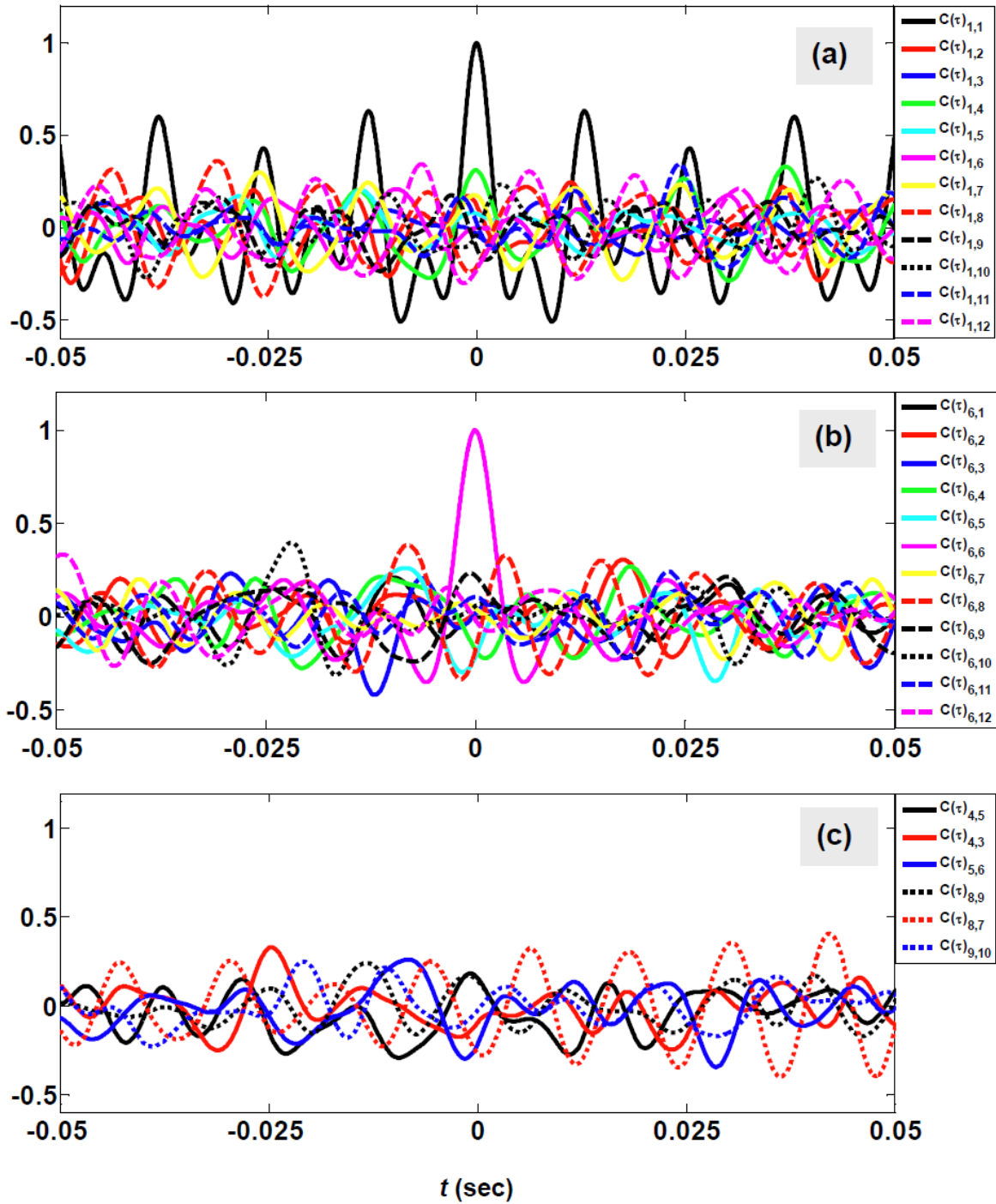


Fig. 3-16 Correlation plots of x-velocities from Model-2: (a) BD-1 with other bundles; (b) BD-6 with other bundles; (c) Bundles located near the misaligned interfaces.

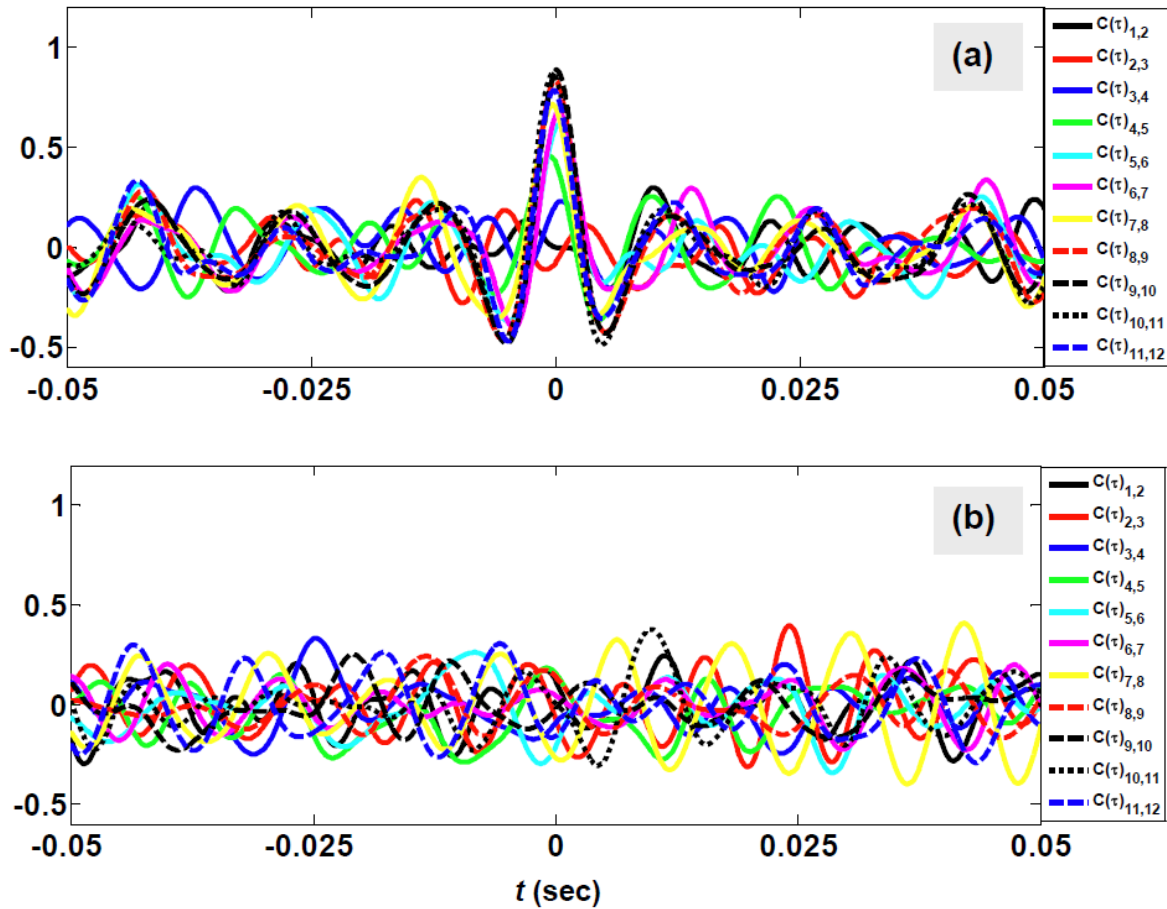


Fig. 3-17 Correlation plots of x-velocities for bundle-pair combination “P”: (a) from Model-1; (b) from Model-2.

3.4.14 Correlation x-velocities, x- and y-forces in frequency domain

Until now it is demonstrated that how much the fluid flow in one bundle is correlated to that of another bundle by selecting several bundle-pair combinations. They represent correlation in time domain only at different time lags, however, with a spatial comparison for different bundles since the bundles are placed at different axial locations inside the fuel channel. However, it is hard to conclude that that at which frequencies the flow parameters are

mostly correlated, but knowledge of those frequencies is of specific interest to the current study as far as fuel bundle vibration is concerned. This is discussed next.

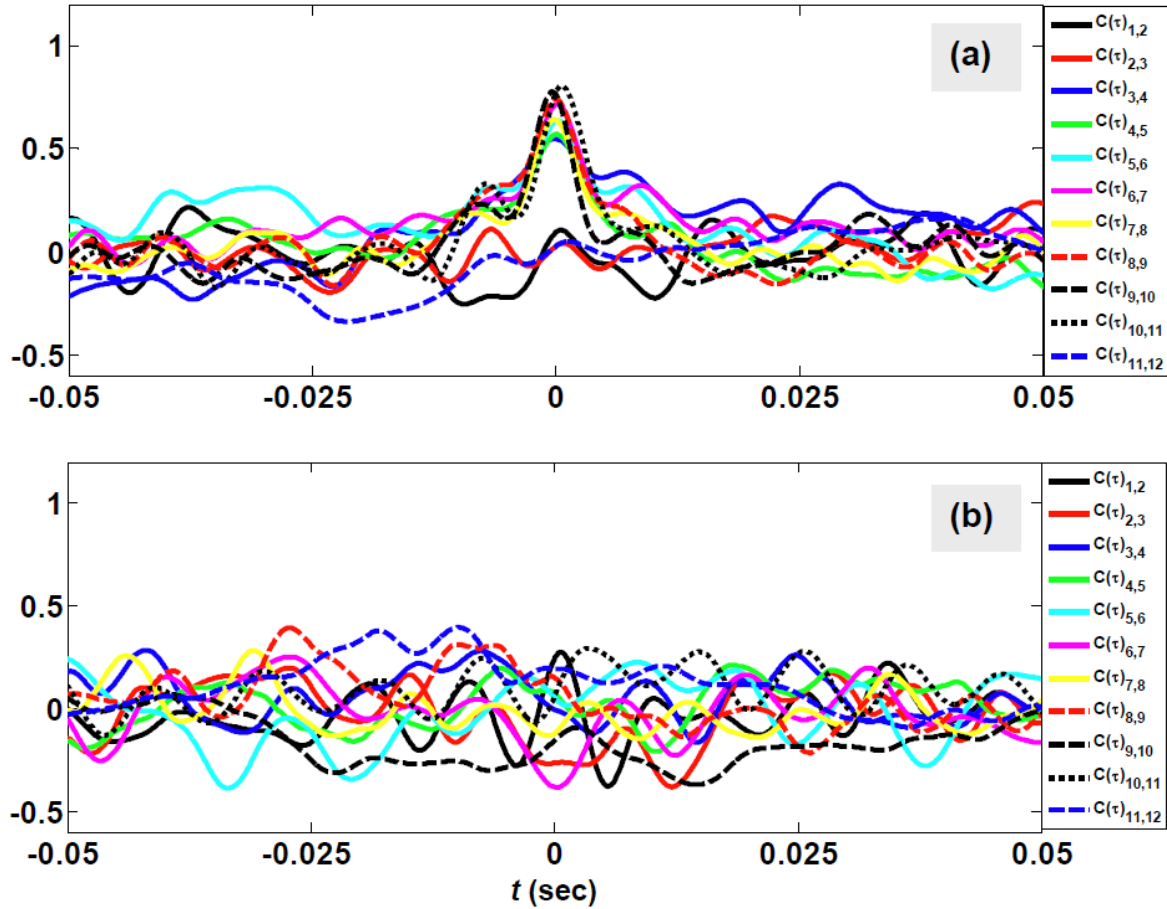


Fig. 3-18 Correlation plots of x-forces for bundle-pair combination "P": (a) from Model-1; (b) from Model-2.

From theory, the coherence will have a value of unity for all frequencies, only in case of auto-correlation i.e., when a time history pertaining to any bundle being compared with itself. This is exactly what is observed for $C(f)_{1,1}$ and $C(f)_{6,6}$ in Fig. 3-19 (a) and Fig. 3-19 (b), respectively. However, for all other bundle-pair combinations, the matching frequencies are very much scattered without showing any specific trend. The plots in Fig. 3-19 (b) are found with a coherence value of around 0.8, as opposed to Fig. 3-19 (a), for frequencies less

than 250 Hz. The part (c) of Fig. 3-19, where specific bundle-pair combinations are selected, demonstrates even higher coherence values, reaching almost unity for frequencies less than 250 Hz again and also at 280 Hz, 350 Hz for $C(f)_{9,10}$ combination. Therefore, in a string of fully aligned bundles, the bundles placed away from the ends of the string have more coherent flow with rest of the bundles and the coherence is more prominent in case of frequencies less than 250 Hz.

The coherence plots for Model-2 which considers misaligned bundles are shown in Fig. 3-20. The coherence is noticed to be very weak, mostly reduced to less than 0.5, for the whole range of the frequencies considered in both part (a) and (b) of Fig. 3-20 with exception in few cases. As expected, the combinations referring auto-correlation i.e., $C(f)_{1,1}$ and $C(f)_{6,6}$ for part (a) and (b), respectively, in Fig. 3-20 indicate a coherence value of unity for all frequencies. In part (c) of Fig. 3-20, a very weak correlation is observed for all the selected bundle-pair combinations. This implies that the presence of the misaligned bundle interface influence the flow in the frequency domain as well.

The flow coherence for combination “P” is shown in Fig. 3-21. It can be noticed from part (a) of this figure that a very strong correlation is present for all combinations of bundle-pairs chosen with an exception for first three consecutive bundle-pairs $C(f)_{1,2}$, $C(f)_{2,3}$, $C(f)_{3,4}$, which demonstrate the weakest correlation among all. Contrary to part (a), the part (b) of Fig. 3-21 exhibits very weak correlation, almost about 0.4. Therefore, it is found that the flow is strongly coherent among the intermediate bundles for fully aligned bundle arrangement, which, however, diminishes with the presence of the misaligned bundle interfaces.

The nature of lateral fluid excitations experienced by each of the bundles in the fuel channel and their correlation with that of other bundles is also important. The coherence plots for x - and y -forces are illustrated by Fig. 3-22 and Fig. 3-23. In Fig. 3-22, a comparison is made for the bundle-pair combination “P”. It is observed from part (a) of this figure that x -force values are well correlated, mostly up to a value of 0.7, for a large range of frequencies, especially for frequencies less than 300 Hz. This, however, reduces near to 0.3 in case of part (b) which reflects results from Model-2 consisting of misaligned bundle interfaces. So, it would be reasonable to indicate that misaligned interfaces not only break the coherence of

flow features in the neighboring bundles of the misalignment location, but also, influence the flow away from the misalignment zone.

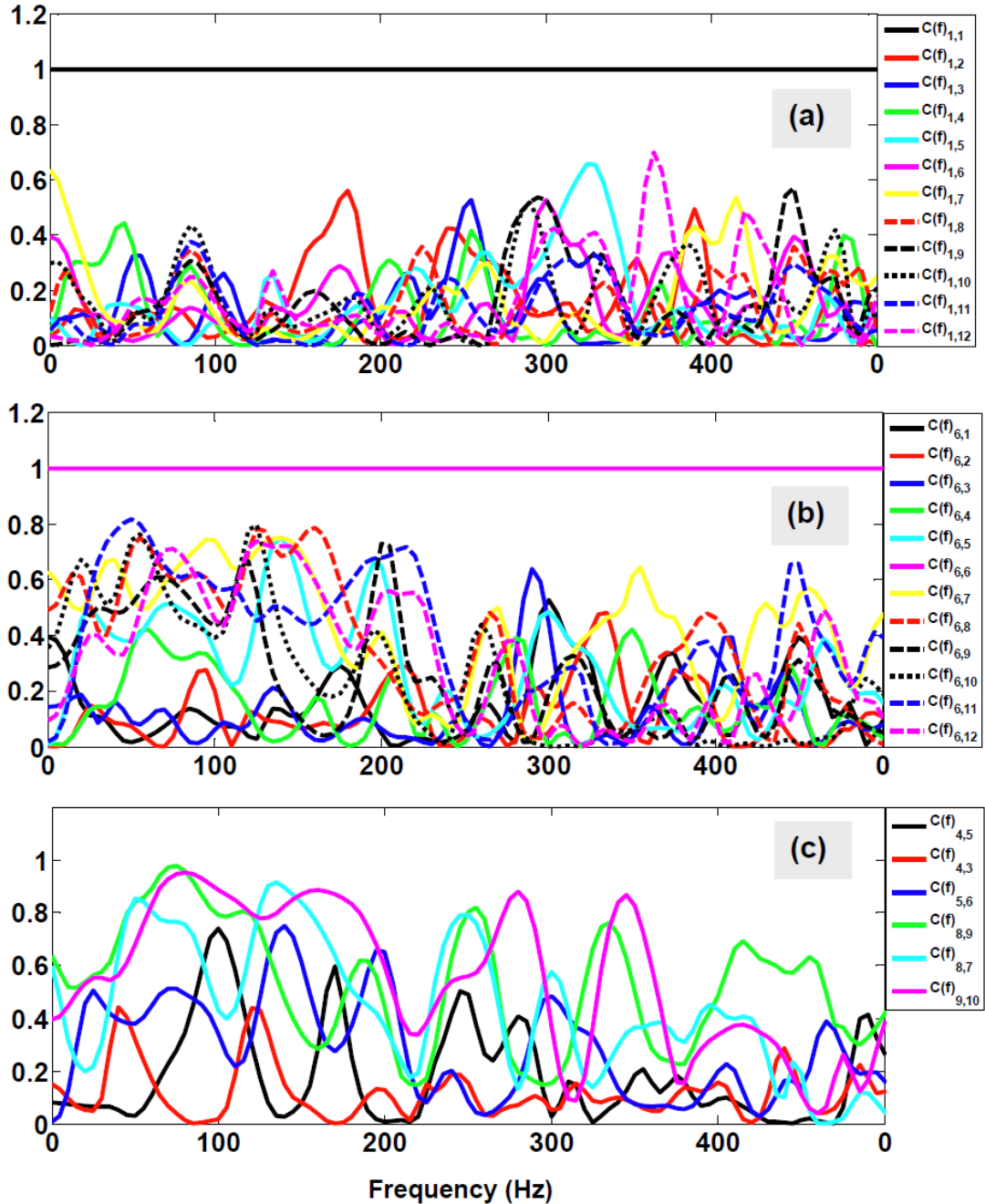


Fig. 3-19 Flow coherence plots for x-velocities from Model-1: (a) BD-1 with other bundles; (b) BD-6 with other bundles; (c) Bundles located near the misaligned interfaces in Model-2.

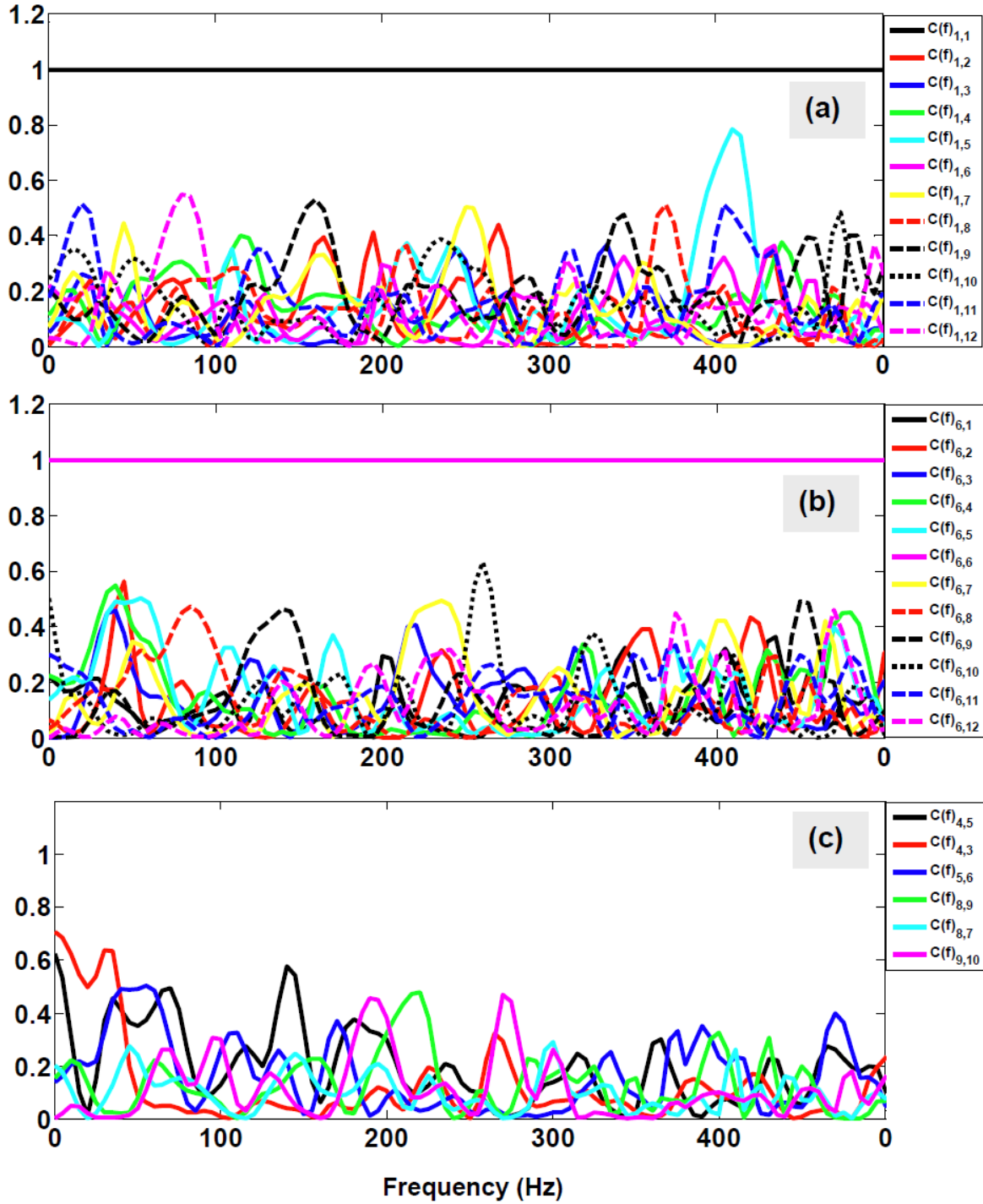


Fig. 3-20 Flow coherence plots for x-velocities from Model-2: (a) BD-1 with other bundles; (b) BD-6 with other bundles; (c) Bundles located near the misaligned interfaces.

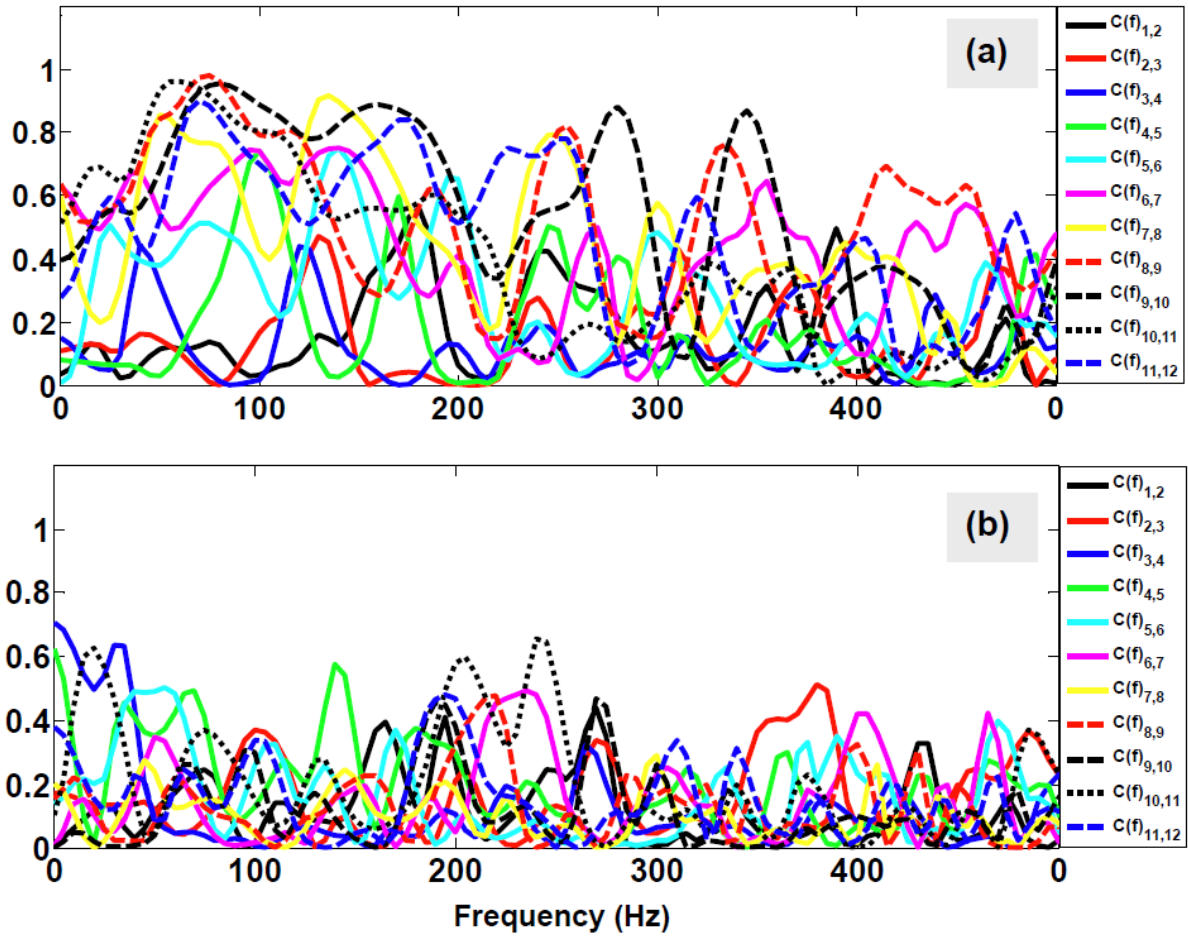


Fig. 3-21 Flow coherence plots for x-velocities for bundle-pair combination “P”: (a) from Model-1; (b) from Model-2.

The Fig. 3-23 compares the coherence of y -forces for the bundle-pair combination “P”. From part (a) this figure, it is observed that the y -forces become highly coherent in nature as the flow passes by from BD-1 to BD-12. This strong coherence reaching almost unity primarily occurs in the frequency range of 0 Hz to 300 Hz. The part (b) of the same figure elaborates that presence of misaligned interface decreases the coherence of the y -forces to about 0.5 and thus demonstrates the influence of the bundle angular misalignment on the fluid y -forces.

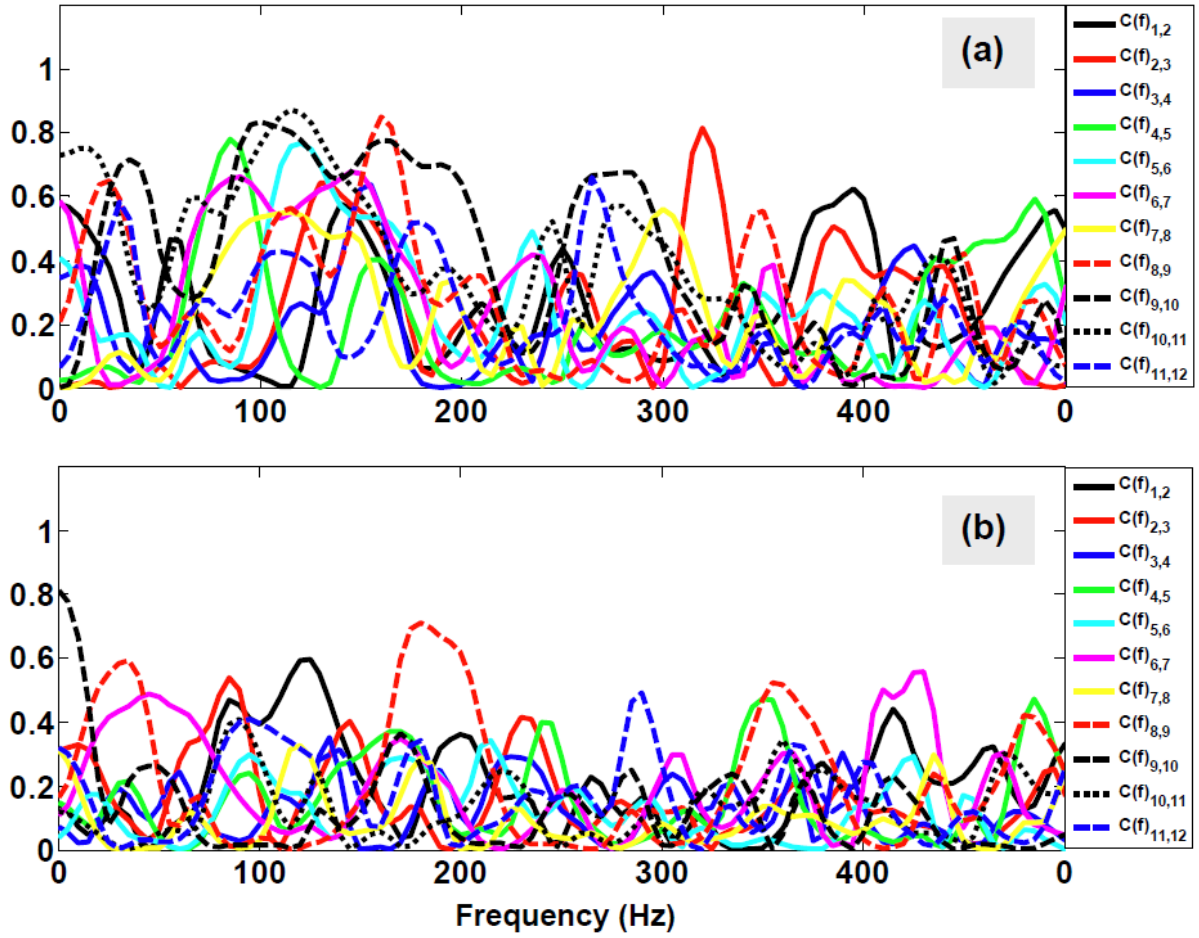


Fig. 3-22 Flow coherence plots for x-forces for bundle-pair combination "P": (a) from Model-1; (b) from Model-2.

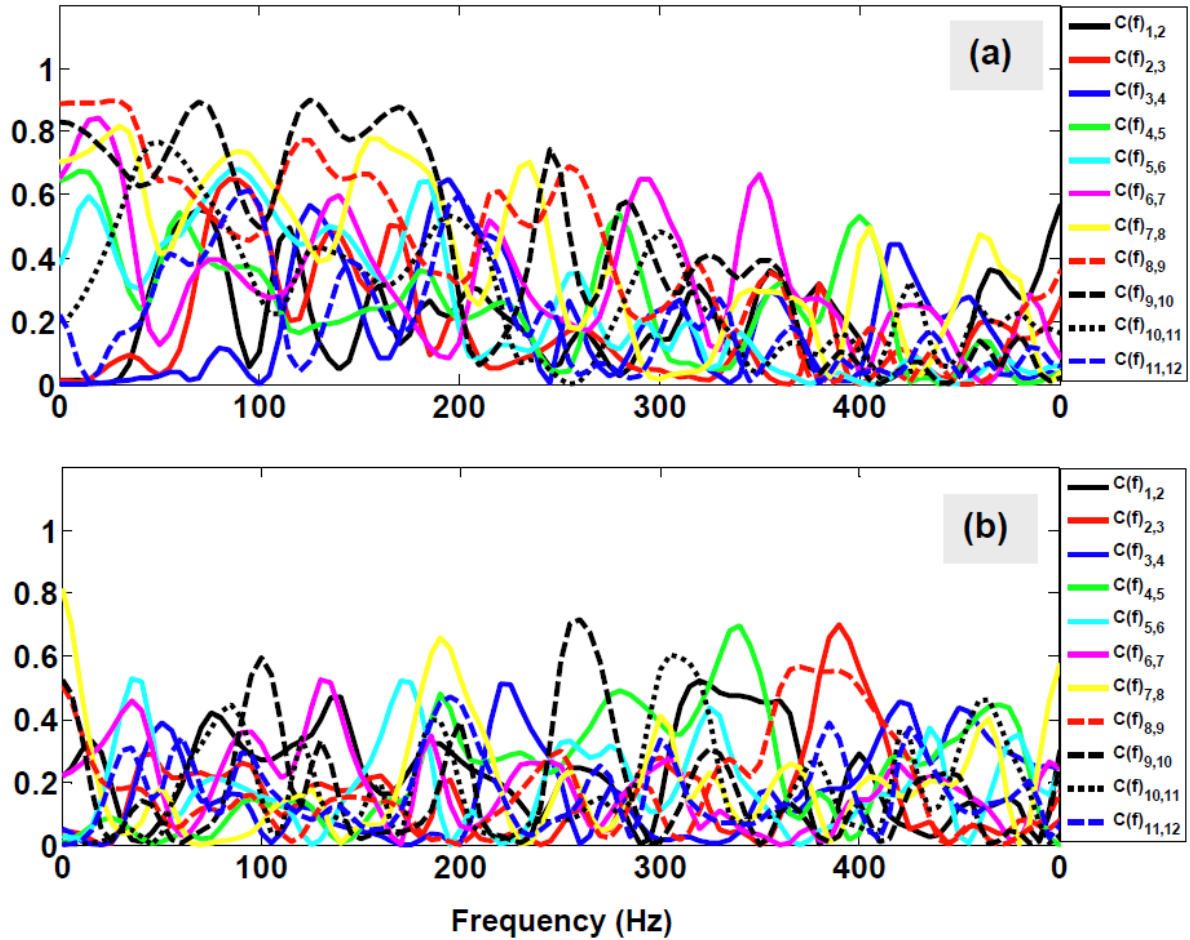


Fig. 3-23 Flow coherence plots for y-forces for bundle-pair combination “P”: (a) from Model-1; (b) from Model-2.

3.5 Summary

This 12-bundle computational work is novel from the following perspective: (a) the inclusion of the whole string of bundles in the CFD model – done for the first time, (b) evaluation of the lateral fluid excitations on each of the bundles in the string, (c) observation on the effect of angular misalignment in the bundle-to-bundle interface regions on the lateral fluid excitation and (d) observation of the frequency shifting of the fluid excitations on each of the bundles due to bundle angular misalignments.

The results of this numerical study reveal that lateral fluid excitations experienced by different bundles change with bundle angular misalignments at the interfaces. In actual practice, the pressure tube is filled up by a string of bundles and the present study shows that

in order to predict accurate fluid excitations on various bundles, inclusion of all the bundles in the fluid model is necessary.

Also, since, under an operating situation, the bundle orientations are beyond control, numerous combinations of bundle angular misalignment is possible, hypothetically, for a string of bundles. However, if any axial guidance can be made for the fuel bundles to stay in some angular position so that all fuel bundles in the string are placed fully aligned with each other, then both the mean and the RMS values of the lateral fluid excitations can be reduced significantly, as found in the present study. From the spectral study of the fluid forces, it is noted that the spectra change with varying bundle misalignment arrangements. Thus with misaligned interfaces, the bundles are more susceptible to the different frequencies of fluid excitations and hence, more chance of lateral vibration.

Moreover, the correlation study for different bundles reveals that the fluid features are correlated from one bundle to another bundle inside the fuel channel in both time and frequency domain. However, the level of correlation (coherence) depends upon the bundle-to-bundle angular position and the choice of bundle-pairs on which the correlation is performed. Strongest correlation is observed among intermediate bundles in case of fully aligned string of bundles. Misaligned interfaces present in the bundle string produce the weakest correlation or almost no correlation. This finding leads to the fact that for the flow modeling of fuel bundles, inclusion of all bundles is a not a choice but a necessity.

CHAPTER 4: INVESTIGATION ON BUNDLE ANGULAR MISALIGNMENT

Due to the high computational demand for a large-scale problem like the 12-bundle fuel channel model, as discussed in the previous chapter, a detailed analysis could not be done on the matter of the bundle angular misalignment within that large model. However, this can be dealt with by focusing on a fewer number of bundles in the whole bundle string, e.g., the first two inlet bundles; the justification for using the two inlet bundles is given in subsection 4.1.5.3.3. This chapter addresses the effect of bundle angular misalignment on the flow, and flow-induced excitations, in more detail. The study involves both computational and experimental investigations, and are presented in sections 4.1 and 4.2, respectively.

4.1 Computational study

4.1.1 Introduction

During refueling in a CANDU reactor, the angular positions of the fuel bundles are not controlled. As a result, the fuel bundles in a fuel channel tend to have different angular orientations and therefore, the possibility of angular misalignments among a string of fuel bundles exists. If any two adjacent bundles are resting inside the pressure tube with such an angular orientation that their components, viz., bundle-elements, endplate-ribs/rings, are in perfect alignment for the two bundles, then the configuration is considered as a fully aligned interface; and if not, then it yields a misaligned interface. A simpler case of bundle-to-bundle interface configuration considering 30° angular rotation for one bundle is illustrated in Fig. 4-1, and the results for several other angular misalignment configurations are presented and discussed later.

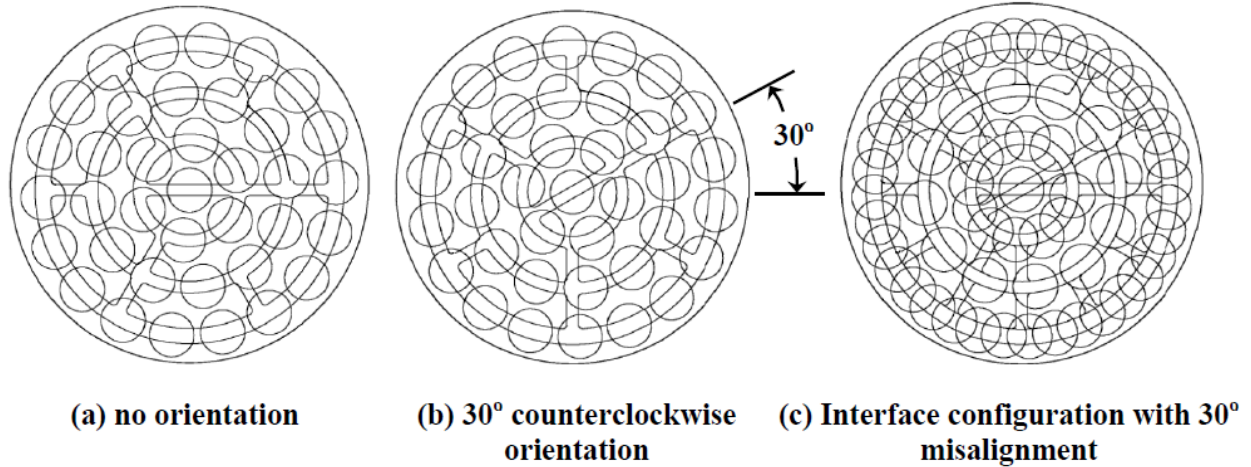


Fig. 4-1 Configuration of endplate and fuel-element with angular misalignment shown.

This part of study is a more comprehensive one as an extension of another work by Bhattacharya et al. (2011b), where only one misaligned interface is studied and is found to magnify the fluid lift forces acting on the inlet bundle about one order in magnitude. In this work, the focus is on the effect of the angular misalignments on the flow and flow-induced unsteady transverse forces on the bundle structures. To achieve this, several three-dimensional fluid dynamics models with bundle-to-bundle interfaces of different angular misalignments for two inlet bundles are developed and solved using an LES technique with the Smagorinsky SGS model.

4.1.2 Description of flow domain

This study considers CFD models which are developed, as shown in Fig. 4-2, and consist of a tube region of $6D$ in length (D being the pressure tube inner diameter), the flow subchannels of the entire first inlet bundle, and the flow subchannels of the first half of the second inlet bundle. The justification for the selection of the half length of the second bundle is based on the similar reasoning as mentioned in Chapter 2.

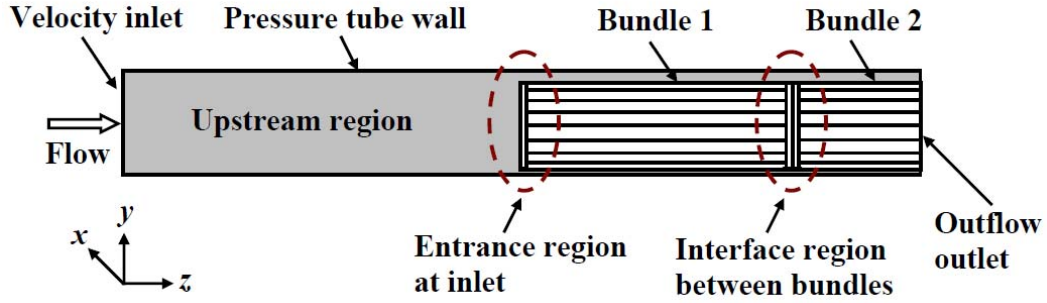


Fig. 4-2 Entire computational domain with boundary condition indicated.

4.1.3 Flow domain discretization

Based on the flow characteristics, the complete computational domain is divided into several regions – the upstream pipe flow and the flow through the BD-1 and half of the BD-2, as shown in Fig. 4-3. The BD-1 has three distinct flow regions: flow entering the upstream endplate subchannels, flow through the bundle subchannels and flow exiting the downstream endplate. The BD-2 has two distinct flow regions: flow entering the upstream endplate subchannels with an angular misalignment with the exiting endplate subchannels of the BD-1 and flow through half of the BD-2. The entire computational domain consists of unstructured meshes with approximately 7.7 million cells to precisely model the complex geometry pertaining to various subchannels and the segments of the fluid model.

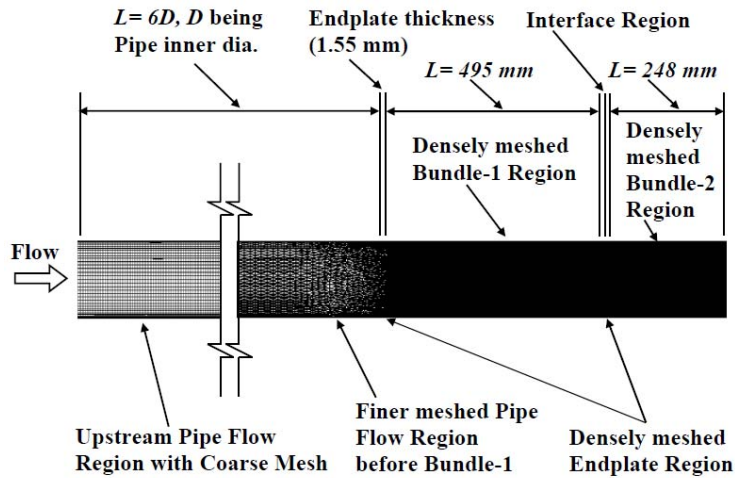


Fig. 4-3 Illustration of meshing scheme.

To meet the accuracy requirement of the LES scheme, the whole domain is discretized using an adequately fine mesh distribution, with endplate and bundle regions having the fine meshes and the upstream pipe flow region having coarse meshes. The grid distribution in various subchannels for the bundle and endplate regions along with the boundary layer distribution in the respective region in a cross section of the xy -plane is kept same as described for CFD model in Chapter 2 (refer Fig. 2-7). To comply with the demand of LES in regard to the near-wall mesh resolution, which is of critical importance, the thickness of the first layer of cells near the walls is restricted to a very low value to ensure y^+ equals 1 on most surfaces, while modeling boundary layer regions.

When considering numerical solutions of turbulent flow, determination of a suitable time-step size becomes one of the foremost requirements and key tools (Choi and Moin, 1994). For the present research, the time step size is based on the large eddy turn-over-time (LETOT), which is evaluated from the Kolmogorov time scale τ (as mentioned in Eq. (6) of Chapter 2) to be 2.4×10^{-4} seconds. The time step size in this study is chosen to be 5×10^{-5} seconds. Two different mean axial flow velocities, 2.4 m/s and 4.8 m/s, are considered at the inlet corresponding to an average velocity of 6 m/s and 12 m/s through bundle subchannels and a Reynolds number of 4.86×10^4 and 9.72×10^4 , respectively. Some details of the flow parameters considered in the current study are mentioned in Table 4-1.

Table 4-1 Flow parameters at different mean flow velocities.

Mean axial flow velocity at inlet (m/s)	Mean axial flow velocity inside bundle (m/s)	Reynolds number, based on average bundle D_h	Mass flow rate (kg/s)
2.4	6	4.86×10^4	20.9
4.8	12	9.72×10^4	41.96

The boundary conditions at different part of the flow domain are followed to be similar as described for the entrance flow model in Chapter 2. The computational models are solved at high temperature (300°C) and high pressure (10 MPa) with water used as fluid.

4.1.4 Solution technique and Computational resource

The LES technique, associated with Smagorinsky SGS model, is employed to solve three-dimensional filtered unsteady N-S equations. The LES scheme, as described in the Chapter 2, is followed for all the CFD models considered in this study. The detailed description of this LES scheme is, therefore, not repeated in this chapter and can be referred to Chapter 2 for any further information.

Using a cluster of supercomputers (36 in numbers), in conjunction with a parallel processing scheme, the numerical solutions are obtained for the three dimensional unsteady flow through the first two inlet CANDU fuel bundles. The convergence criteria is set to a value of 0.001 for flow parameters; with the time step size considered for several models, there is 2 (minimum) to 8 (maximum) iterations for every time steps in the LES solutions, thus conforming the non-linearity in solving the N-S equations.

4.1.5 Validation and grid sensitivity study

Like in Chapter 2, the numerical approach is validated comparing results from two different studies: (i) numerical and (ii) experimental. In regard to numerical scheme, the LES technique is verified first with the work done by Chang and Travoularis (2007). Then, the results from the current simulation is compared with experimental results documented by D'Arcy and Schenk (1987) for local axial flow velocity contours in certain subchannel part of the bundle cross-section. In both of these comparison, good agreement is achieved. For the details on the validation for this present study and also for grid sensitivity study please refer to Chapter 2.

4.1.6 Bundle-to-bundle angular misalignment

The 37-element bundle structure, considered in the present study, exhibits a periodicity of 60° in azimuthal direction in its cross-section (barring the central rib), indicating that the appearance of the elements in each ring is repeated after every 60° angular rotation. In other words, the bundle structure has six identical sectors in its cross-section; each sector consists of six elements and one sixth of the central element. So, all possible misaligned configurations can be attained by considering one fully aligned interface (0°) to next fully

aligned (60°) interface. The current study investigates the effect of bundle-to-bundle interface misalignment for different cases starting from 0° to 60° with an increment of 5° , as illustrated in Fig. 4-4. A careful observation will reveal that the misalignment orientations are in symmetry about an angular axis passing through the 30° orientation; thus the 30° misaligned configuration appears to create a moderate flow obstruction. Therefore, in the current study, primarily the contours and plots are compared between 0° and 30° situations; however, fluid excitation forces in the lateral direction on the bundle i.e., F_x and F_y are evaluated and discussed for all different misaligned interfaces. In Fig. 4-4, the reference rotating plane is shown by a dashed line, which is rotated every time by 5° to get the next misaligned configuration. It is noted that, the actual resting angular position of a fuel bundle is random although fuel bundles tend to have their most preferred orientations from the operating experiences.

4.1.7 Results

In this section, numerical results obtained from the CFD models are analyzed and discussed. Various cases are considered and results produced for different parameters. The total duration of solution for all different models is 0.5 s from which only 0.4 s (i.e., 0.1 s to 0.5 s) is considered for data processing because the solution became stable after 0.1 s .

The contours are presented as viewed from the upstream towards the downstream. Every contour plot consists of the endplate profile projected on it for better understanding of the effect due to the endplate, if any. It is to be noted here that although the contours exhibit flow parameters at certain moment, however, their distribution or the pattern remains similar at different time instants on that surface with very small changes in the magnitude. The discussion in the following section involves detailed review of the interface flow and its effect on the fluid forces experienced by the BD-1 with the help of Fig. 4-5 to Fig. 4-9. Then, emphasis is given on the effect of different angular misalignments in the bundle-to-bundle interface region, as can be seen from Fig. 4-10 to Fig. 4-15, in conjunction with Fig. 4-4.

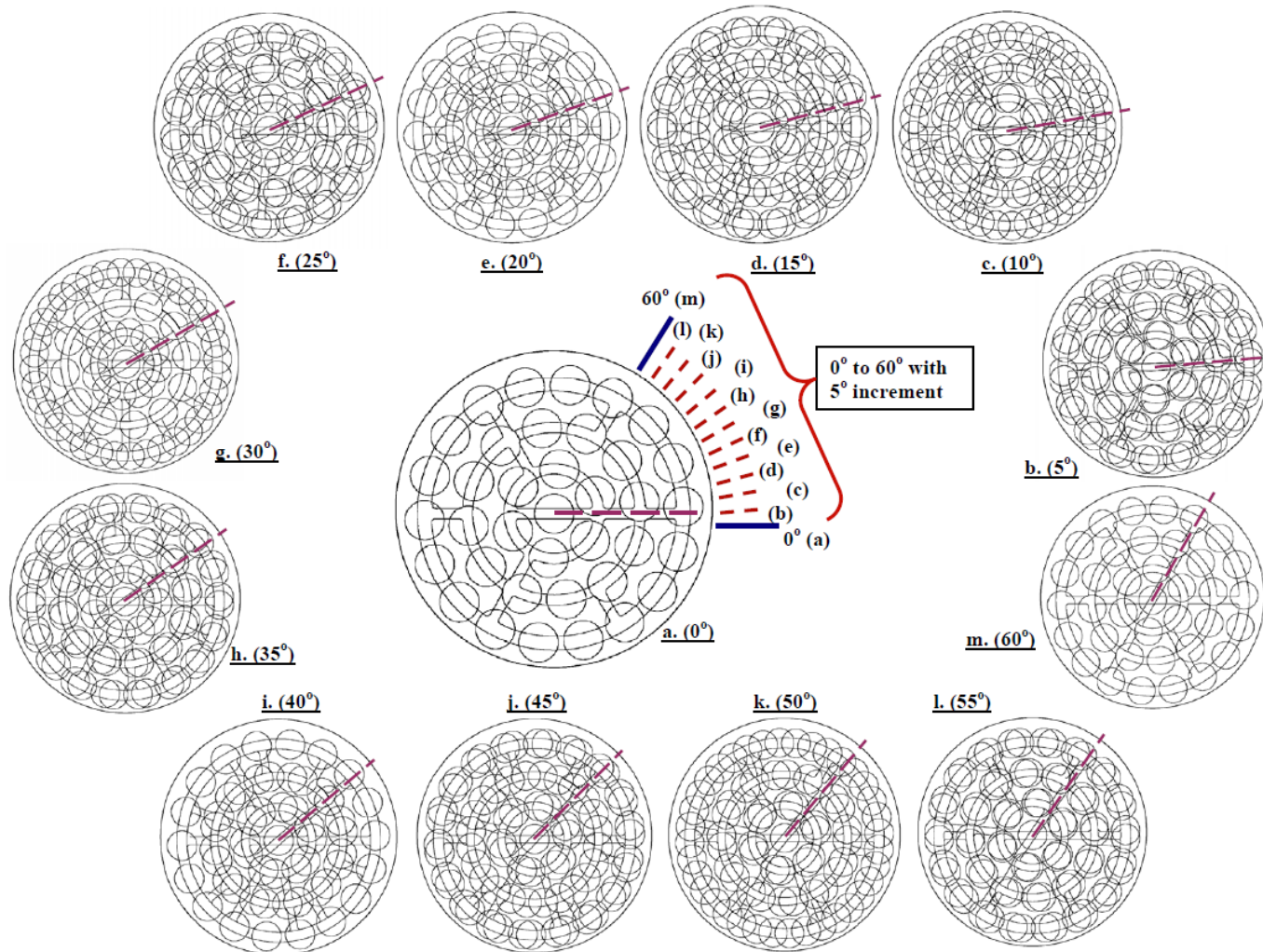


Fig. 4-4 Different angular misalignment configurations with 5° increments.

4.1.7.1 Discussion on y -velocities

The contours of the y -velocity components are shown in Fig. 4-5. Among the four contours, only midplane of first bundle displays a minimum y -velocity. This indicates that fluid flow becomes almost parallel subchannel flow without effective lateral components at the midplane of the bundle. Whereas, for other contours in (a), (c) and (d), the dominance of lateral components is higher, which indicates that the cross-flow caused due to the endplate is significant around the entrance and interface region. For Fig. 4-5 (a) and Fig. 4-5 (b), the contour plots are distributed in such a way that the right side shows flow of fluid through subchannels with positive velocity and the left side shows negative velocity. Thus, the local maxima and the minima for the y -velocity components are distributed in the opposite sides about the bundle vertical axis. This observation is not so prominent for (c) and (d). However, for (c) and (d), higher velocity is observed around locations right before and after the endplate ribs/rigs and their junctures.

4.1.7.2 Discussion on x -velocities

Like in the case of y -velocity, the contour corresponding to the midplane i.e., Fig. 4-6 (b) contains the lowest x -velocity components pointing out again that flow in the midway of the bundle does not have significant lateral components, representing a fully developed flow. However, the contours around the entrance and the interface endplates, i.e., (a), (c) and (d), exhibit higher x -velocity components, compared to that in (b). This evidences towards the existence of the cross-flow around endplates. Also, Fig. 4-6 (b) and Fig. 4-6 (c) show the distribution of x -velocity components in such a fashion that the local maxima and the minima are noticed in the opposite sides about the bundle horizontal and vertical axes, respectively. In (a), (c) and (d) of Fig. 4-6, it is seen that lateral velocity components are magnified before and after the endplate ribs/rings, proving again the influence of these endplate components in modifying the parallel bundle subchannel flow.

4.1.7.3 Tangential velocity

Distribution of tangential velocity components through the bundle subchannels at cross-sections of various axial locations are illustrated in Fig. 4-7. In Fig. 4-7 (a) and Fig. 4-7 (c), the middle and inner subchannel regions behind and ahead of the endplate for the BD-1 are

seen with high tangential velocity, with Fig. 4-7 (a) showing strong negative tangential velocity in the endplate ribs. The intensity of the tangential velocity component is found to be decreased in Fig. 4-7 (b) with more flow continuity established through the bundle subchannels, enhancing the presence of swirling like flow in the BD-1. This is, however, not evidenced in the case of BD-2, shown in Fig. 4-7 (d); but the existence of negative tangential velocity is again found after the interface endplate ribs, elaborating the importance of considering endplates and the bundle-to-bundle interface regions while modeling the bundle subchannel flow.

4.1.7.4 Radial velocity

The radial velocity components can also contribute towards the bundle lateral motion and hence, it is important to discuss it at this point in time. The contours of radial velocity components, which are shown in Fig. 4-8, display that the highest magnitude is attained for both locations right after the endplate for two bundles, i.e, (a) and (d). At the halfway through the BD-1, a radial continuity of flow through bundle subchannels with a low value is observed, as shown in Fig. 4-8 (b). In Fig. 4-8 (c), the locations between the adjacent elements in same endplate ring are found to show higher magnitude of the radial velocity components. This is because, at those locations, fluid particles tend to cross the interface endplate rings and thus spread in radial direction, providing higher bundle lateral movement.

4.1.7.5 Lateral fluid forces

Fluid forces on the BD-1 are presented in this section through Fig. 4-9. Due to bundle sagging, the CANDU fuel bundle has maximum gap between the outer elements and the pressure tube inner wall at the top. The bundle tends to move upwards under the influence of the lift force. It may be better to mention here that, from the operating experiences of the CANDU reactors, lateral fluid forces are of more interest while dealing with fuel bundle vibration. Hence, time histories and PSDs for the x -force (F_x) and the y -force (F_y), which are responsible for bundle side-to-side and vertical motion, respectively, for the BD-1 are presented here as the lateral fluid force.

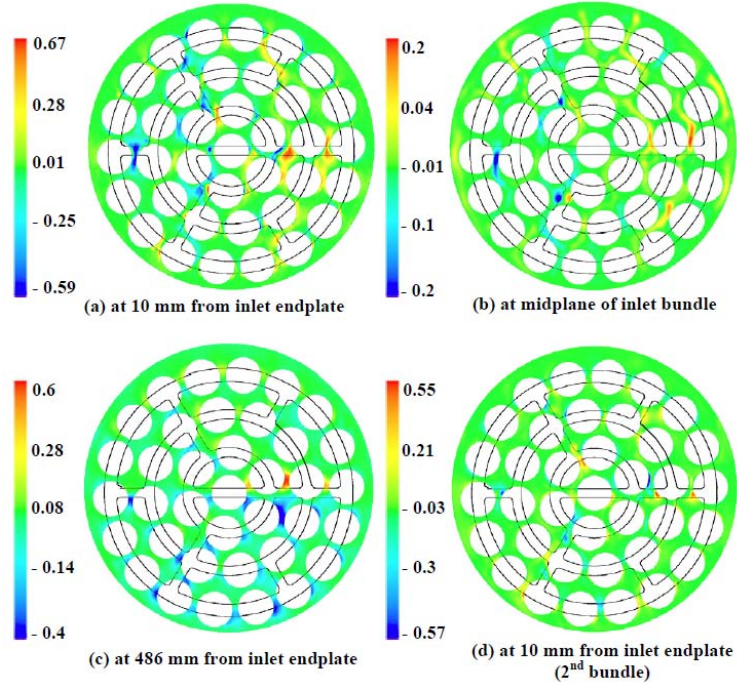


Fig. 4-5 Contours of y-velocity normalized by corresponding U at different axial locations for U of 2.4 m/s.

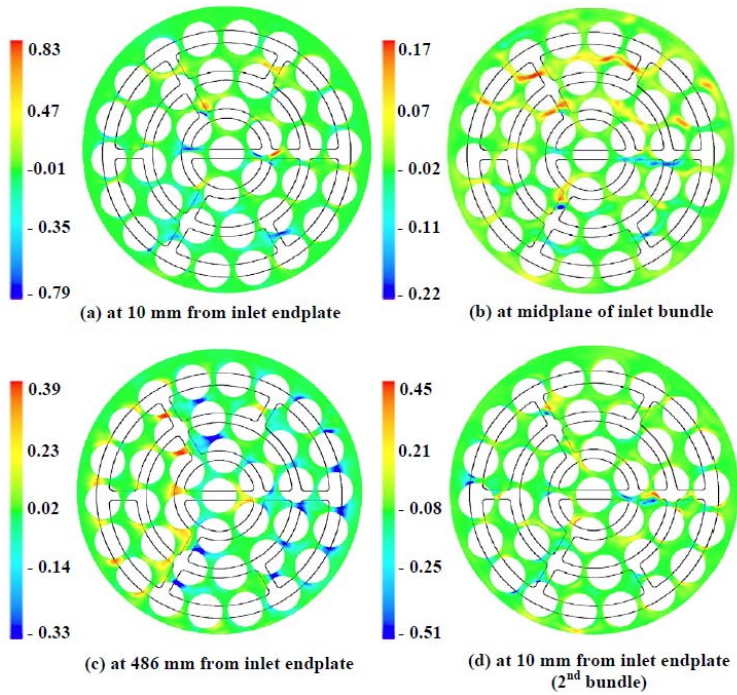


Fig. 4-6 Contours of x-velocity normalized by corresponding U velocity at different axial locations for U of 2.4 m/s.

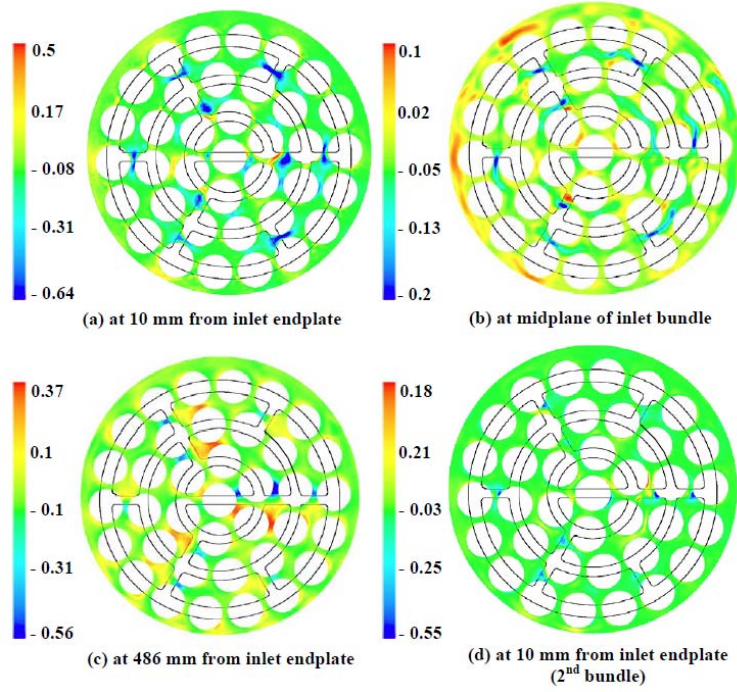


Fig. 4-7 Contours of tangential-velocity normalized by corresponding U at different axial locations for U of 2.4 m/s.

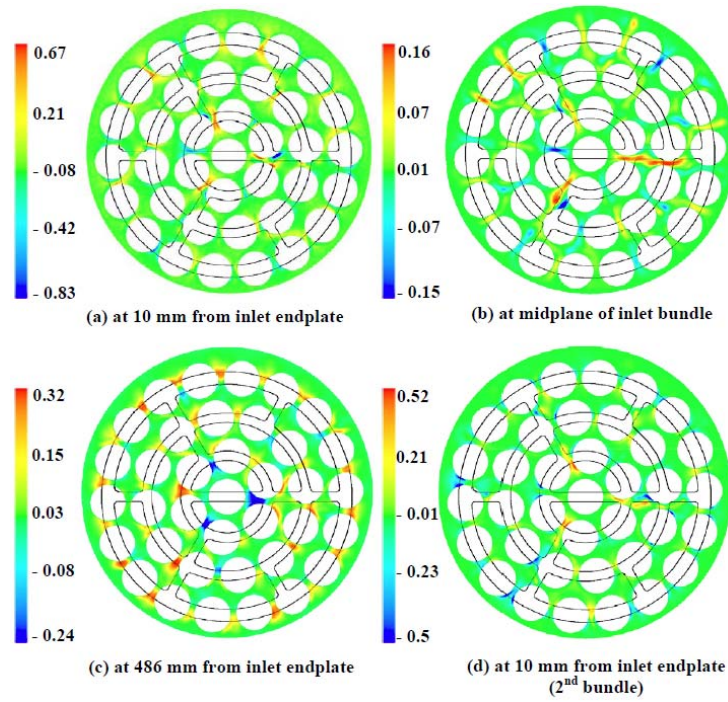


Fig. 4-8 Contours of radial-velocity normalized by corresponding U at different axial locations for U of 2.4 m/s.

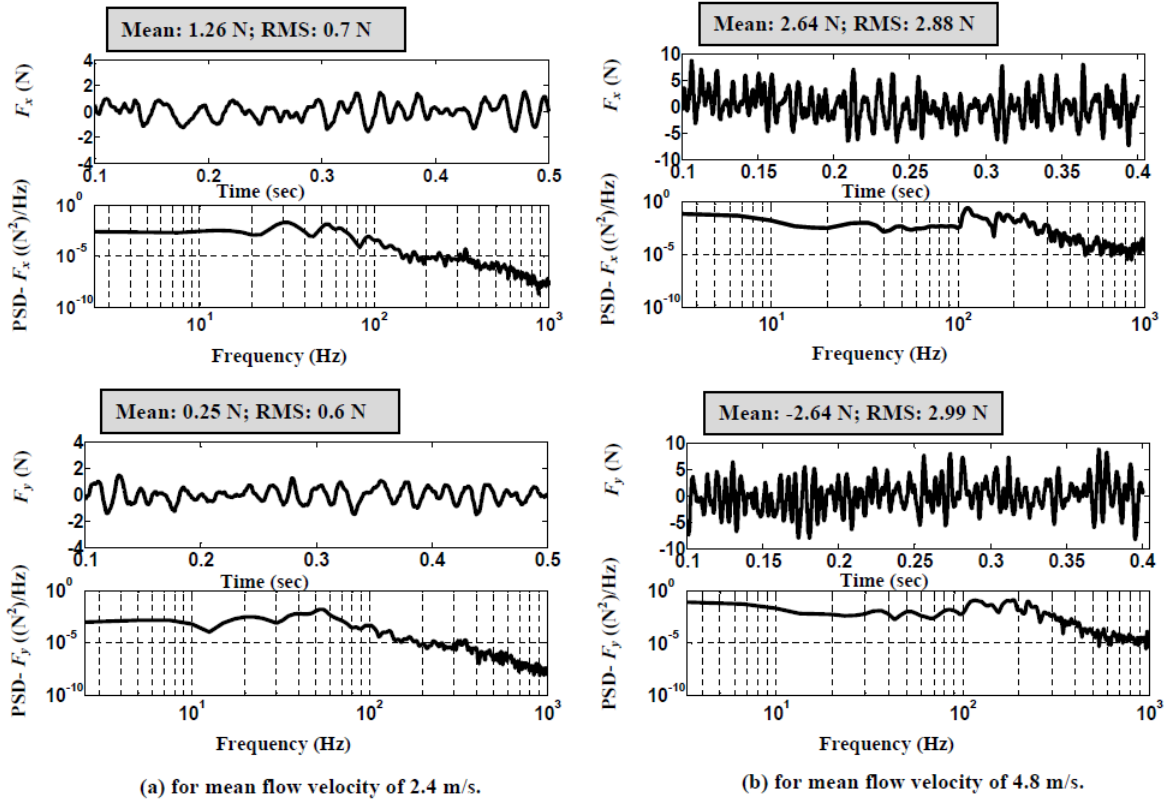


Fig. 4-9 Time histories and PSDs of x-force (side force) and y-force (lift force) for the first bundle for U of 2.4 m/s and 4.8 m/s.

The time histories, shown in Fig. 4-9, are presented after removing the mean from the actual data to show precisely the fluctuations, which is of importance to the dynamic study of the bundle motion. The mean and RMS values for each of the cases are mentioned separately for easy understanding of the readers. The amplitude of fluctuation and the mean values are found to be increased reasonably at U of 4.8 m/s for both F_x and F_y with higher frequencies shown up for higher mean flow velocity case. The x -force (F_x) has dominant frequencies at 30 Hz, 50 Hz, 90 Hz and 320 Hz for U of 2.4 m/s; and spread over around 110 Hz and 300 Hz for U of 4.8 m/s. The lift force (F_y) is found with dominant frequencies spread over around 65 Hz to 120 Hz for U of 2.4 m/s; and around 35 Hz to 220 Hz for U of 4.8 m/s. All these frequencies discussed here show that if the fuel bundles contain any of its natural modes in the vicinity of these frequencies, then the bundle will get energy for its vibration from these frequencies.

4.1.7.6 *Effect of angular misalignment*

The results discussed in the earlier sections provide an insight on the importance of the entrance and the interface regions in a string of bundles for having better knowledge on bundle lateral vibrations. In this section, the effect of the various angular misalignments in the bundle-to-bundle interface region is analyzed. Initially, a comparative study is performed between 0° and 30° alignment configurations for the two bundles, with the help of pathlines and velocity vectors. The choice of these two cases is already elaborated upon in section 4.1.4. Later on, lateral fluid forces, F_x and F_y , on the BD-1 are analyzed and produced for all different combinations of misaligned interface configurations.

4.1.7.7 *Pattern of flow shown by pathlines*

The pattern of the flow from the inlet endplate to the outlet end is shown by Fig. 4-10 and Fig. 4-11 with the help of pathlines at an instant of time, when viewed from the downstream end. The fuel elements are not shown to avoid possible obstruction in the viewing of the pathlines. As mentioned in section 4.1.5.2 that, although the flow parameters change with time, given the unsteady nature of the flow, the pattern of the flow remains similar. So, using pathlines to show the development of flow past the inlet endplate is thus justified. Pathlines created from different sources are shown by different colors, shown in Fig. 4-10 (a) for fully aligned case. This figure illustrates the front view and has six source locations (S1 to S6) for the pathlines indicated by the black dots; their selection is made to cover the clear subchannel regions and the regions beside the endplate ribs. As expected, pathlines coming from S1, S2, S3 and S5 show maximum scatter compared to the other pathlines. These locations are situated beside the endplate ribs, enabling the flow to follow certain path, influenced by the differential pressure right after the endplate. The development of the flow can also be seen very clearly through an isometric view, as shown in Fig. 4-10 (b).

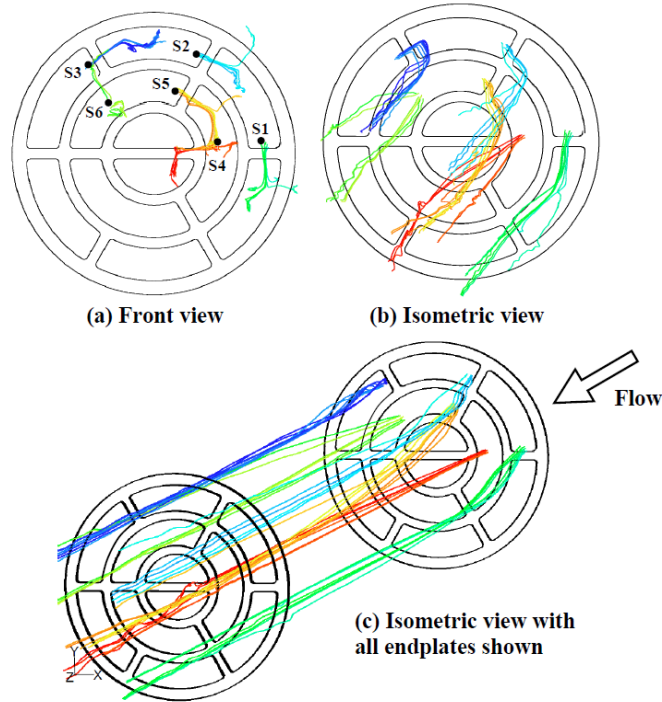


Fig. 4-10 Pathlines showing development of fluid flow with sources indicated by black dots when viewed from downstream side for aligned interface.

In the Fig. 4-10 (c), where all the endplates are shown, it can be seen that the flow almost recovers after the midway through the BD-1. However, fluid particles, encountering endplate ribs/rings at the bundle-to-bundle interface, undergo wakes when entering the BD-2. Particles which do not encounter endplate ribs/rings follow almost a straight path, as seen from the Fig. 4-10 (c).

The pathline generation for misaligned interface is elaborated with the help of Fig. 4-11. From Fig. 4-11 (a), it is clear that presence of misaligned interface influences fluid particle to scatter more compared to aligned interface, as seen from Fig. 4-10 (a). In addition, there are areas where fluid particles start to swirl in its own path, which is not at all seen for the aligned scenario. From the isometric view, shown in Fig. 4-11 (b), it is noticed that the flow deviations after the inlet endplate are present like the aligned model. However, unlike aligned condition, fluid particles in case of misaligned interface model undergo significant

wakes of higher magnitude after the interface endplate, as shown in Fig. 4-11 (b). Thus, this observation draws the importance of misalignment in the bundle-to-bundle interface region.

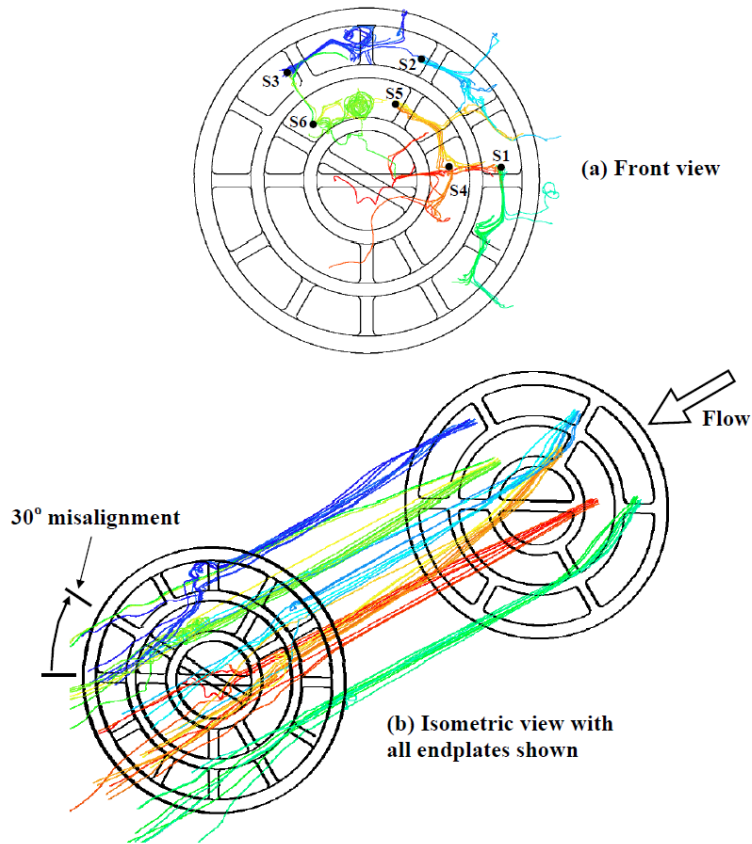


Fig. 4-11 Pathlines showing development of fluid flow with sources indicated by black dots when viewed from downstream side for misaligned interface.

4.1.7.8 Pattern of flow shown by in-plane velocity vectors

A comparative study of the in-plane velocity vectors, before and after the interface region, is presented with the help of Fig. 4-12 and Fig. 4-13. For both aligned as well as the misaligned scenarios, the pattern of velocity vectors is not very much different for the cross section before the interface, as seen in Fig. 4-12. However, after the interface, for aligned scenario, some locations with relatively higher flow velocity are observed due to the sudden change in the flow regime. Interestingly, for the misaligned scenario, many such locations with rotational flow pattern are observed. This indicates that the velocity profile and their

magnitude change significantly after the misaligned interface region compared to that of an aligned interface.

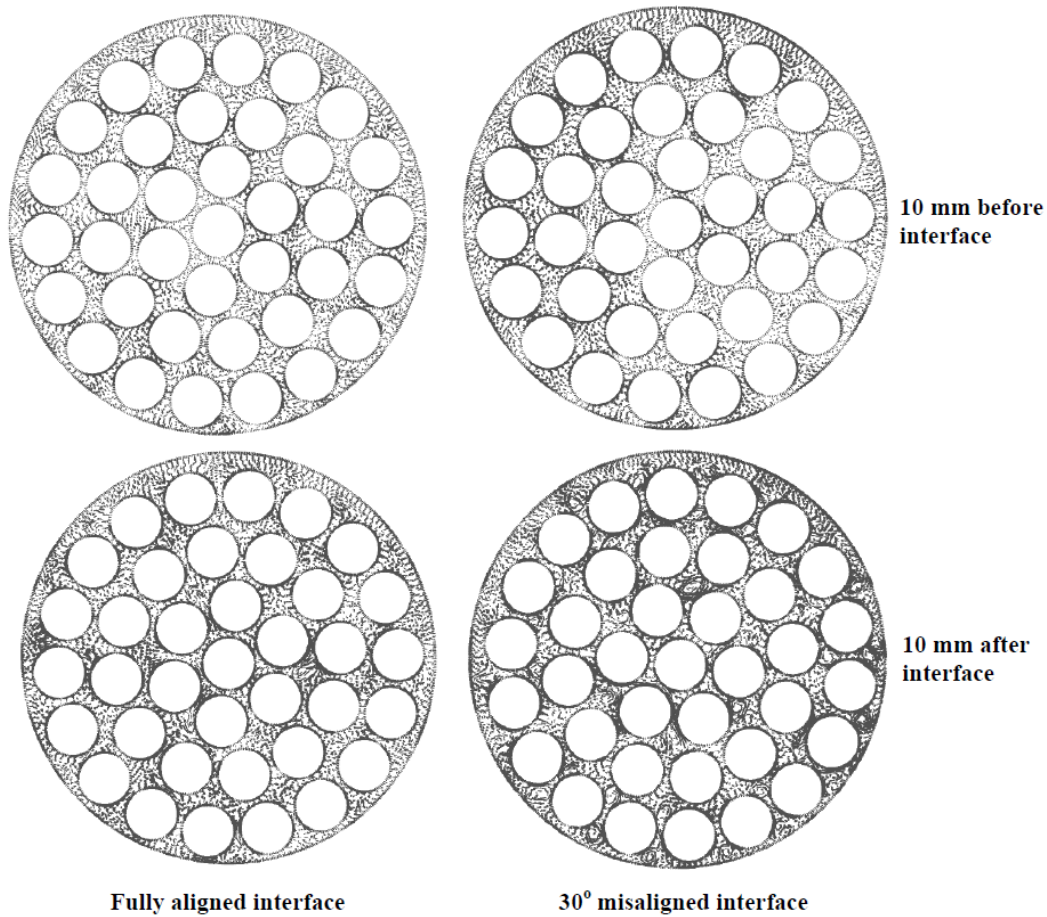


Fig. 4-12 In-plane velocity vectors (scale 20x) at locations before and after the interface.

To understand the direction as well as the magnitude of these vectors clearly, only a quarter of the whole cross-section is shown with a zoomed-in view of the velocity vectors, as can be found in Fig. 4-13. The endplate profile is projected onto these vector plots in order to show their orientation. For the cross-sections representing before the interface, it can be noticed that the magnitude increases and fluid particles are found to show higher movements through the subchannel regions to negotiate the blockage created by endplate-bundle element, in case of misaligned situation. But, after the interface, for the fully aligned scenario, some locations with relatively higher flow velocity are observed due to the sudden

change in the flow regime. Interestingly, for the misaligned scenario, many such locations with clearly visible rotational flow pattern of higher magnitude are observed. This indicates that the velocity profile and their magnitude change significantly after the interface region with angular misalignment.

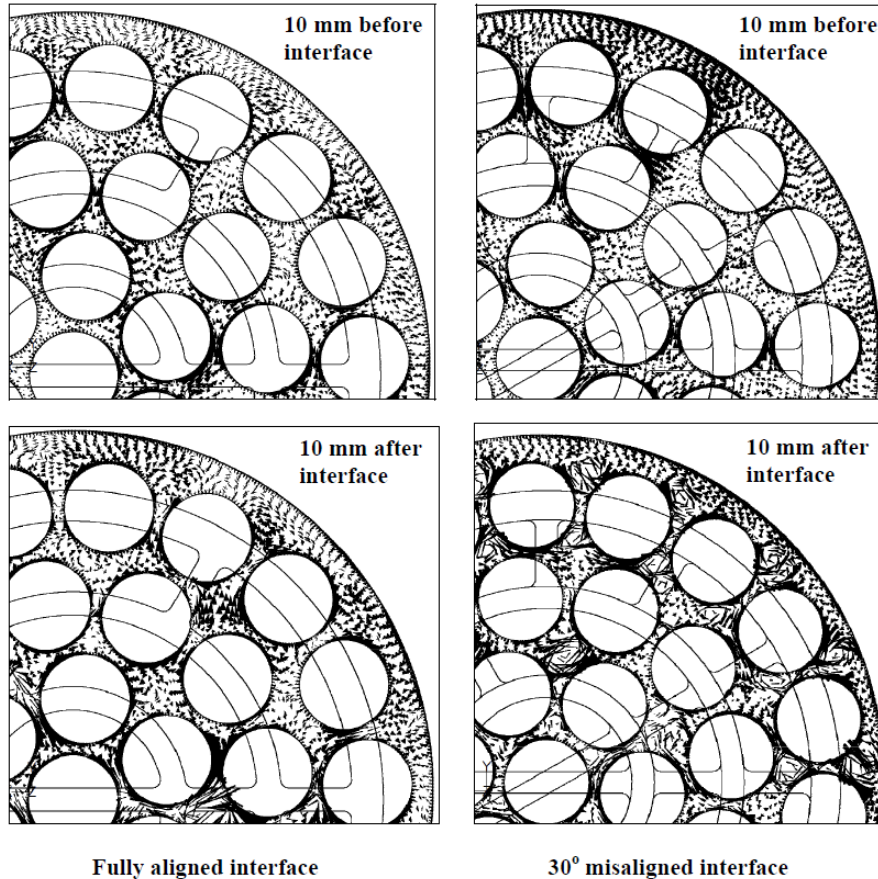


Fig. 4-13 Zoomed view of in-plane velocity vectors.

4.1.7.9 Mean and RMS values lateral fluid forces

To see the effect of misalignment on the bundle side-to-side force (F_x) and the lift force (F_y), the time histories and the PSDs are compared for the inlet bundle, which can be seen in Fig. 4-14. The mean is again deducted from the raw data and the fluctuation part is produced. For every plot the corresponding RMS and the mean values are shown separately. It is very important to mention that not only the mean values are increased with misaligned interface

scenario, but, the fluctuation range or the RMS values are also increased for both the F_x and F_y , when there is 30° angular misalignment. The F_x has the dominant spikes at 30 Hz, 55 Hz and 90 Hz; whereas, for F_y the frequencies are spread over a wide spectrum of band. Thus, this is very much of interest that the misaligned interface between bundles can produce considerably higher lateral fluid forces compared to that of fully aligned case.

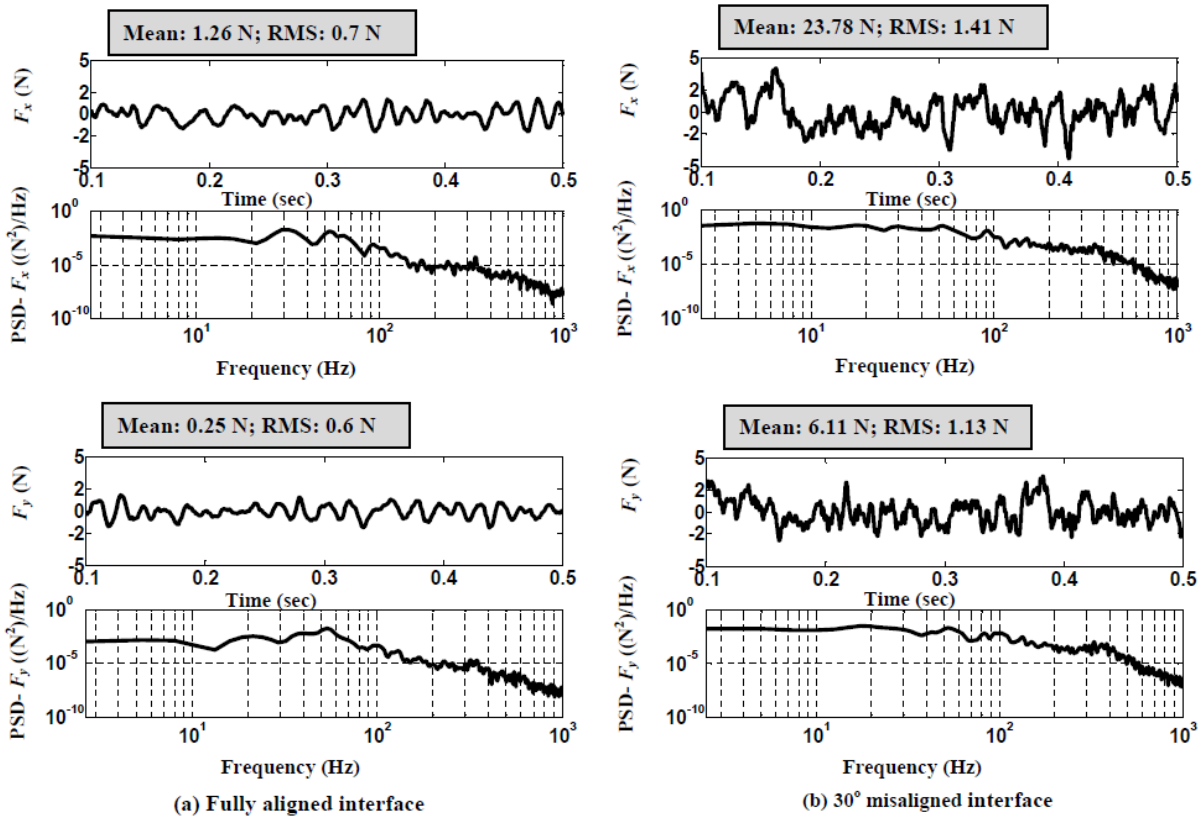


Fig. 4-14 Comparison of x-force and y-force for aligned and misaligned interfaces.

The next is to develop several CFD models with different angular misalignments starting from 0° to 60° with an increment of 5° . All configurations considered can be found in Fig. 4-4. For each of these orientations, the F_x and F_y on the BD-1 is recorded and processed for further analysis. The RMS and the mean values for each case are and can be found in Table 4-2. The mean as well as the RMS are presented by plots with different angular misalignments in Fig. 4-15. From the two graphs of Fig. 4-15, it is clearly seen that the

mean values vary with the change in the angular misalignments for both F_x and F_y . For the F_y , the mean follows a decreasing trend and for F_x it has increasing trend. Also, the change in the RMS values for x and y -fore is noticed to be significant. This is very important that angular misalignments influence the inlet bundle to experience lateral fluid excitations, much higher in magnitudes, about 3 times higher for RMS values and more than one order of magnitude for mean values.

Table 4-2 Mean and RMS values of fluid forces on the first bundle at different misalignment angles.

Processed Force values (Columns)	Horizontal-force, F_x (N)		Vertical-force, F_y (N)	
	Mean	RMS	Mean	RMS
Misalignment in degrees (Rows)				
0	1.26	0.70	0.25	0.60
5	4.93	1.21	9.58	1.37
10	7.46	1.64	13.84	0.17
15	11.85	1.52	15.19	1.61
20	15.92	0.81	3.25	0.86
25	20.81	1.37	9.54	1.37
30	23.78	1.41	6.11	1.13
35	27.20	2.76	3.01	1.79
40	29.28	0.69	-5.95	0.78
45	33.73	1.8	-0.47	1.78
50	37.52	1.77	-1.35	1.43
55	19.31	1.66	-11.12	1.76
60	34.51	0.73	-17.73	0.55

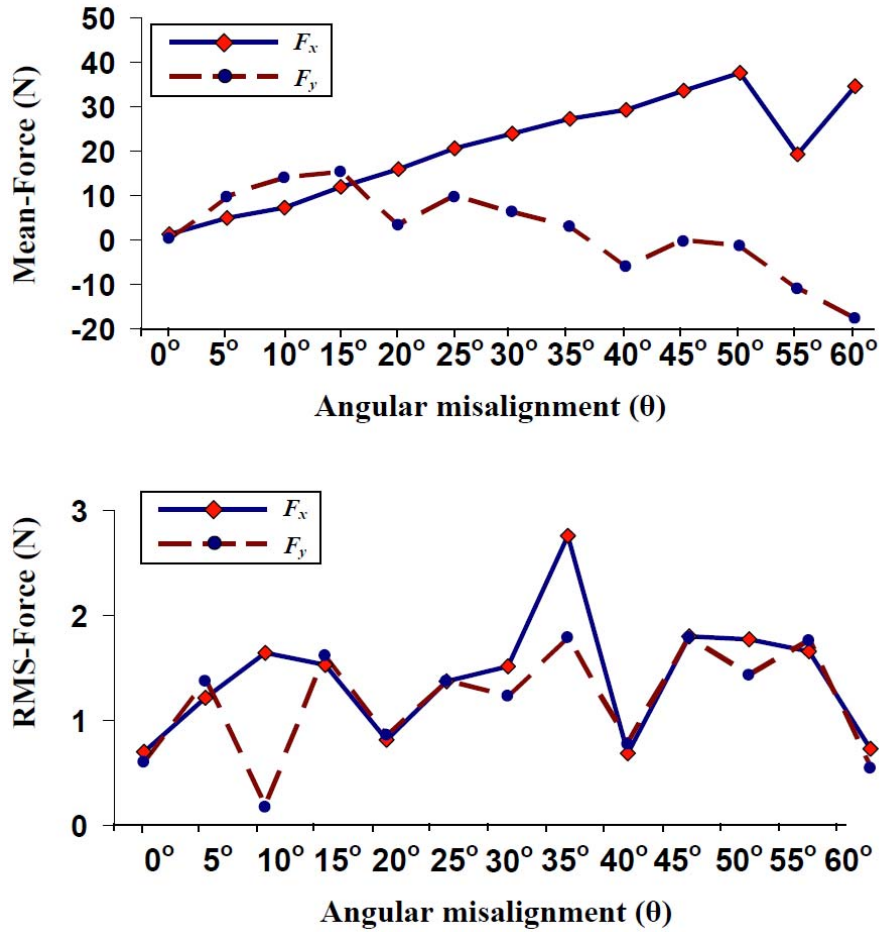


Fig. 4-15 Mean and RMS values of x and y-force on the first bundle at different alignments.

4.1.8 Findings from the computational study

In this study, comprehensive CFD models for a two-bundle string are developed for the first time to examine the effect of the angular misalignments on flow through CANDU fuel bundle structures and flow-induced unsteady forces in lateral directions. The increase of the lateral unsteady forces varies with the change in angular misalignments. The highest RMS and mean value of the lateral forces are found to increase by about 3 times due to an angular misalignment of 35° and more than one order of magnitude due to an angular misalignment of 50°, respectively. This mean value is the steady part of the fluid flow and the RMS represent the fluctuations. These are one the most significant findings to date in dealing with the mechanisms of flow-induced vibrations of CANDU fuel bundles.

4.2 Experimental study

4.2.1 Introduction

This section describes an experimental investigation carried out on flow-induced vibration of two simulated 43-element CANDU fuel bundles with angular misalignment in an out-reactor fresh water loop. Experimental data are presented and discussed for a range of (a) bundle angular misalignment and (b) mass flow rate in the subsequent sections.

4.2.2 Description on test facility

The experimental setup, as shown in Fig. 4-16, consists of a feeder pipe, a return pipe, a 4 inch diameter piping loop with a straight and transparent section of PVC pipe, a seven-vane centrifugal pump driven by a 10 HP electrical motor, a magnetic type flow meter and a pump-controller speed controller. The flow meter is used to measure the water flow rate at different pump-shaft operating speeds during experiments. Use of a transparent flow channel is to visualize bundle movement and to detect the presence of air bubbles within the water. The whole piping system is supported by nine steel columns anchored on the concrete lab floor. The two simulated bundles are placed inside the test section and held at their positions by a shield plug at the downstream end.

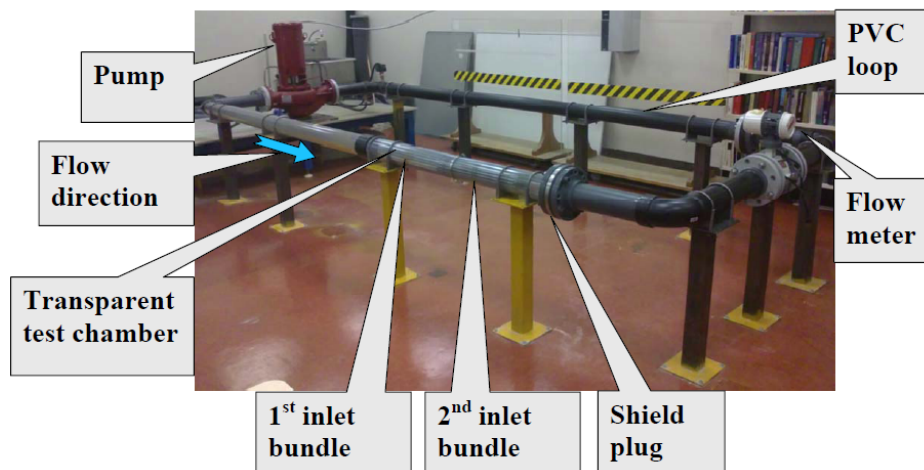


Fig. 4-16 An out-reactor experimental setup.

The flow rates of the centrifugal pump are determined by the rotational speeds of the AC motor, which are adjustable through a controller in the range of 0 to 30 Hz with a 0.5 Hz increment. Because of the load effect, a small slippage of the motor speed is observed. With the experimental setup, a maximum mass flow rate of 28 kg/s may be achieved when two bundles are placed inside the test section. It is noted here that, because of the use of seven-vane impeller, the flow pulsational frequencies normalized to the shaft rotational speed are expected to be in multiples of seven. It is also worth mentioning here that, before the start of each experiment, all sections of pipe in the test loop are filled up completely with fresh water to eliminate the air bubbles.

A simulated 43-element CANDU bundle consists of 43 stainless fuel elements welded to two identical stainless steel endplates in three radially spaced rings and two central webs. The outer ring has 21 fuel elements; the intermediate ring has 14; the inner ring has 7; the centre has one. The outer ring fuel elements have bearing pads at three axial locations to support the bundle weight through contacts with the test tube. As illustrated in Fig. 4-17, each endplate has three concentric rings for holding the fuel elements in desired locations. These rings are connected by radial ribs and central webs. The length of the simulated bundle is 500 mm. The center and inner ring fuel elements have diameter of 13 mm; the remaining fuel elements are 11.2 mm in diameter. The bundle has an average hydraulic diameter (D_h) of 8 mm.

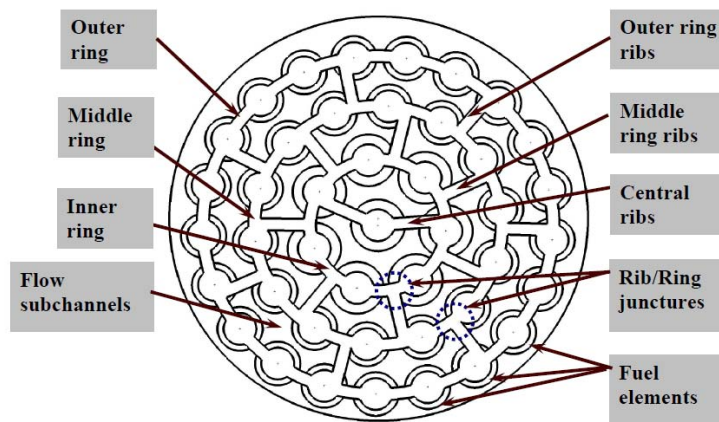
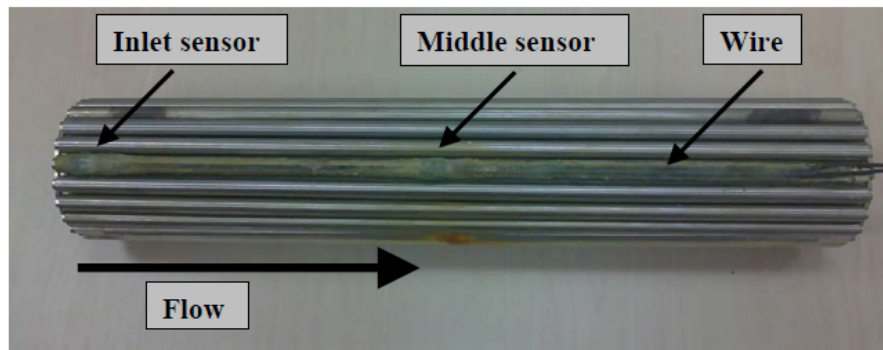
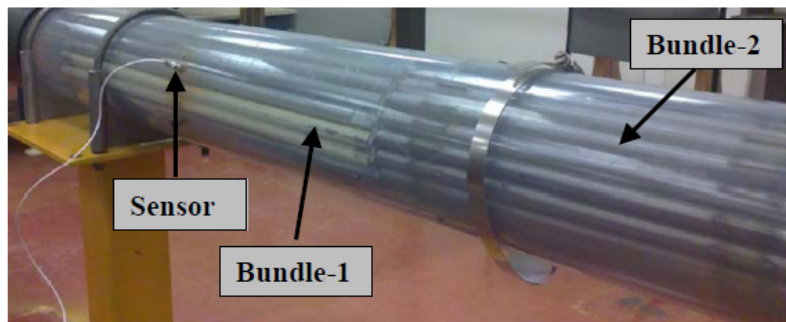


Fig. 4-17 Side view of a simulated 43-element fuel bundle.

Two MEMS-based biaxial accelerometers, ADXL203 from Analog Devices Inc., are mounted on the topmost outer element of the first inlet bundle, one at 15 mm from the inlet endplate and the other at the mid-span of the same fuel element. The highest sensing frequency of MEMS-based biaxial accelerometers is 2.5 kHz. The sensitivity of the sensor is 1000 mV/g with a measuring range of $\pm 1.7g$, a measuring error of $\pm 0.1\%$ and a resolution of 1 mg. Marine glue is used to seal the sensors from water. Signals recorded during experiments are accessed with the help of separate water-proof and noise-proof cables laid on the top surface of the outer fuel element at the 12 o'clock position, as shown in Fig. 4-18 (a). The analog electrical signal is acquired, digitized and stored using a data acquisition system (two units of Handyscope HS4) and a personal computer.



(a) Accelerometer



(b) Displacement sensor

Fig. 4-18 Locations and mountings of accelerometer and displacement sensor.

In addition to the above mentioned accelerometer, a non-contact differential variable reluctance transducer, NC-DVRT-1.5 from MicroStrain Inc., is installed at a location shown in Fig. 4-18 (b) to monitor the lateral (horizontal) movement of the bundle in relation to the supporting tube. The sensor measured directly the gap between a target face on the fuel bundle and its own face at the sensor head. When the face of the sensor probe comes in close proximity to a ferrous or highly conductive material, the reluctance of the coils within the sensor changes and provides the output as a voltage signal. The typical repeatability of this type of sensor is $\pm 2 \mu\text{m}$; the frequency range is 0 to 800 Hz. The sensor has a sensitivity of 5 V/mm with a measuring range of 1.5 mm and an error of $\pm 0.2 \%$.

A sampling rate of 19.531 kHz is used to sample all signals for a duration of 6.71 seconds for each test. It is to be noted that this sampling frequency is a pre-set value in the system corresponding to 20 kHz frequency; with this pre-set frequency the maximum measurement duration can be attained up to 6.71 sec. Since highest sensing frequency of the sensor is below 2.5 kHz, the adopted sampling rate is well above the Nyquist frequency. No aliasing problem is anticipated.

4.2.3 Experiments

For a two-bundle string, the bundle orientation angles (α_1 and α_2) are defined in Fig. 4-19. The angular misalignment (θ) is defined in this figure as the difference between the angular positions. In a CANDU reactor, the bundle orientation angle is not a controlled parameter during fuelling and refuelling. Therefore, a distinct possibility of angular misalignments exists between neighbouring fuel bundles. The fuel elements for a 43-element simulated bundle are designed to have a rotational periodicity of seven (or 51.4°) in the azimuthal direction. Except for the two central webs, the ring-rib sub-assembly of the 43-element endplate also has a rotational periodicity of seven. Considering this dominating structural periodicity for the 43-element CANDU bundle, it is assumed that the effects of the angular misalignments are largely periodic with a periodicity of 51.4° for the bundle-obstructed pipe flow.

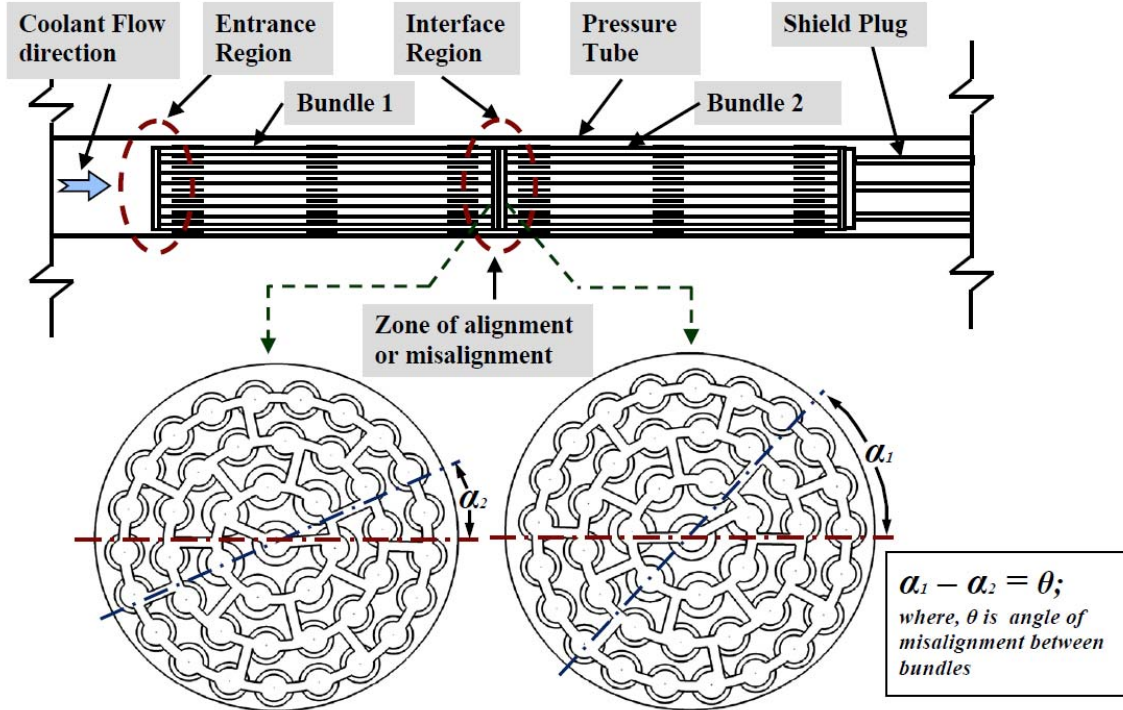
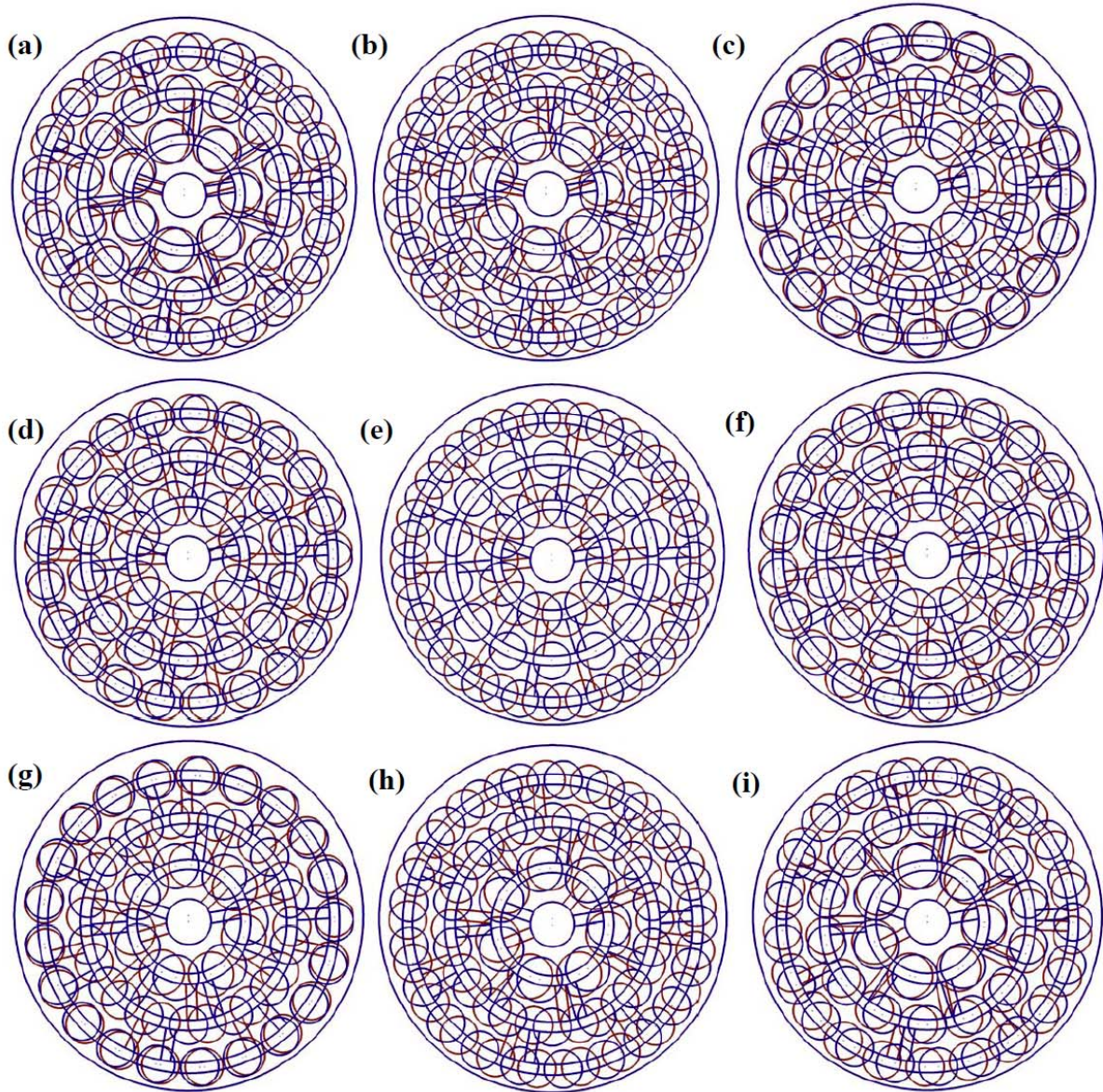


Fig. 4-19 Present experimental domain with misalignment between bundles explained.

In the current study, the angular position of the first (or inlet) bundle is fixed to be the design position ($\alpha_1 = 0^\circ$) while the second bundle is rotated from the perfectly aligned position ($\alpha_2 = 0^\circ$) to the next nearly perfectly aligned position ($\alpha_2 = 51.4^\circ$) with an increment of 5.14° . Except for the two nominally aligned cases ($\theta = 0^\circ$ and 51.4°), all other misaligned configurations are illustrated in Fig. 4-20.

All experiments were performed in the room temperature. A static pressurization of 20 psi is applied to the close loop. The Reynolds numbers, water mass flow rates, mean flow velocities both in the pipe and inside the bundle, the shaft speeds at different flow conditions are given in Table 4-3. Simultaneous sampling of the acceleration and displacement signals in each test is done through the data acquisition system; the data are stored for processing and analysis.



Misalignment configurations between bundles with θ value as follows:
 (a) 5.14° ; (b) 10.28° ; (c) 15.42° ; (d) 20.56° ; (e) 25.7° ; (f) 30.84° ; (g) 35.98° ;
 (h) 41.12° ; (i) 46.26°

Fig. 4-20 Different angular misalignment configurations in the bundle-to-bundle interface region.

It is worth mentioning here that the mounting of the sensors used and associated cables require some amount of material removal from the respective fuel element - a minor modification to the original bundle structure.

Table 4-3 Flow parameters at different speed settings for 25.6° misalignment.

Pump shaft speed (Hz)	Mean flow velocity in the pipe (m/s)	Mean flow velocity inside the bundle (m/s)	Reynolds number based on average bundle D_h	Mass flow rate (kg/s)
10	1.07	2.4	19,200	8.56
15	1.65	3.71	29,680	13.22
20	2.25	5.06	40,480	17.97
25	2.83	6.37	50,960	22.6
30	3.43	7.7	61,600	27.36

For each setting of bundle configuration, tests are conducted with the motor controller speeds from 10 Hz to 30 Hz with a 1 Hz increment. For each speed setting, two measurements of the steady state vibration were taken. A strong repeatability in both time and frequency domains was observed for the responses under the same test conditions. The time histories and PSDs for an arbitrarily picked test in the experimental database are shown in Fig. 4-21. In addition to this figure, the repeatability can also be verified from Fig. 4-22 and Fig. 4-23 where statistics of the measured signals are plotted for more number of tests. Due to the fine repeatability, only one set of measurement was taken and used in this study.

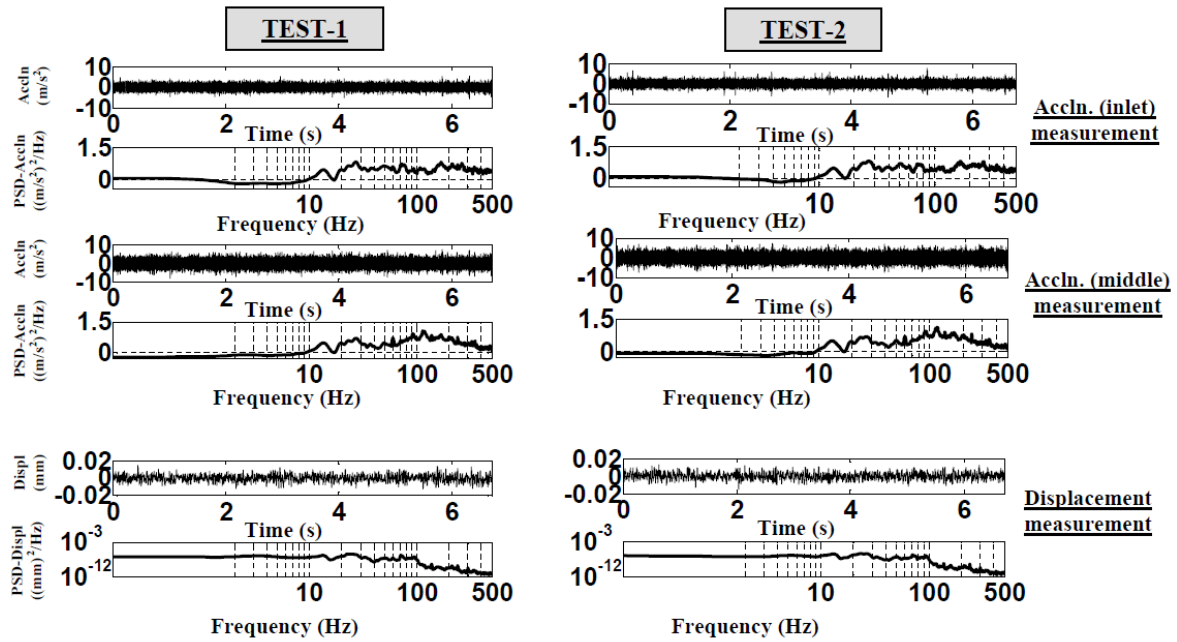


Fig. 4-21 Repeatability checking shown by time histories and PSDs of measured acceleration and displacement responses.

4.2.4 Results and Discussions

Large number of vibration data in the time domain obtained for a range of configuration and operational parameters are processed and analyzed in this section.

4.2.4.1 Stationarity of recorded vibration signals

A stationary time signal is one whose statistical properties such as mean, variance, autocorrelation, etc. remain constant over time. A turbulent flow, after an initial transient period, can reach a statistically stationary state in which their statistics are independent of time (Pope, 2000) even though the flow variables vary with time.

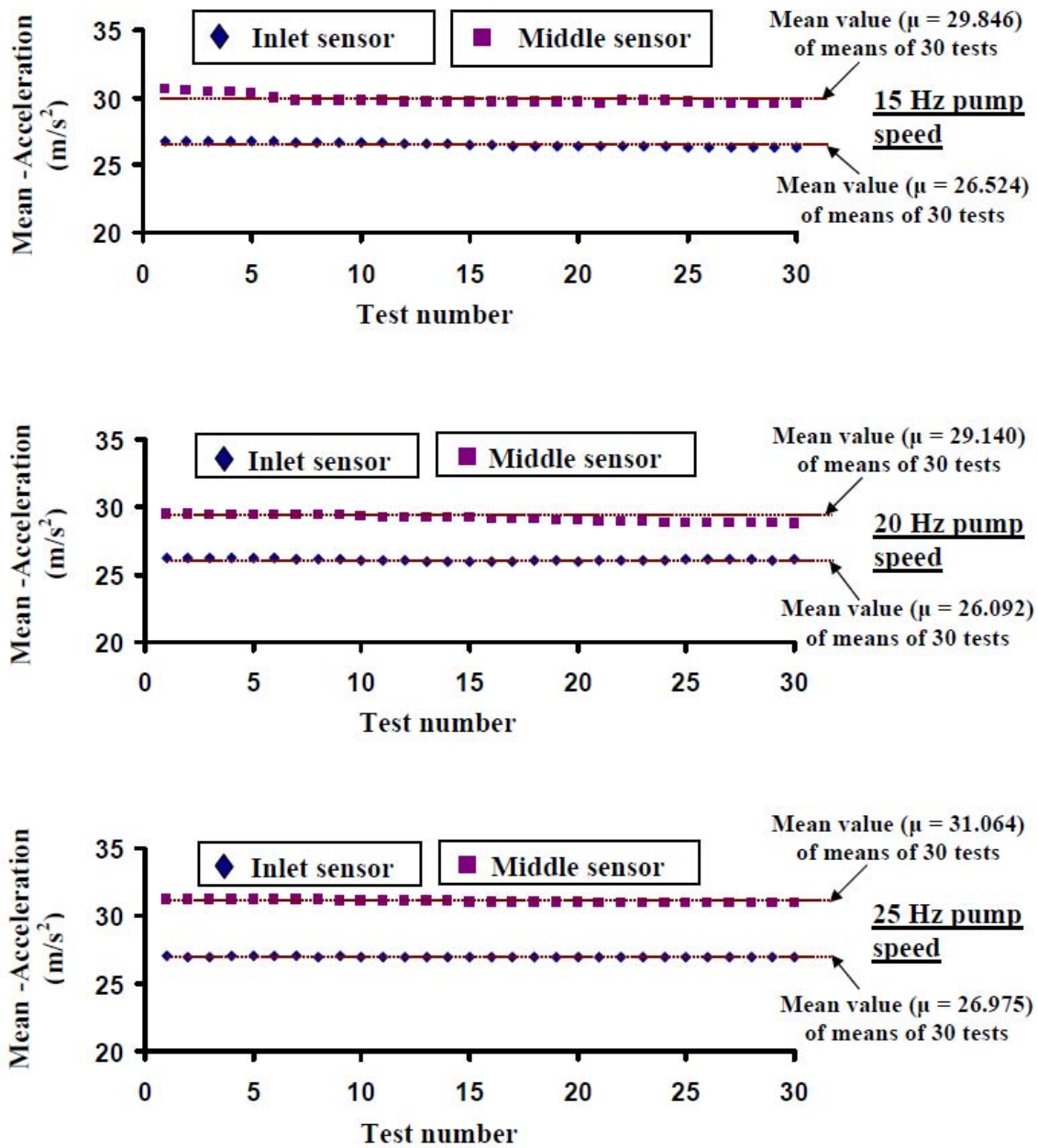


Fig. 4-22 Plots showing variation of mean values at various mass flow rates.

To confirm the stationarity of the vibration signal, only one bundle configuration is focused and three different flow rates are selected (i.e., at 13.22 kg/s, 17.97 kg/s and 22.6 kg/s). For each test case, 30 records were obtained. Each record is 6.71 seconds long and contains 131,053 data points. The mean accelerations of the inlet and middle sensors for the three test conditions are shown in Fig. 4-22; the standard deviations are shown in Fig. 4-23.

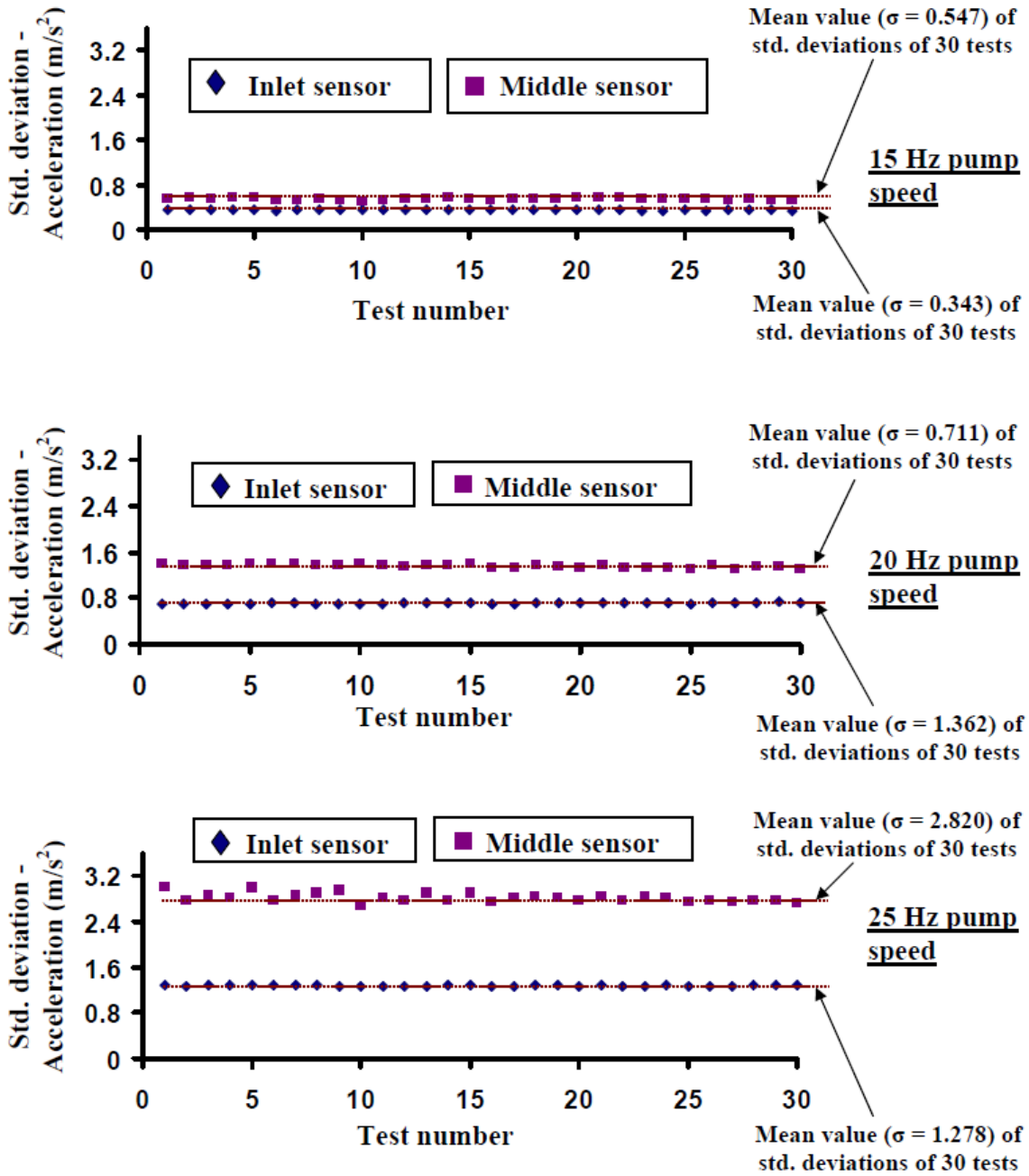


Fig. 4-23 Plots showing variation of standard deviations at various mass flow rates.

The mean value calculated from these 30 different measured means and standard deviations (or the population mean) are shown by a dotted line in each plot. It can be clearly seen that the mean and standard deviations are the same as the reference mean. The small differences

from the reference mean, as noticed in the plots, are caused by the random error incurred during the tests, which can hardly be avoided from a practical point of view.

4.2.4.2 Acceleration measurements

Altogether there are about 700 numbers of recorded measurements and so, it is hardly possible to present all time domain signals. Therefore, the time histories of the bundle vibration from the accelerometers are presented in Fig. 4-24 and Fig. 4-25 for the water mass flow rate of 17.97 kg/s setting only, which represents bundle response at the midway of the experimental range of 8.56 kg/s and 27.36 kg/s. The mean value is deducted from each of the measurements and only the fluctuation portion is produced to find the range of vibration. The mean and RMS values are given in Table 4-4 for single case as representative of other cases for easy understanding.

From Fig. 4-24, which represents the time histories of the fluctuations of the inlet sensor, the range of fluctuation is the largest for configuration (a). At this configuration, circular elements are not in their minimum overlapping; the ribs from two different bundles come side-to-side, making a large rectangular area of blockage and hence causing higher fluctuation. Configurations (A), (g), (i) and (B) show lowest fluctuating range, which can be explained from the fact that out of 11 possible configurations, only these four orientations provide larger flow area. In configurations (c), (f) and (h) larger fluctuation compared to those of (A), (g), (i) and (B) is noticed. At these configurations, one can notice that the flow area is actually reduced compared to other orientations, which leads the occurrence of larger fluctuations. The response of the middle sensor in Fig. 4-25 shows a higher fluctuation level for all configurations compared to those from the inlet sensor. This is understandable because the fuel elements at the middle tend to vibrate more in the fundamental bending mode.

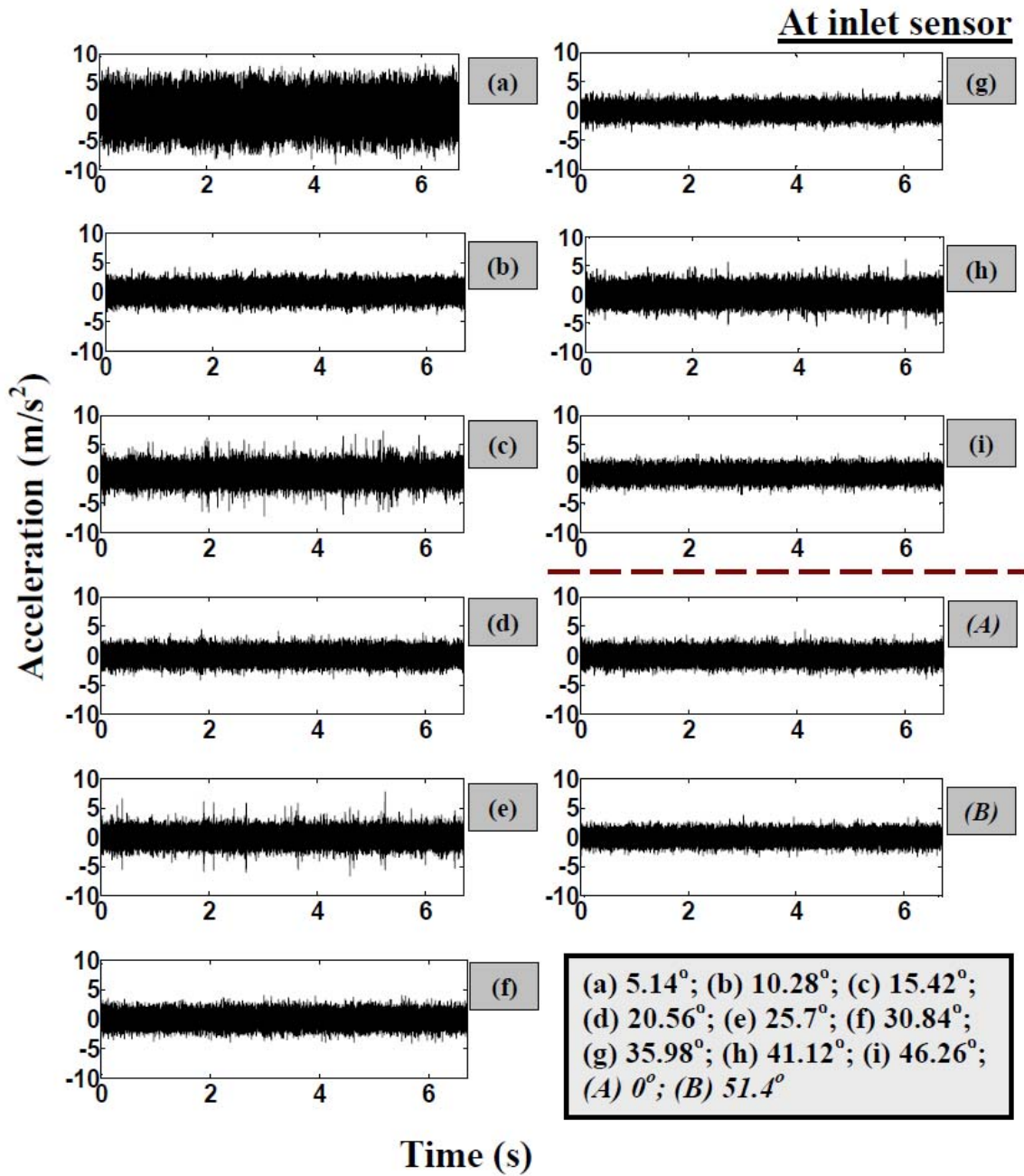


Fig. 4-24 Time histories of acceleration response for the inlet sensor at mass flow rate of 17.97 kg/s for different angular orientations.

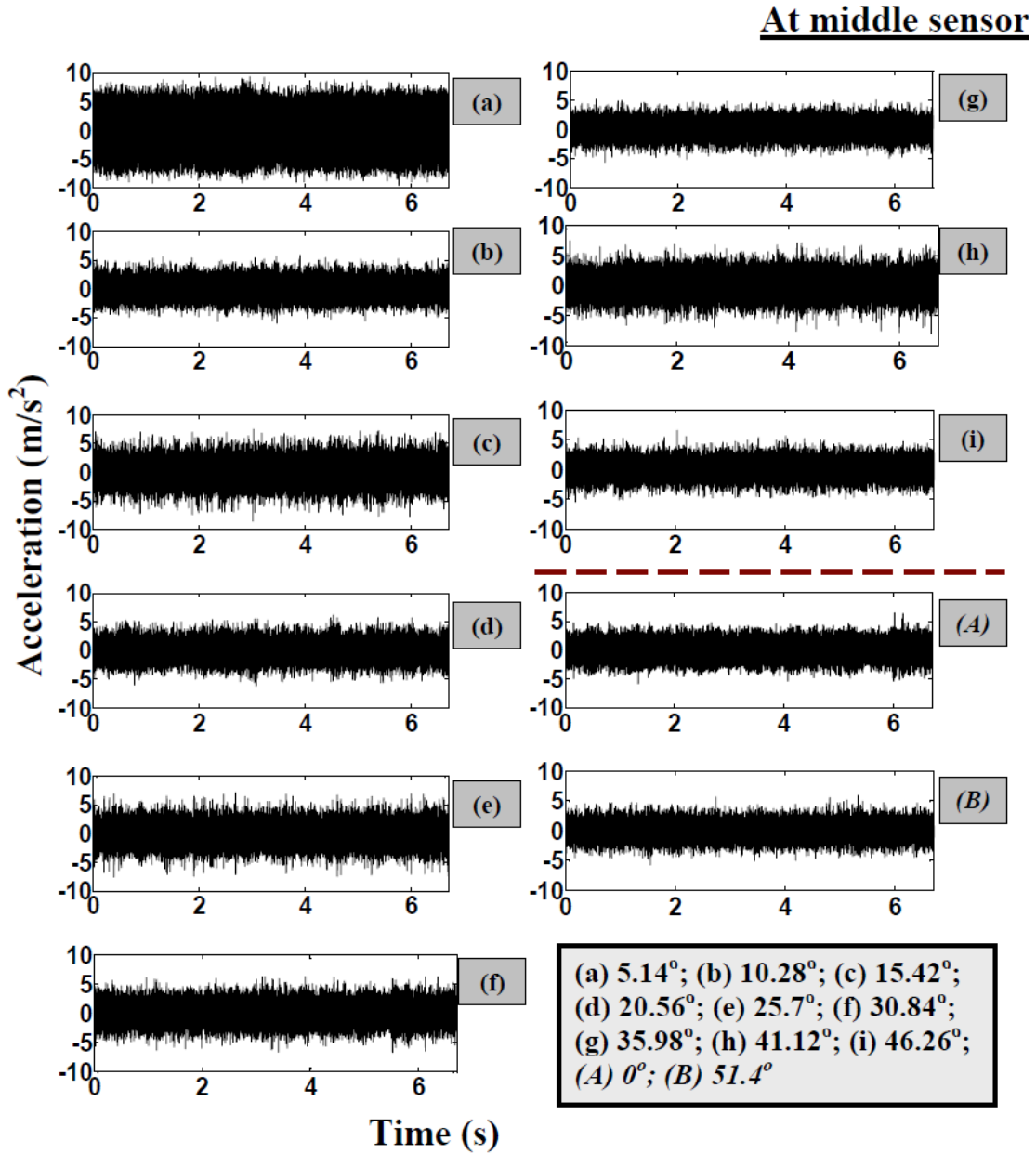


Fig. 4-25 Time histories of acceleration response for the middle sensor at mass flow rate of 17.97 kg/s for different angular orientations.

Table 4-4 The mean and RMS values of acceleration and displacement at mass flow rate of 17.97 kg/s for different angular orientations.

Misalignment angle (degree)	Inlet accelerometer		Middle accelerometer		Displacement sensor	
	Mean (m/s ²)	RMS (m/s ²)	Mean (m/s ²)	RMS (m/s ²)	Mean (mm)	RMS (mm)
0	29.56	0.89	27.94	1.29	0.165	0.0038
5.14	29.5	2.189	27.8	3	0.186	0.0044
10.28	29.51	0.96	28.0	1.4	0.22	0.0029
15.42	29.20	1.15	28.14	1.75	0.23	0.04
20.56	29.15	0.93	28.24	1.45	0.32	0.0039
25.7	28.64	0.998	29.60	1.62	0.28	0.0037
30.84	28.75	0.94	28.76	1.52	0.30	0.004
35.98	28.75	0.83	28.05	1.29	0.33	0.0034
41.12	28.93	1.05	28.47	1.63	0.31	0.0039
46.26	28.76	0.85	28.78	1.32	0.34	0.0037
51.4	28.64	0.8	28.69	1.28	0.35	0.0036

4.2.4.3 Displacement measurements

The time histories of the displacement sensor measurement are presented in Fig. 4-26 for the mass flow rate of 17.97 kg/s. In these plots, the mean value is deducted from each of the measurements and only the fluctuations with respect to the mean are shown. For configuration (a) and (f), large fluctuations are observed. This is because, outer and middle ring elements are overlapping in the same manner creating similar blockage to the flow path. Exceptions are noticed for inner ring elements. For the other configurations, fluctuation range is much smaller.

It is to be noted here, that the RMS values for both acceleration and displacement time histories are falling well outside the given range of error of the measuring sensors and thus the acceptability of the measurement is justified.

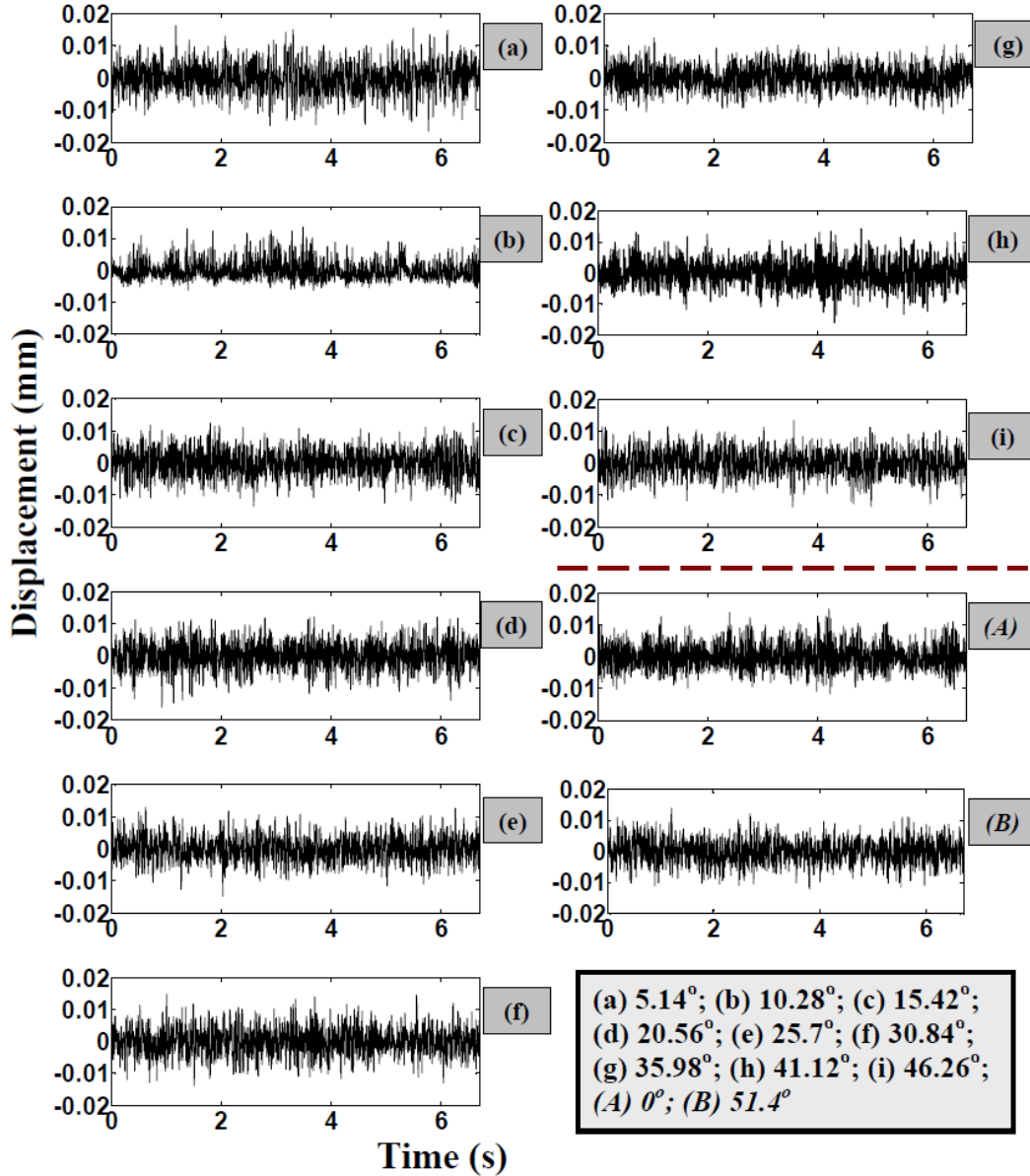


Fig. 4-26 Time histories of displacement response for the inlet sensor at mass flow rate of 17.97 kg/s for different angular orientations.

4.2.4.4 Acceleration PSDs

In the current study, a total of 11 different bundle misalignment configurations are investigated. For each configuration, measurements are recorded for 21 different flow rates, making the total number of measurements to 693 with 231 for each sensor. However, due to space limitations, the PSDs are shown only for mass flow rate of 17.97 kg/s setting as a representative of all cases. The PSD plots are shifted upward in order to consolidate them in one figure. The plots are limited to 5 Hz and 500 Hz frequency, which is the range of interest for the bundle vibration in the present study.

The PSDs of the acceleration response from the two sensors are shown in Fig. 4-27 and Fig. 4-28. In Fig. 4-27, which relates to the inlet sensor, the shaft rotating frequency, the blade passing frequencies and other dominant frequencies are all seen noticeably. The dominant frequencies, except the blade passing frequency, are found to be shifting at different misalignment configurations with no specific trend. For the middle sensor at the same mass flow rate of 17.97 kg/s setting, the dominant frequencies (Fig. 4-28), except the blade passing frequencies, are not prominent compared to that of Fig. 4-27; but their occurrence varies with the misalignment angle.

4.2.4.5 Displacement PSDs

In Fig. 4-29, PSD plots for the displacement sensor at mass flow rate of 17.97 kg/s is presented. From this figure, a few other dominant frequencies in addition to the pump blade passing frequency are noticed. The 25 Hz frequency is observed to be shifting between 25 Hz and 30 Hz at various bundle misalignment combinations; this demonstrates that the frequency of the displacement response vary with the misalignment angles.

From the PSDs of the acceleration and the displacement response, it is noticed that the frequency of bundle motion is sensitive to the misalignment angle. To date, this is an important observation with respect to CANDU fuel bundle motion. However, it is of more relevance to find out, if at all, the effect of angular misalignment on the bundle lateral response, as discussed in details in the following sub-section.

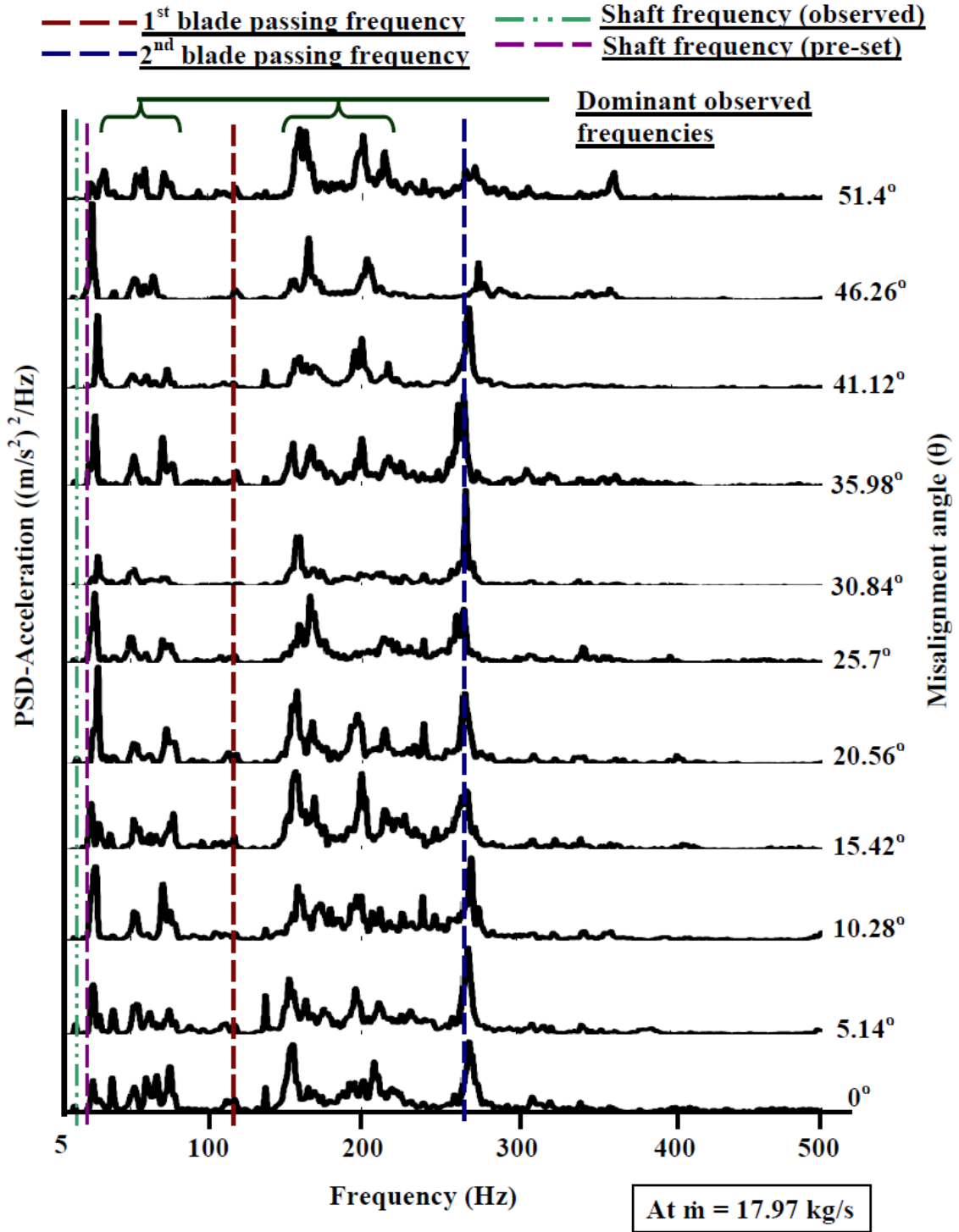


Fig. 4-27 PSDs of acceleration response for the inlet sensor at mass flow rate of 17.97 kg/s for different angular orientations.

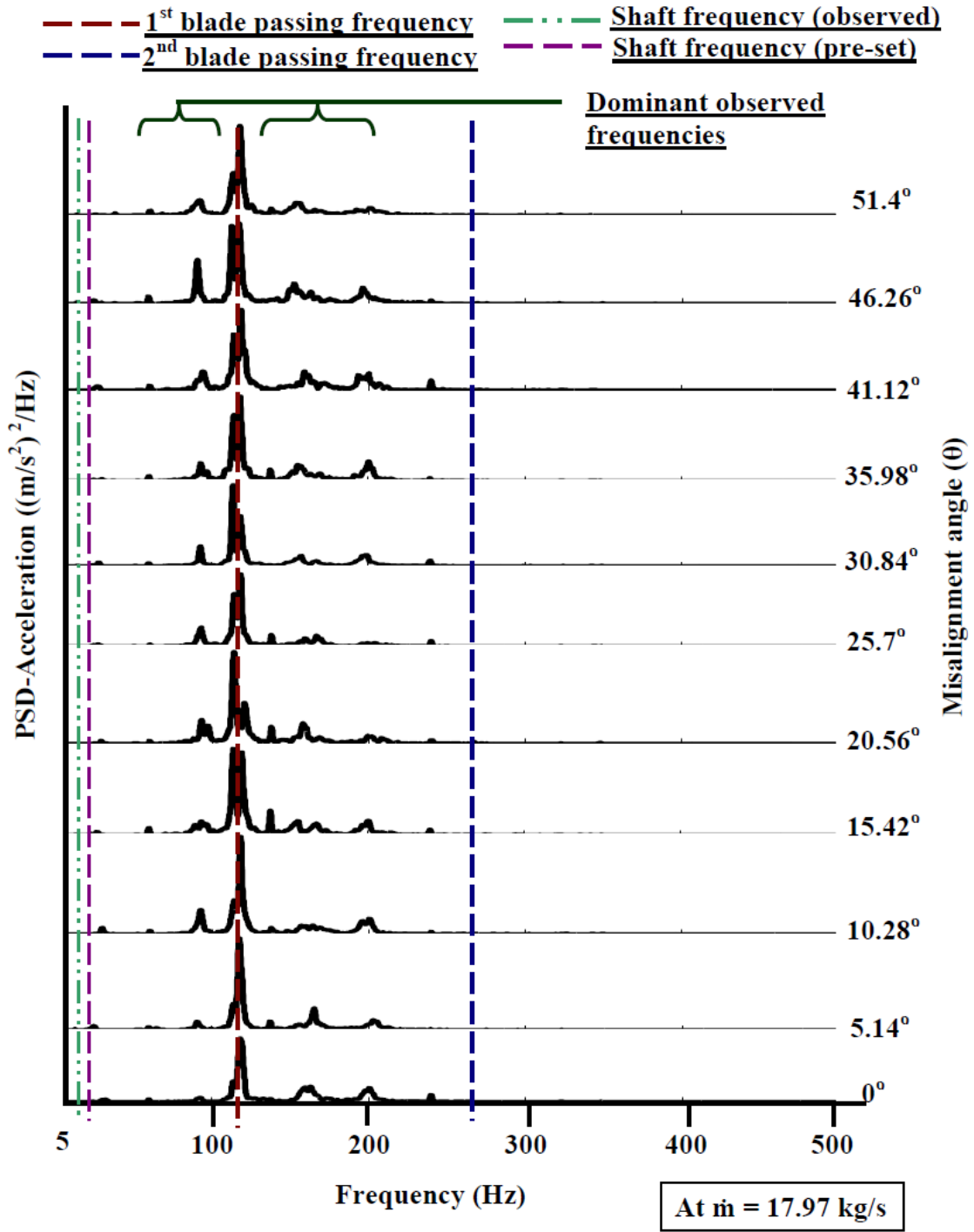


Fig. 4-28 PSDs of acceleration response for the middle sensor at mass flow rate of 17.97 kg/s for different angular orientations.

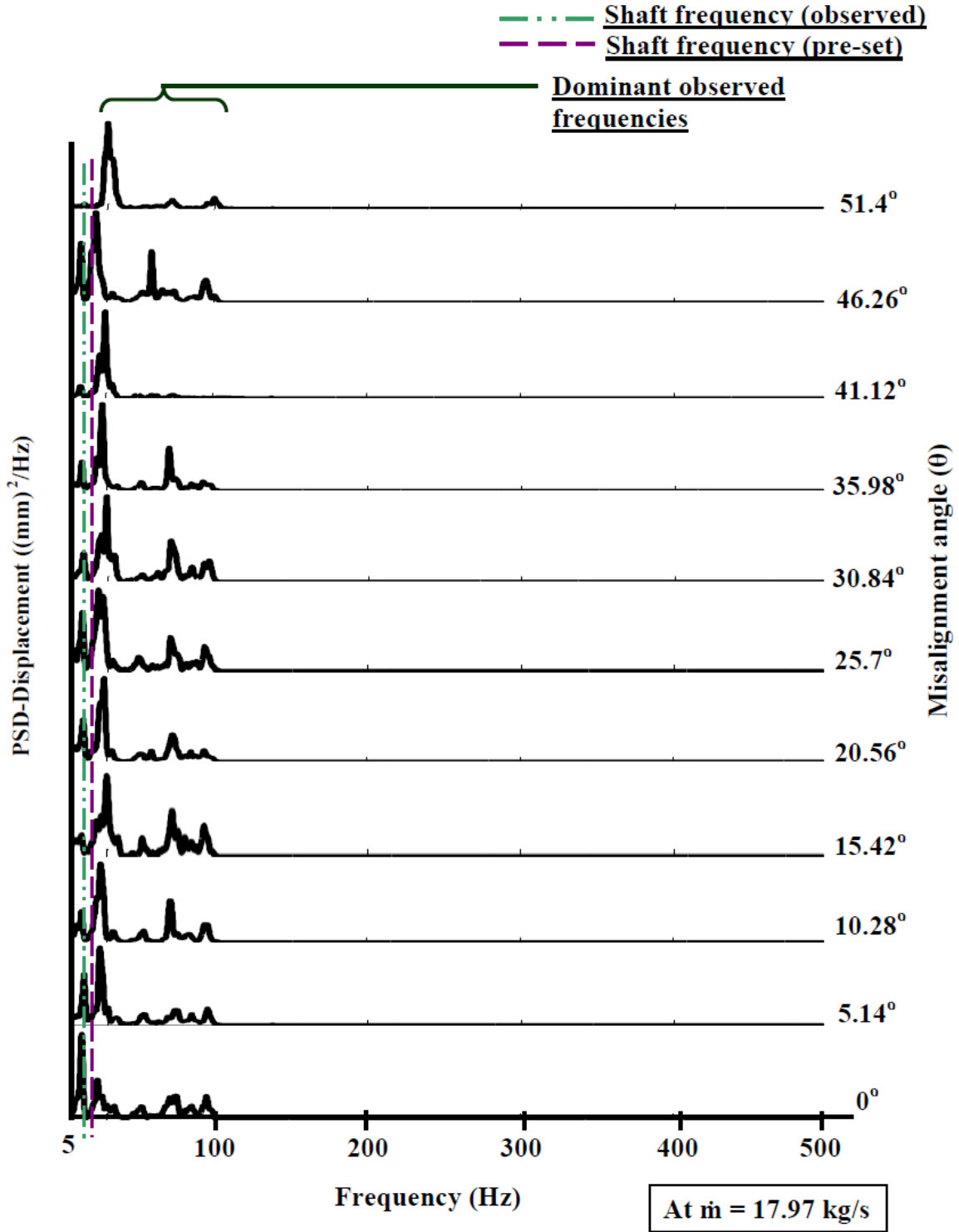
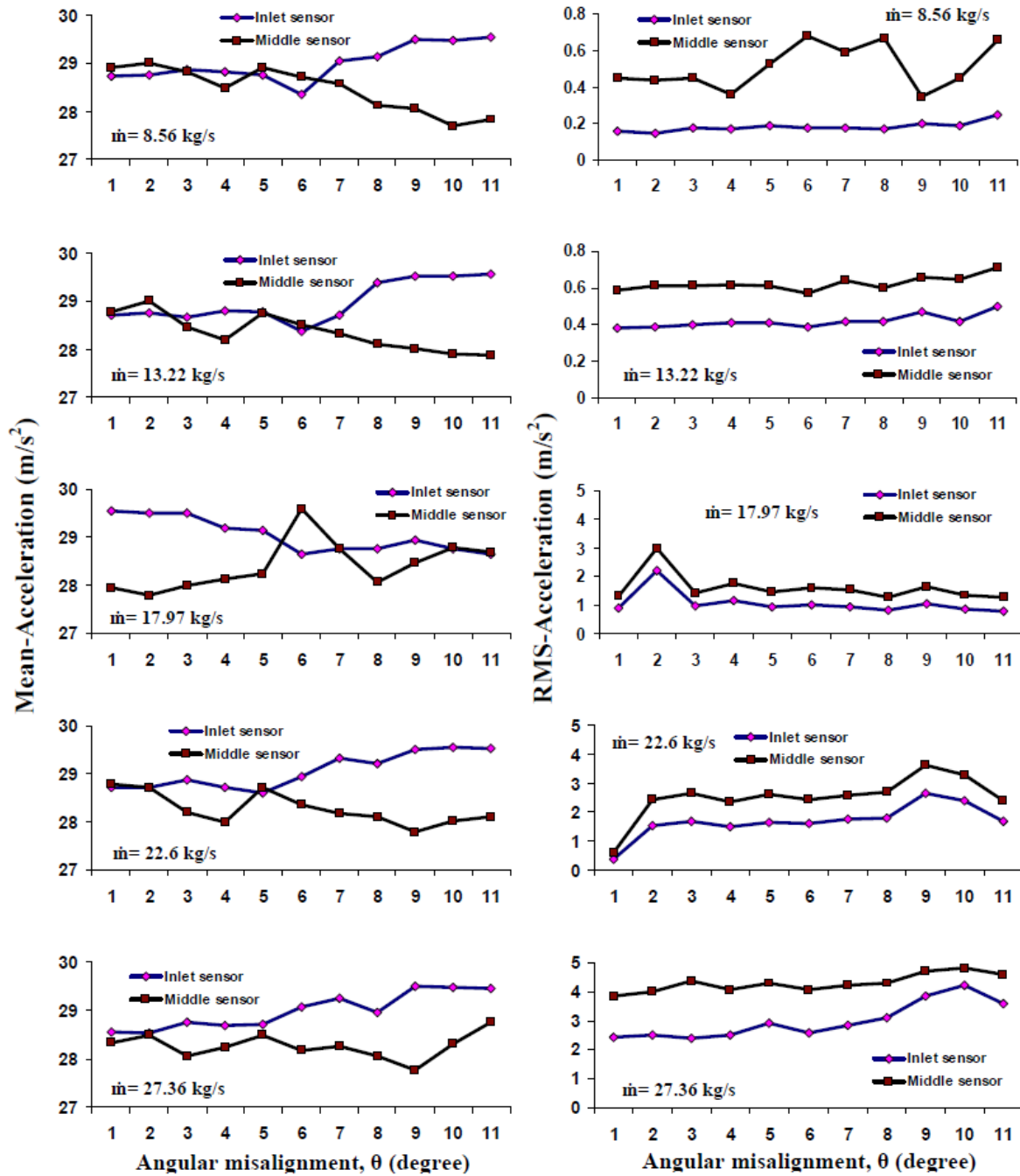


Fig. 4-29 PSDs of displacement response at mass flow rate of 17.97 kg/s for different angular orientations.

4.2.4.6 *Effect of Angular Misalignment on Bundle Acceleration response*

In Fig. 4-30, the plots on the left side refer to the mean values and those on the right side refer to the RMS values of the bundle acceleration response for different misalignment angles. The mass flow rate for each case is mentioned in the respective plots. It is very clearly visible from the mean-acceleration plots that the mean values change considerably with respect to the misalignment angle. The variations on mean values are found to be occurring at misalignment angle of 15.42° , 20.56° , 25.7° , 35.98° and 41.12° , for the middle sensor. For the inlet sensor, the larger mean variations are observed to be occurring at misalignment angle of 20.56° , 25.7° and 35.98° . It is thus reasonable to mention that the change in misalignment angles affect the mean bundle response.

For the RMS values, which are better representation of vibration/fluctuation, the first two plots are shown with different Y-axis value due to very small change in the fluctuations at the lower mass flow rates. At mass flow rate of 8.56 kg/s and 13.22 kg/s, the fluctuations of the inlet and the middle sensors appear with very little change, except for the middle sensor at the 8.56 kg/s flow rate, where RMS values change significantly at misalignment angle of 15.42° , 25.7° , 35.98° and 41.12° . The RMS values, at higher mass flow rates, exhibit distinguishable variation with respect to the change in the misalignment angle along with considerably higher fluctuations. The occurrence of the large RMS amplitude at a mass flow rate of 17.97 kg/s is already explained in sub-section 4.2.4.2.1. Also, interestingly but quite logically, for the mass flow rate of 22.6 kg/s and 27.36 kg/s cases, the fluctuations show a trend of approaching lower values at the misalignment angle 0° and 51.4° , which represent two consecutive fully aligned configurations, compared to the other misalignment angles. From these plots of both mean and the RMS values, it can very distinctively be seen that bundle-to-bundle misalignment configurations indeed affect the bundle lateral motion.



' θ ' values: (1) 0°; (2) 5.14°; (3) 10.28°; (4) 15.42°; (5) 20.56°; (6) 25.7°; (7) 30.84°; (8) 35.98°; (9) 41.12°; (10) 46.26°; (11) 51.4°

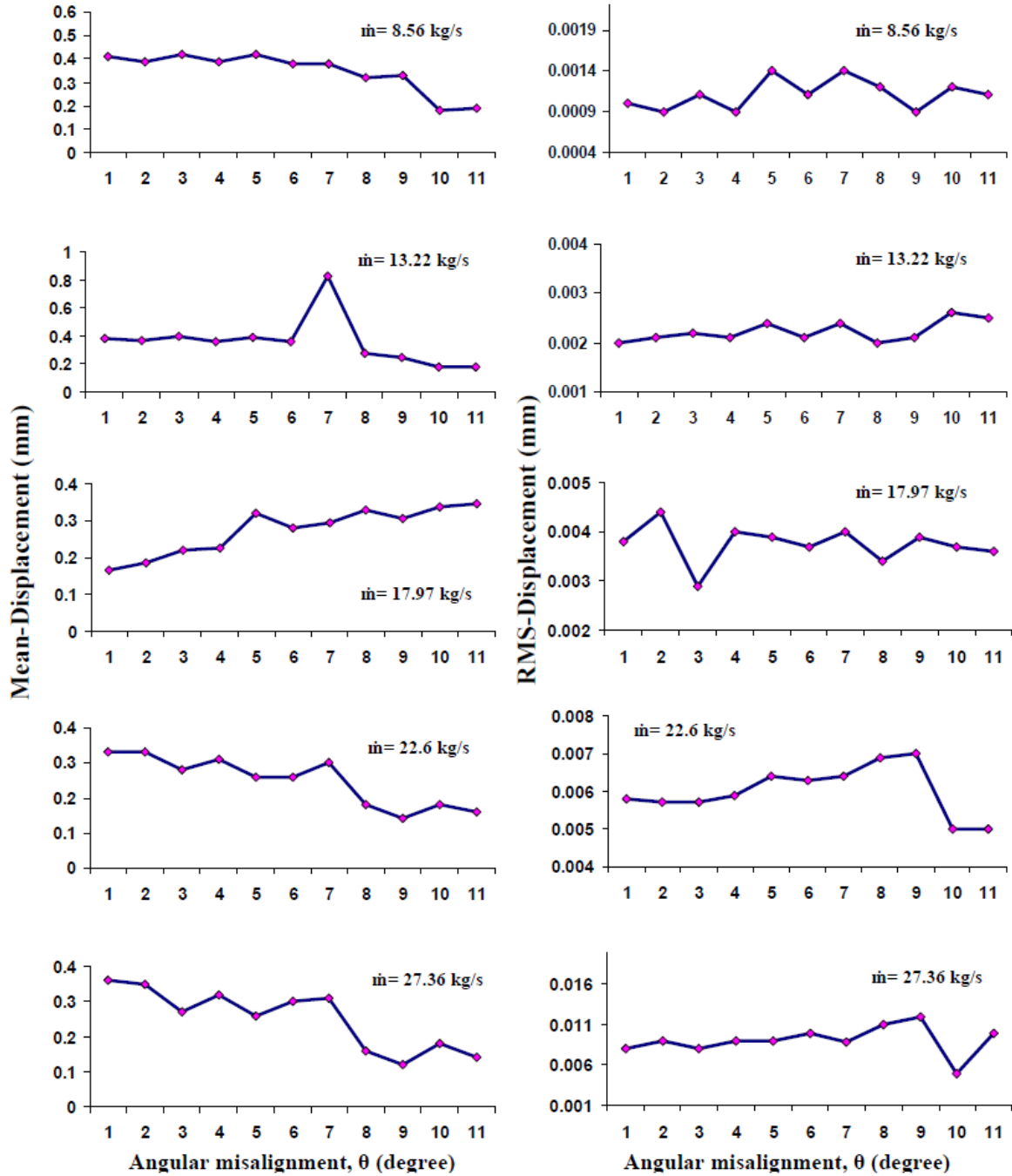
(\dot{m} = mass flow rate of water in kg/s)

Fig. 4-30 Mean and RMS values of acceleration response at various angular orientations for different mass flow rates.

4.2.4.7 *Effect of Angular Misalignment on Bundle Displacement response*

The mean and RMS values corresponding to displacement response are plotted in Fig. 4-31 for different flow rates at all selected misalignment combinations. The values in the plots represent the actual bundle lateral movement inside the PVC pipe of the testing loop. Like Fig. 4-30, in this figure also, the plots in the left and the right side represent the mean and the RMS displacement values, respectively. Except for the mass flow rate of 17.97 kg/s, all other plots show a downward trend. The variation in the mean values is noticed to be small in case 8.56 kg/s and 17.97 kg/s flow rate settings and is large in the cases of 13.22 kg/s, 22.6 kg/s and 27.36 kg/s flow rate settings. Also, the combination of mass flow rate of 13.22 kg/s and a misalignment angle of 30.84° is observed to produce significant increase in the mean displacement, nearly up to 0.8 mm.

Like the acceleration RMS plots, the RMS values of displacement measurements also show reasonable amount of fluctuation for different flow conditions at different misalignment angles. The large fluctuations are noticed mainly at misalignment angle of 10.28° , 41.12° and 46.16° . It may appear from the RMS-displacement plots that, although the values are well outside the error band of the sensor, but still too small (between $1\ \mu\text{m}$ and $16\ \mu\text{m}$) to produce considerable amount of fluctuation which could be harmful for the tube containing the bundles. However, it is to be noted here that inside the pressure tube, the actual CANDU fuel bundle has very limited space to move, about 1.5 mm at the top (max). The researches carried out in the past showed that the recorded RMS vibration amplitude for the bundle remains within $10\ \mu\text{m}$ (Pettigrew, 1993) and the gross bundle motion in the pressure tube is as low as $25\ \mu\text{m}$ (Norsworthy et al., 1994). Moreover, fretting is a phenomenon with very small amplitude vibration capable of causing potential damage in long term application. Therefore, the amount fluctuations recorded from the displacement measurement due to the different misalignment configurations are of practical significance to CANDU fuel bundle application concerning the pressure tube fretting induced wear.



' θ ' values:

(1) 0° ; (2) 5.14° ; (3) 10.28° ; (4) 15.42° ; (5) 20.56° ; (6) 25.7° ; (7) 30.84° ; (8) 35.98° ; (9) 41.12° ;
 (10) 46.26° ; (11) 51.4°

(\dot{m} = mass flow rate of water in kg/s)

Fig. 4-31 Mean and RMS values of displacement response at various angular orientations for different mass flow rates.

4.2.4.8 Effect of Flow Velocity on Bundle Response at Various Angular Misalignment

Since the present experiment is conducted at various flow velocities, it would be better to provide information regarding the effect of flow velocities on the bundle response at different misalignment angles. This is described in this sub-section with the help of Fig. 4-32. In this figure, the acceleration and the displacement RMS values of the recorded measurements are plotted for four randomly selected misalignment angles from the 11 pre-defined combinations at different bundle flow velocities ranging from 2.4 m/s to 7.7 m/s.

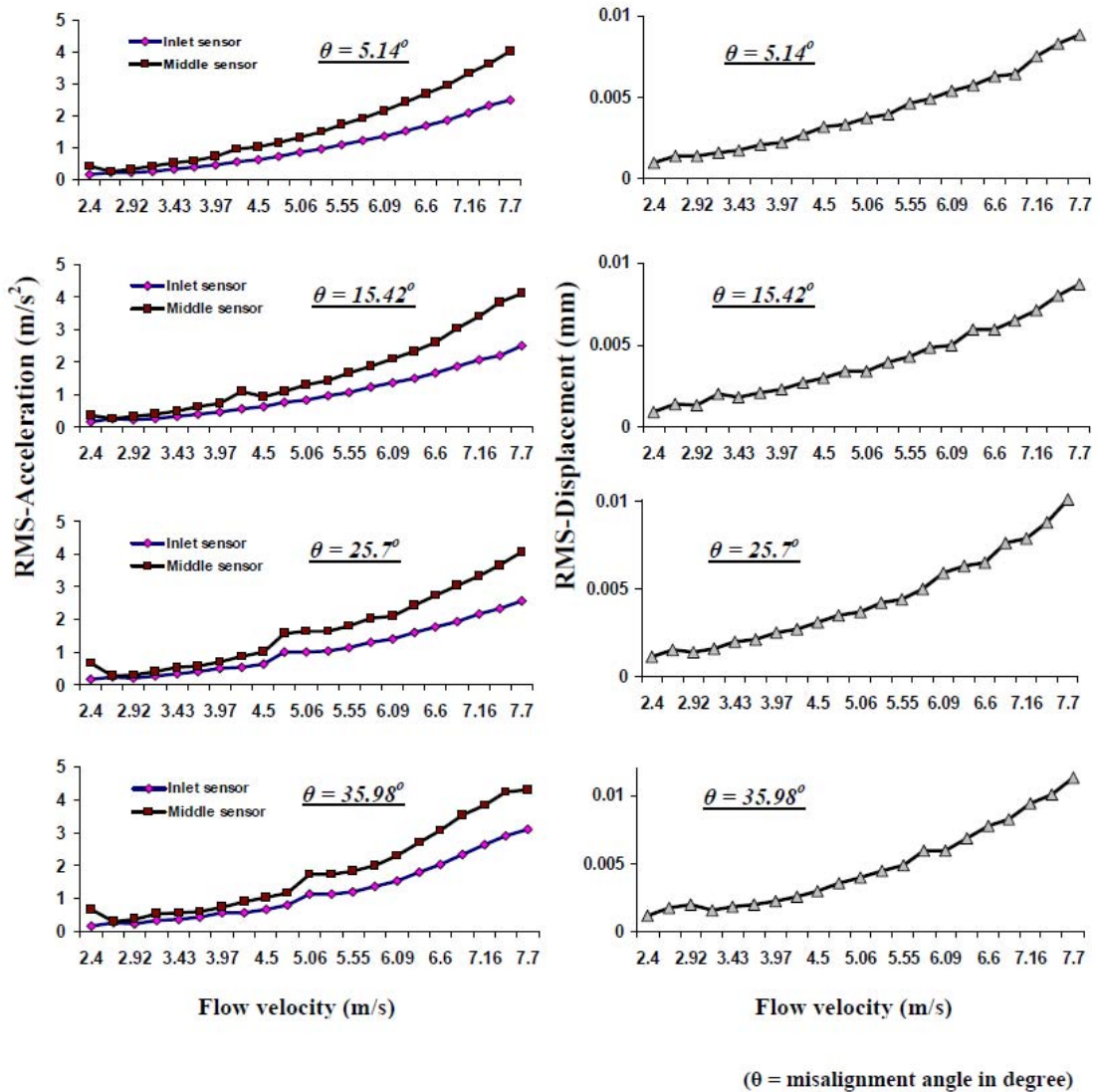


Fig. 4-32 RMS values of acceleration and displacement response at various mass flow rates for different angular orientations.

From all eight plots it is very clearly seen that the RMS values increase with the increase of the flow velocity, which is well expected. Except for few cases, which are minor, the change in the RMS amplitude with respect to the flow velocity is smooth and almost consistent for each misalignment angle condition.

4.2.5 Findings from the experimental work

Experiments are carried out to investigate flow-induced vibration of a two simulated CANDU fuel bundle string with angular misalignment. The experimental data obtained for 11 different bundle orientations reveal that there exist some configurations where lateral bundle vibration levels are very high. Shift in dominating frequency as a result of bundle misalignment is observed. The RMS values of the acceleration and the displacement response demonstrate that the angular misalignment influences the bundle lateral vibration significantly. For CANDU type reactors, where bundle orientations are not controlled, findings from the current experimental study should be very useful to nuclear fuel design engineers and scientists.

4.3 Summary

The bundle-to-bundle angular misalignment is found to influence both the lateral fluid excitations and the lateral bundle motion. Both numerical and experimental studies reveal that there exist some misalignment combinations, at which the bundle experiences much higher lateral fluid forces and vibrates with considerably higher amplitude. This is one of the most significant findings to date in the field of flow-induced vibrations of CANDU fuel bundle structure.

CHAPTER 5: CONCLUSION

5.1 Conclusion

Comprehensive computational model for a fuel channel filled with 12 bundles has been developed in the present study to get an insight of the flow features for the whole bundle string, and also to quantify the effect of bundle angular misalignment on the transverse fluid forces. The fluid excitations are found to be low when all bundles are fully aligned with each other. Excitations became higher with all bundles being misaligned by an angle of 5° . But, in the presence of only two misaligned interfaces in the whole bundle string, fluid excitations reached their highest values (out of the three models) mainly on the neighboring bundles of the misaligned interfaces. The mean lateral fluid forces increased by an order of magnitude, and their RMS values rose about 3 to 4 times at some misalignment configurations compared to fully aligned situation. The bundle subchannel flow inside the fuel channel is found to be very much coherent from the cross-correlation plots, and the coherence is weakened with the introduction of the misaligned interfaces of adjacent bundles. The PSD plots of the fluid forces revealed that the fluid excitation frequencies change with bundle misalignment arrangements – making the bundles more susceptible to the different frequencies of fluid excitations.

To find out some critical angular combinations of misalignment arrangement, a detailed study on the bundle angular misalignment is done on a two-bundle string with a much finer increment of angular misalignment. Results show significant variation in the mean lateral fluid force at different misaligned configurations, and the variation is persistent with the misalignment angle. The fluctuation (or RMS) of these forces is found to increase about 3 times in the case of 35° misalignment and varies distinctly with misalignment combinations. Experimental investigations on the two simulated CANDU fuel bundles show that bundle lateral movement varies with the change in the angular misalignment. PSDs computed from the measured bundle response show that dominant frequencies occur without any specific trend and they are found to shift with the change in the misalignment angle. Therefore, in order to assess proper fluid forces on the fuel bundles and to measure

bundle transverse motion due to the coolant flow, bundle-to-bundle angular misalignment should be considered – so that the mechanism of flow-induced vibration in fuel bundle structure is understood well.

5.2 Major Accomplishments

The main accomplishments from the current research work can be summarized as:

- Developed a comprehensive computational fluid dynamics model for a fuel channel filled with a string of 12-bundles and obtained solutions using large eddy simulation for the first time – a significant achievement to date.
- Discovered that the fully aligned fuel bundles produce minimal lateral fluid excitations and misaligned fuel bundles produce large amplitude excitations.
- Predicted the lateral fluid excitations for individual bundles in a string of 12 bundles at different angular misalignment.
- Observed that one of the major sources of bundle lateral vibration is the coherent nature of the flow among the multiple bundles inside the fuel channel exhibiting fluid excitations of frequencies spread over a wide band in the power spectra.
- Examined lateral fluid excitations at various angular misalignment combinations for a short bundle string with finer increment of misalignment angle and noted some critical bundle positions with higher fluid forces.
- Found good correlation of flow among different bundles and the coherence is reduced with the presence of the misaligned interfaces.
- Experimentally investigated that bundle lateral motion is higher in the case of misaligned bundle interfaces and lower in the fully aligned case.

5.3 Significance of this research

This research presents some new results from LES simulations of highly turbulent coolant flow in a string of CANDU fuel bundles with a focus on the effect of the angular

misalignment of the individual fuel bundles. One of the the main merits of the present work is the application of high-performance computing to a complex, large-scale practical problem of considerable relevance to the operation of CANDU reactors. An analysis of a complete fuel channel of a nuclear reactor using LES is at the forefront of current research worldwide. The present study contributes to enhancing the state-of-the-art, by a successful application of the CFD technique to a particular problem of the CANDU design.

The current study will help evaluate the lateral fluid excitations on individual fuel bundles in a fuel channel, and will also provide better understanding and information of the influence of the bundle angular misalignment on the fluid forces and the bundle response. Also, from the results of the present research, it can be mentioned that if by any means the bundle angular positions are locked with respect to the neighboring bundles, the effective lateral fluid excitations can be reduced considerably. Therefore, this research could benefit the nuclear industry, in terms of gaining in-depth knowledge on the flow mechanism and the flow-induced vibration of the fuel bundles for a full length fuel channel.

5.4 Future work

Firstly, the real fluid-structure interaction phenomemon can be explored and solved for the fuel bundle study using the user defined function (UDF) in the FLUENT. A model can be created and tested starting with a single beam subjected to axial fluid flow. Upon finding reasonable meshing factors for the dynamic meshing domain from the simpler model, another large scale model can be developed. The demand of high computational resources can be optimized by having an efficient parallel processing scheme for the solution complying the UDF.

Secondly, in past studies on the fuel bundle structure subjected to axial flow, while calculating the critical flow velocity for the bundle, only one bundle has been considered at the most. This is highly under-estimating the fact that inside the fuel channel due to the hydraulic drag of the coolant, bundles are in contact with their neighboring ones almost always, and thus these bundles behave more like a string than an independent separate bundle. Therefore, the critical flow velocity calculated for a single bundle can reasonably differ from that of a whole string of bundles. So, in such a situation, if the critical flow

velocity based on the complete bundle string is falling on the vicinity of the natural frequency of the bundle string, fluid-elastic instability is bound to happen, and the whole string will start vibrating. This will cause severe damage to the pressure tube. So, it is very important to calculate the proper critical flow velocity for the whole string of bundles in order to see whether the operating flow velocity in the actual reactor is falling near the calculated threshold value. This is has not yet been evaluated to date, and if ascertainable, can be a significant milestone in understanding the mechanism(s) of fuel bundle vibration in CANDU reactors.

APPENDIX

A1. Matlab script for generating PSDs of x- and y-forces

```
clear;clc;
%-----%
% Read the data

basefile = 'Directory of the data file';
%*** Complete File Name ***
expression = [basefile,'Fx_hst','.DAT'];
% expression = [basefile,'Fy_hst','.DAT'];

data = load(expression);
[m,n] = size(data); %m is # rows %n is # cols
%-----%
% Sampling rate
Ts=data(2,1)-data(1,1);
Fs=1/Ts;
% -----%
% Data cutting time
TStart=data(1,1);
TEnd=data(end,1);
TLength=TEnd-TStart;
NData=4000;
%-----%
time=data(1:m,1); % (s)
Output10=data(1:m,2)'; % (BD-10)
Output11=data(1:m,3)'; % (BD-11)
Output12=data(1:m,4)'; % (BD-12)
Output1=data(1:m,5)'; % (BD-1)
Output2=data(1:m,6)'; % (BD-2)
Output3=data(1:m,7)'; % (BD-3)
Output4=data(1:m,8)'; % (BD-4)
Output5=data(1:m,9)'; % (BD-5)
Output6=data(1:m,10)'; % (BD-6)
Output7=data(1:m,11)'; % (BD-7)
Output8=data(1:m,12)'; % (BD-8)
Output9=data(1:m,13)'; % (BD-9)
%-----%
nfft=NData;
Resolution=Fs/nfft; % freq. bandwidth (Hz)
%-----%
% Deducting the mean to get the fluctuations
%-----%
mean1=sum(Output1)/nfft;
zm1=Output1-mean1;
mean2=sum(Output2)/nfft;
zm2=Output2-mean2;
mean3=sum(Output3)/nfft;
zm3=Output3-mean3;
mean4=sum(Output4)/nfft;
zm4=Output4-mean4;
mean5=sum(Output5)/nfft;
zm5=Output5-mean5;
mean6=sum(Output6)/nfft;
```

```

zm6=Output6-mean6;
mean7=sum(Output7)/nfft;
zm7=Output7-mean7;
mean8=sum(Output8)/nfft;
zm8=Output8-mean8;
mean9=sum(Output9)/nfft;
zm9=Output9-mean9;
mean10=sum(Output10)/nfft;
zm10=Output10-mean10;
mean11=sum(Output11)/nfft;
zm11=Output11-mean11;
mean12=sum(Output12)/nfft;
zm12=Output12-mean12;

%-----
% PSD calculation of x- and y-forces
%-----
[P11 F]=cpsd(zm1,zm1,gausswin(1000),[],nfft,Fs);
[P22 F]=cpsd(zm2,zm2,gausswin(1000),[],nfft,Fs);
[P33 F]=cpsd(zm3,zm3,gausswin(1000),[],nfft,Fs);
[P44 F]=cpsd(zm4,zm4,gausswin(100),[],nfft,Fs);
[P55 F]=cpsd(zm5,zm5,gausswin(1000),[],nfft,Fs);
[P66 F]=cpsd(zm6,zm6,gausswin(1000),[],nfft,Fs);
[P77 F]=cpsd(zm7,zm7,gausswin(1000),[],nfft,Fs);
[P88 F]=cpsd(zm8,zm8,gausswin(1000),[],nfft,Fs);
[P99 F]=cpsd(zm9,zm9,gausswin(1000),[],nfft,Fs);
[P1010 F]=cpsd(zm10,zm10,gausswin(1000),[],nfft,Fs);
[P1111 F]=cpsd(zm11,zm11,gausswin(1000),[],nfft,Fs);
[P1212 F]=cpsd(zm12,zm12,gausswin(1000),[],nfft,Fs);

%-----
f =Fs/2* linspace(0,1,nfft/2)';
Bw=Fs/nfft;
%-----
%% Plotting
% Plotting parameters
nfc=1100/Resolution;
% % plot the acce.
% hold on
figure(1);
subplot(2,1,1);
loglog(f(1:nfc),(P11(1:nfc)),'-k','Linewidth',6);
axis([0,500, 0, 10]);
% grid on
set(gca,'YTick',[1e-10 1e-5 1], 'XTick',[0 100 200 300 500])

subplot(2,1,2);
loglog(f(1:nfc),(P22(1:nfc)),'-k','Linewidth',6);
axis([0,500, 0, 10]);
% grid on
set(gca,'YTick',[1e-10 1e-5 1], 'XTick',[0 100 200 300 500])

figure(2);
subplot(2,1,1);
loglog(f(1:nfc),(P33(1:nfc)),'-k','Linewidth',6);
axis([0,500, 0, 10]);

```

```

% grid on
set(gca, 'YTick',[1e-10 1e-5 1], 'XTick',[0 100 200 300 500])

subplot(2,1,2);
loglog(f(1:nfc),(P44(1:nfc)),'-k','Linewidth',6);
axis([0,500, 0, 10]);
% grid on
set(gca, 'YTick',[1e-10 1e-5 1], 'XTick',[0 100 200 300 500])

.
.
.
%-----
% Similar repeated command for figure 3 to 5.
%-----
.
.
.

figure(6);
subplot(2,1,1);
loglog(f(1:nfc),(P1111(1:nfc)),'-k','Linewidth',6);
axis([0,500, 0, 10]);
% grid on
set(gca, 'YTick',[1e-10 1e-5 1], 'XTick',[0 100 200 300 500])

subplot(2,1,2);
loglog(f(1:nfc),(P1212(1:nfc)),'-k','Linewidth',6);
axis([0,500, 0, 10]);
% grid on
set(gca, 'YTick',[1e-10 1e-5 1], 'XTick',[0 100 200 300 500])

% -----
% end

```

A2. Matlab script for generating cross-correlation coefficient of flow parameters in time domain

```

clear;clc;
%-----
% Read the data

basefile = 'Directory of the data file';
for i = 1
%*** Complete File Name ***
%   expression = [basefile,'xcorr_ux_',num2str(i),'.OUT'];
%   expression = [basefile,'xcorr_Fx_',num2str(i),'.dat'];
%   expression = [basefile,'xcorr_Fy_',num2str(i),'.dat'];

%*** Load The Data ***
data = load(expression);
[m,n] = size(data);           %m is # rows %n is # cols
end
%-----

```

```

% Sampling rate
Ts=(data(2,1)-data(1,1));
Fs=1/Ts;
% -----
% Data cutting time
TStart=(data(1,1));
TEnd=(data(end,1));
TLength=TEnd-TStart;
NData=4000;
%-----
time=data(1:m,1); % (s)
Output10=data(1:m,2)'; % (full_bundle)
Output11=data(1:m,3)'; % (full_bundle)
Output12=data(1:m,4)'; % (full_bundle)
Output1=data(1:m,5)'; % (full_bundle)
Output2=data(1:m,6)'; % (full_bundle)
Output3=data(1:m,7)'; % (full_bundle)
Output4=data(1:m,8)'; % (full_bundle)
Output5=data(1:m,9)'; % (full_bundle)
Output6=data(1:m,10)'; % (full_bundle)
Output7=data(1:m,11)'; % (full_bundle)
Output8=data(1:m,12)'; % (full_bundle)
Output9=data(1:m,13)'; % (full_bundle)
%-----
nfft=NData;
Resolution=Fs/nfft; % freq. bandwidth (Hz)
%-----
% Deducting the mean to get the fluctuations
%-----
mean1=sum(Output1)/nfft;
zm1=(Output1-mean1);
mean2=sum(Output2)/nfft;
zm2=(Output2-mean2);
mean3=sum(Output3)/nfft;
zm3=(Output3-mean3);
mean4=sum(Output4)/nfft;
zm4=(Output4-mean4);
mean5=sum(Output5)/nfft;
zm5=(Output5-mean5);
mean6=sum(Output6)/nfft;
zm6=(Output6-mean6);
mean7=sum(Output7)/nfft;
zm7=(Output7-mean7);
mean8=sum(Output8)/nfft;
zm8=(Output8-mean8);
mean9=sum(Output9)/nfft;
zm9=(Output9-mean9);
mean10=sum(Output10)/nfft;
zm10=(Output10-mean10);
mean11=sum(Output11)/nfft;
zm11=(Output11-mean11);
mean12=sum(Output12)/nfft;
zm12=(Output12-mean12);
%-----
% Cross-correlation
k = (1:(2*length(Output1)-1));
BD1BD1 = xcorr(zm1, zm1, 'coeff');

```

```

BD1BD2 = xcorr(zm1,zm2,'coeff');
BD1BD3 = xcorr(zm1,zm3,'coeff');
BD1BD4 = xcorr(zm1,zm4,'coeff');
BD1BD5 = xcorr(zm1,zm5,'coeff');
BD1BD6 = xcorr(zm1,zm6,'coeff');
BD1BD7 = xcorr(zm1,zm7,'coeff');
BD1BD8 = xcorr(zm1,zm8,'coeff');
BD1BD9 = xcorr(zm1,zm9,'coeff');
BD1BD10 = xcorr(zm1,zm10,'coeff');
BD1BD11 = xcorr(zm1,zm11,'coeff');
BD1BD12 = xcorr(zm1,zm12,'coeff');

```

```

BD1BD6 = xcorr(zm1,zm6,'coeff');
BD2BD6 = xcorr(zm2,zm6,'coeff');
BD3BD6 = xcorr(zm3,zm6,'coeff');
BD4BD6 = xcorr(zm4,zm6,'coeff');
BD5BD6 = xcorr(zm5,zm6,'coeff');
BD6BD6 = xcorr(zm6,zm6,'coeff');
BD6BD7 = xcorr(zm6,zm7,'coeff');
BD6BD8 = xcorr(zm6,zm8,'coeff');
BD6BD9 = xcorr(zm6,zm9,'coeff');
BD6BD10 = xcorr(zm6,zm10,'coeff');
BD6BD11 = xcorr(zm6,zm11,'coeff');
BD6BD12 = xcorr(zm6,zm12,'coeff');

```

```

BD1BD2 = xcorr(zm1,zm2,'coeff');
BD2BD3 = xcorr(zm2,zm3,'coeff');
BD3BD4 = xcorr(zm3,zm4,'coeff');
BD4BD5 = xcorr(zm4,zm5,'coeff');
BD5BD6 = xcorr(zm5,zm6,'coeff');
BD6BD7 = xcorr(zm6,zm7,'coeff');
BD7BD8 = xcorr(zm7,zm8,'coeff');
BD8BD9 = xcorr(zm8,zm9,'coeff');
BD9BD10 = xcorr(zm9,zm10,'coeff');
BD10BD11 = xcorr(zm10,zm11,'coeff');
BD11BD12 = xcorr(zm11,zm12,'coeff');

```

```

BD4BD5 = xcorr(zm4,zm5,'coeff');
BD3BD4 = xcorr(zm3,zm4,'coeff');
BD5BD6 = xcorr(zm5,zm6,'coeff');

```

```

BD8BD9 = xcorr(zm8,zm9,'coeff');
BD7BD8 = xcorr(zm7,zm8,'coeff');
BD9BD10 = xcorr(zm9,zm10,'coeff');

```

```

%-----
f =Fs/2*linspace(0,1,nfft/2)';
Bw=Fs/nfft;
%-----
% Plotting parameters
nfc=4000/Resolution;
hold on
% -----

```

```

figure(1);
% Time domain
subplot(1,1,1);
plot(k,BD1BD1,'-k',k,BD1BD2,'-r',k,BD1BD3,'-b',k,BD1BD4,'-
g',k,BD1BD5,'-c',k,BD1BD6,'-m',k,BD1BD7,'-y',k,BD1BD8,'--r',k,BD1BD9,'-
-k',k,BD1BD10,':k',k,BD1BD11,'--b',k,BD1BD12,'--m','Linewidth',4);
axis([3000,5000,-0.6,1.2]);
set(gca,'XTickLabel',{'-0.05','-
0.025','0','0.025','0.05'},'FontSize',24,'fontweight','bold')
hleg =
legend('\bf\fontsize{14}C(\tau)_1,_1','\bf\fontsize{14}C(\tau)_1,_
_2','\bf\fontsize{14}C(\tau)_1,_3','\bf\fontsize{14}C(\tau)_1,_4'
,'\bf\fontsize{14}C(\tau)_1,_5','\bf\fontsize{14}C(\tau)_1,_6','\
bf\fontsize{14}C(\tau)_1,_7','\bf\fontsize{14}C(\tau)_1,_8','\bf\
fontsize{14}C(\tau)_1,_9','\bf\fontsize{14}C(\tau)_1,_1_0','\bf\
onsize{14}C(\tau)_1,_1_1','\bf\fontsize{14}C(\tau)_1,_1_2');
% grid on
% -----
.
.
.
%-----
% Similar repeated command for figure 2 to 3.
%-----
.
.
.
% -----
figure(4);
% Time domain
subplot(1,1,1);
plot(k,BD4BD5,'-k',k,BD3BD4,'-r',k,BD5BD6,'-
b',k,BD8BD9,':k',k,BD7BD8,':r',k,BD9BD10,':b','Linewidth',4);
axis([3000,5000,-0.6,1.2]);
set(gca,'XTickLabel',{'-0.05','-
0.025','0','0.025','0.05'},'FontSize',24,'fontweight','bold')
hleg =
legend('\bf\fontsize{14}C(\tau)_4,_5','\bf\fontsize{14}C(\tau)_4,_
_3','\bf\fontsize{14}C(\tau)_5,_6','\bf\fontsize{14}C(\tau)_8,_9'
,'\bf\fontsize{14}C(\tau)_8,_7','\bf\fontsize{14}C(\tau)_9,_1_0')
;
% grid on
% end
% -----

```

A3. Matlab script for generating cross-correlation coefficient of flow parameters in frequency domain

```

clear;clc;
%-----
% Read the data

basefile = 'Directory of the data file';
for i = 1
%*** Complete File Name ***

```

```

%     expression = [basefile,'xcorr_ux_',num2str(i),'.OUT'];
%     expression = [basefile,'xcorr_Fx_',num2str(i),'.dat'];
expression = [basefile,'xcorr_Fy_',num2str(i),'.dat'];

%*** Load The Data ***
data = load(expression);
[m,n] = size(data);           %m is # rows %n is # cols
end
%-----
% Sampling rate
Ts=(data(2,1)-data(1,1));
Fs=1/Ts;
%-----
% Data cutting time
TStart=(data(1,1));
TEnd=(data(end,1));
TLength=TEnd-TStart;
NData=4000;
%-----
time=data(1:m,1); % (s)
Output10=data(1:m,2)'; % (full_bundle)
Output11=data(1:m,3)'; % (full_bundle)
Output12=data(1:m,4)'; % (full_bundle)
Output1=data(1:m,5)'; % (full_bundle)
Output2=data(1:m,6)'; % (full_bundle)
Output3=data(1:m,7)'; % (full_bundle)
Output4=data(1:m,8)'; % (full_bundle)
Output5=data(1:m,9)'; % (full_bundle)
Output6=data(1:m,10)'; % (full_bundle)
Output7=data(1:m,11)'; % (full_bundle)
Output8=data(1:m,12)'; % (full_bundle)
Output9=data(1:m,13)'; % (full_bundle)
%-----
nfft=NData;
Resolution=Fs/nfft; % freq. bandwidth (Hz)
%-----
% Deducing the mean to get the fluctuations
%-----
mean1=sum(Output1)/NData;
zm1=(Output1-mean1);
mean2=sum(Output2)/NData;
zm2=(Output2-mean2);
mean3=sum(Output3)/NData;
zm3=(Output3-mean3);
mean4=sum(Output4)/NData;
zm4=(Output4-mean4);
mean5=sum(Output5)/NData;
zm5=(Output5-mean5);
mean6=sum(Output6)/NData;
zm6=(Output6-mean6);
mean7=sum(Output7)/NData;
zm7=(Output7-mean7);
mean8=sum(Output8)/NData;
zm8=(Output8-mean8);
mean9=sum(Output9)/NData;
zm9=(Output9-mean9);
mean10=sum(Output10)/NData;

```

```

zm10=(Output10-mean10);
mean11=sum(Output11)/NData;
zm11=(Output11-mean11);
mean12=sum(Output12)/NData;
zm12=(Output12-mean12);
%-----
[C11,F]=mscohere(zm1,zm1,gausswin(1000),[],nfft,Fs);
[C12,F]=mscohere(zm1,zm2,gausswin(1000),[],nfft,Fs);
[C13,F]=mscohere(zm1,zm3,gausswin(1000),[],nfft,Fs);
[C14,F]=mscohere(zm1,zm4,gausswin(1000),[],nfft,Fs);
[C15,F]=mscohere(zm1,zm5,gausswin(1000),[],nfft,Fs);
[C16,F]=mscohere(zm1,zm6,gausswin(1000),[],nfft,Fs);
[C17,F]=mscohere(zm1,zm7,gausswin(1000),[],nfft,Fs);
[C18,F]=mscohere(zm1,zm8,gausswin(1000),[],nfft,Fs);
[C19,F]=mscohere(zm1,zm9,gausswin(1000),[],nfft,Fs);
[C110,F]=mscohere(zm1,zm10,gausswin(1000),[],nfft,Fs);
[C111,F]=mscohere(zm1,zm11,gausswin(1000),[],nfft,Fs);
[C112,F]=mscohere(zm1,zm12,gausswin(1000),[],nfft,Fs);

[C61,F]=mscohere(zm6,zm1,gausswin(1000),[],nfft,Fs);
[C62,F]=mscohere(zm6,zm2,gausswin(1000),[],nfft,Fs);
[C63,F]=mscohere(zm6,zm3,gausswin(1000),[],nfft,Fs);
[C64,F]=mscohere(zm6,zm4,gausswin(1000),[],nfft,Fs);
[C65,F]=mscohere(zm6,zm5,gausswin(1000),[],nfft,Fs);
[C66,F]=mscohere(zm6,zm6,gausswin(1000),[],nfft,Fs);
[C67,F]=mscohere(zm6,zm7,gausswin(1000),[],nfft,Fs);
[C68,F]=mscohere(zm6,zm8,gausswin(1000),[],nfft,Fs);
[C69,F]=mscohere(zm6,zm9,gausswin(1000),[],nfft,Fs);
[C610,F]=mscohere(zm6,zm10,gausswin(1000),[],nfft,Fs);
[C611,F]=mscohere(zm6,zm11,gausswin(1000),[],nfft,Fs);
[C612,F]=mscohere(zm6,zm12,gausswin(1000),[],nfft,Fs);

[C12,F]=mscohere(zm1,zm2,gausswin(1000),[],nfft,Fs);
[C23,F]=mscohere(zm2,zm3,gausswin(1000),[],nfft,Fs);
[C34,F]=mscohere(zm3,zm4,gausswin(1000),[],nfft,Fs);
[C45,F]=mscohere(zm4,zm5,gausswin(1000),[],nfft,Fs);
[C56,F]=mscohere(zm5,zm6,gausswin(1000),[],nfft,Fs);
[C67,F]=mscohere(zm6,zm7,gausswin(1000),[],nfft,Fs);
[C78,F]=mscohere(zm7,zm8,gausswin(1000),[],nfft,Fs);
[C89,F]=mscohere(zm8,zm9,gausswin(1000),[],nfft,Fs);
[C910,F]=mscohere(zm9,zm10,gausswin(1000),[],nfft,Fs);
[C1011,F]=mscohere(zm10,zm11,gausswin(1000),[],nfft,Fs);
[C1112,F]=mscohere(zm11,zm12,gausswin(1000),[],nfft,Fs);

[C45,F]=mscohere(zm4,zm5,gausswin(1000),[],nfft,Fs);
[C43,F]=mscohere(zm4,zm3,gausswin(1000),[],nfft,Fs);
[C56,F]=mscohere(zm5,zm6,gausswin(1000),[],nfft,Fs);

[C89,F]=mscohere(zm8,zm9,gausswin(1000),[],nfft,Fs);
[C87,F]=mscohere(zm8,zm7,gausswin(1000),[],nfft,Fs);
[C910,F]=mscohere(zm9,zm10,gausswin(1000),[],nfft,Fs);
%-----
f =Fs/2*linspace(0,1,nfft/2)';
Bw=Fs/nfft;

```

```

%-----
% Plotting parameters
nfc=4000/Resolution;
% hold on
% -----
figure(1);
% Time domain
subplot(1,1,1);
plot(F,C11, '-k',F,C12, '-r',F,C13, '-b',F,C14, '-g',F,C15, '-c',F,C16, '-
m',F,C17, '-y',F,C18, '--r',F,C19, '--k',F,C110, ':k',F,C111, '--
b',F,C112, '--m', 'Linewidth',4);
axis([0,500, 0, 1.2]);
set(gca, 'XTickLabel', {'0', '100', '200', '300', '400'}, 'FontSize',24, 'fontw
eight', 'bold')
hleg =
legend('\bf\fontsize{14}C({f})_1,_1', '\bf\fontsize{14}C({f})_1,_2', '\
bf\fontsize{14}C({f})_1,_3', '\bf\fontsize{14}C({f})_1,_4', '\bf\fontsi
ze{14}C({f})_1,_5', '\bf\fontsize{14}C({f})_1,_6', '\bf\fontsize{14}C({
f})_1,_7', '\bf\fontsize{14}C({f})_1,_8', '\bf\fontsize{14}C({f})_1,_9
', '\bf\fontsize{14}C({f})_1,_1_0', '\bf\fontsize{14}C({f})_1,_1_1', '\b
f\fontsize{14}C({f})_1,_1_2');
% grid on
% -----
.
.
.
%-----
% Similar repeated command for figure 2 to 3.
%-----
.
.
.

% grid on
% -----
figure(4);
% Time domain
subplot(1,1,1);
plot(F,C45, '-k',F,C43, '-r',F,C56, '-b',F,C89, '-g',F,C87, '-c',F,C910, '-
m', 'Linewidth',4);
axis([0,500, 0, 1.2]);
set(gca, 'XTickLabel', {'0', '100', '200', '300', '400'}, 'FontSize',24, 'fontw
eight', 'bold')
hleg =
legend('\bf\fontsize{14}C({f})_4,_5', '\bf\fontsize{14}C({f})_4,_3', '\
bf\fontsize{14}C({f})_5,_6', '\bf\fontsize{14}C({f})_8,_9', '\bf\fontsi
ze{14}C({f})_8,_7', '\bf\fontsize{14}C({f})_9,_1_0');
% grid on
% -----
% end

```

REFERENCE

Abbasian, F., Yu, S.D., Cao, J., 2009. Experimental and numerical investigations of three-dimensional turbulent flow of water surrounding a CANDU simulation fuel bundle structure inside a channel. *Nuclear Engineering and Design*. 239 (11), 2224-2235.

Abbasian, F., 2009. Numerical and Experimental investigation of turbulent flow of water surrounding a simulation CANDU fuel bundle in a tube. PhD Thesis, Ryerson University, Toronto, Canada.

Anselmet, F., Ternat, F., Amielh, M., Boiron, O., Boyer, P., Pietri, L., 2009. Axial development of the mean flow in the entrance region of turbulent pipe and duct flows. *Comptes rendus Mecanique*. 337 (8), 573-584.

Au-Yang, M.K., 2001, Flow-induced vibration of power and process plant components-A practical workbook, ASME Press, NY.

Baglietto, E., Ninokata, H., and Misawa, T., 2006. CFD and DNS methodologies development for fuel bundle simulations. *Nuclear Engineering and Design*. 236, 1503-1510.

Barsamina, H.R., Hassan, Y.A., 1997. Large eddy simulation of turbulent cross flow in tube bundles. *Nuclear Engineering and Design*. 172, 103-122.

Benhamadouche, S., and Laurence, D., 2003. LES, Coarse LES, and Transient RANS comparisons on the flow across a tube bundle. *International Journal of Heat and Fluid Flow*. 24, 470-479.

Bhattacharya, A., Yu, S.D., Kawall, G., 2011a, An experimental investigation of flow-induced vibration of a 43-element simulation CANDU fuel bundle under confined axial flow, Proceedings of the 23rd CANSIM, Vancouver, Canada, June 5-9.

Bhattacharya, A., Yu, S.D., Kawall, G., 2011b, Simulation of turbulent flow through inlet 37-element CANDU fuel bundles with angular misalignment, Proceedings of the SMiRT21, New Delhi, India, Nov. 6-11.

Bhattacharya, A., Yu, S.D., Kawall, G., 2012. Numerical simulation of turbulent flow through a 37-element CANDU fuel bundle, *Annals of Nuclear Energy*, 40, 87-105.

Bhattacharya, A., and Yu, S.D., 2012a. An experimental investigation of effects of angular misalignment on flow-induced vibration of simulated CANDU fuel bundles, *Nuclear Engineering and Design*, 250, 294-307.

Bhattacharya, A., and Yu, S.D., 2012b. Numerical simulation of flow through nuclear fuel bundles with angular misalignments, *ASME Journal of Fluids Engineering*, Vol. 134, 111101-1:15.

Bhattacharya, A., and Yu, S.D., 2013. Simulation of unsteady flow through a string of CANDU fuel bundles in pressure tube, *Nuclear Science and Engineering*, American Nuclear Society, In-Press.

Blevins, R.D., 1993. *Flow-Induced Vibration*, 2nd Edition. Krieger Publishing Company, F.L., U.S.

Chang, D., Tavoularis, S., 2007. Numerical simulation of turbulent flow in a 37-rod bundle. *Nuclear Engineering and Design*. 237, 575-590.

Chen, S.S., Wambsganss, M.W., 1972. Parallel-flow-induced vibration of fuel rods. *Nuclear Engineering and Design*, 18(2), 253-278.

Chen, S.S., 1975. Vibration of nuclear fuel bundles. *Nuclear Engineering and Design*, 35(3), 399-422.

Choi, H., Moin, P., 1994. Effects of the computational time step on numerical solutions of turbulent flow. *Journal of computational physics*. 113 (1), 1-4.

Curling, L.R., Paidoussis, M.P., 1992. Measurements and characterization of wallpressure fluctuations on cylinders in a bundle in turbulent axial flow: part 1 and 2. *Journal of Sound and Vibration*, 157(3): 405-449.

Chung, T., J., 2002. Computational Fluid Dynamics. 1st edition. Cambridge University Press, Cambridge, UK.

D'Arcy, D.F., Schenk, J. R., 1987, Axial velocity and turbulence measurements in adjacent subchannels of a 37-rod bundle, Proceedings of the 3rd International Symposium on Laser Anemometry, Boston, USA. 277-282

Germano, M., Piomelli, U., Moin, P., Cabot, W.H., 1991. A dynamic subgrid-scale eddy viscosity model. Physics of Fluids A. 3 (7), 1760-1765.

Gorman, D. J., 1971. An analytical and experimental investigation of the vibration of cylindrical reactor fuel elements in two phases flow. Nuclear Science and Engineering, 44, 277-390.

Hassan, Y.A., Barsamian, H.R., 1999. Turbulence simulation in tube bundle geometries using the dynamic subgrid-scale model. Nuclear Technology. 128, 58-74.

Judah, J., 1992. Overview of fuel inspections at the Darlington nuclear generating station. Proceedings of the annual conference - Canadian Nuclear Association. c1-c22.

Kim, H.M, No, H.C., 2004. Analysis of power spectrum density in the PWE fuel assembly using the 3-D LES turbulent model of Fluent 6. Proceedings of the 12th International Conference on Nuclear Engineering. April 25-29, Arlington, Virginia, USA. 295-303.

Lee, K.B., Jang, H.C., 1997. A numerical prediction on the turbulent flow in closely spaced bare rod arrays by a nonlinear k- ϵ model. Nuclear Engineering and Design. 172, 351-357.

Leonard. A., 1974. Energy Cascade in Large-Eddy Simulations of Turbulent Fluid Flows. Advances in Geophysics A. 18, 237-248.

Lilly, D.K., 1992. A Proposed Modification of the Germano Subgrid-Scale Closure Model. Physics of Fluids A. 4 (3), 633-635.

Merzari, E., Ninokata, H., 2009. Development of an LES methodology for complex geometries. Nuclear engineering and technology. 42 (7), 893-906.

Misra, A., Pauls, R.E., Vijay, D.K., Teper, W., Lin, T.C., Strzelczyk, A., Liu, J., Hemraj, R., 1994. Acoustic modelling in support of fuel failure investigation in a CANDU nuclear generating station. American Society of Mechanical Engineers, Pressure Vessels and Piping Division (Publication) PVP 279, 99-118.

Norsworthy, A.G., Field, G.J., Meysner, A., Dalton, K., and Crandell, A., 1994. Fuel Bundle to Pressure Tube Fretting in Bruce and Darlington Reactors. Canadian Nuclear Society, 15th Annual Conference Proceedings. 2, 2.

Norsworthy, A.G., Ditschun, A., 1995. Fuel bundle to pressure tube fretting in Bruce and Darlington. Proceedings-Annual Conference, Canadian Nuclear Association, (2), 16.

Paidoussis, M.P., 1966. Dynamics of flexible slender cylinders in axial flow. Part I and Part II. Journal of Fluid Mechanics, 26(4), 717-751.

Paidoussis, M.P., 1982. A Review of Flow-Induced Vibrations in Reactors and Reactor Components, Journal of Nuclear Engineering and Design, 7(1), 31-60.

Paidoussis, M.P., Curling, L.R., 1985. An analytical model for vibration of clusters of flexible cylinders in turbulent axial flow. Journal of Sound and Vibration, 98(4), 493-517.

Paidoussis, M.P., 2004. Fluid-structure interactions: slender structures and axial flow, Volume 1 and Volume 2. Elsevier Academic Press, San Diego, U.S.

Pettigrew, M.J., 1993. The vibration behavior of nuclear fuel under reactor conditions. Nuclear Science and Engineering, 114(3), 179-189.

Pope, S.B., 2000. Turbulent Flows, Cambridge University Press, New York, pp. 34 – 82.

Rollet-Miet, P., Laurence, D., and Ferziger, J., 1999. LES and RANS of Turbulent Flow in Tube Bundles. International Journal of Heat and Fluid Flow. 20, 241-254.

Sagaut, P., 2006. Large Eddy Simulation for Incompressible Flow. 3rd edition. Springer-Verlag, Berlin, Heidelberg.

REFERENCE

- Smagorinsky, J.S., 1963. General circulation experiments with the primitive equations, part I: The basic experiment. *Monthly Weather Review*. 91, 99-152.
- Smith, B.A.W., Derksen, D.D., 1998, Measurement of steady and unsteady hydrodynamic loads on a nuclear fuel bundle, *Journal of Fluids and Structures*, 12, 475–489.
- Stewart, W.B., 1992. Darlington NGS Unit 2 Fuel Damage Investigation. Proceedings of the 13th Annual CNS Conference, Saint John, June 7-10.
- Suh, Y.K., Lightstone, M.F., 2004. Numerical simulation of turbulent flow and mixing in a rod bundle geometry. *Nuclear Energy*. 43 (3), 153-163.
- Tennekes, H., Lumley, J.L., 1972. *A First Course in Turbulence*. The MIT Press. Massachusetts, U.S.
- Vijayan, P.K., Pilkhwal, D.S., Saha, D., Venkat Raj, V., 1999. Experimental studies on the pressure drop across the various components of a PHWR fuel channel, *Experimental Thermal and Fluid Science*. 20, 34-44.
- Welch, P.D., 1967. The Use of Fast Fourier Transform for the Estimation of Power Spectra: A Method Based on Time Averaging Over Short, Modified Periodograms. *IEEE Trans. Audio Electroacoust.* AU-15, 70-73.
- White, F.M., 2003. *Fluid Mechanics*, 5th edition. McGraw-Hill, New York.
- Yetisir, M., Fisher, N.J., 1997. Prediction of pressure tube fretting-wear damage due to fuel vibration. *Nuclear Engineering and Design*. 176, 261-271.
- Zhang, X., Yu, S.D., 2008. Experimental studies of a simulation CANDU fuel bundle structure in confined axial flow. Proceedings of FIV2008, Prague, Czech.
- Zhang, X., Yu, S.D., 2011, Large eddy simulation of turbulent flow surrounding two simulated CANDU fuel bundles, *Nuclear Engineering and Design*, 241(9), 3553-3572.